The Influence of Side Chain Modifications on Transport in Polymeric Mixed Ionic/Electronic Conductors

Jonathan W. Onorato

A dissertation
submitted in partial fulfillment of the
requirements for the degree of

Doctor of Philosophy

University of Washington
2020

Reading Committee:
Christine Luscombe, Chair
Eleftheria Roumeli
Guozhong Cao
Lilo Pozzo

Program Authorized to Offer Degree:
Materials Science and Engineering

University of Washington

Abstract

The Influence of Side Chain Modifications on Transport in Polymeric Mixed Ionic/Electronic Conductors

Jonathan W. Onorato

Chair of the Supervisory Committee:
Professor Christine K. Luscombe
Materials Science and Engineering

Mixed ionic/electronic conducting polymers (MIECs) are an important emerging class of materials, with rising interest due to the wide range of applications enabled by their unique properties. Recent research efforts have begun to focus on developing homopolymer-based MIECs by introducing ion-conducting side chains in place of alkyl chains that are more traditional for conjugated polymers. It has been widely shown that side chain variations in conjugated polymers have a significant effect on polymer electronic conduction; however, understanding of the influence of side chain variation for MIEC polymers on both the ionic and electronic conduction for MIECs remains limited, and optimization efforts have been largely Edisonian. This work seeks to expand on the field's understanding of these MIEC materials and the interplay between side chains and ionic conduction, focusing on enabling predictive understanding of their material properties. First, we explore, the influence of the connection for an oligoethylene glycol side chain, either with an oxygen atom directly attached to the polymer backbone, or with a methylene bridge, highlighting the importance of proximity of the oxygen atom to the polymer backbone on ionic conductivity. We follow this with an investigation into varying the concentration and position of oxygen atoms of an oligoethylene glycol side chain, highlighting the influence that subtle changes in oxygen atom placement have on the polymer morphology, and polymer interactions with lithium salts.

Acknowledgements

Science is so much more than an individual effort, and I know my PhD truly represents that. It's been probably my greatest joy during my PhD to have met so many amazing people who are all so smart, and so talented, and so caring. There are so many people I want to thank.

First and foremost, I want to thank Prof. Christine Luscombe. Without her guidance and inspiration, none of this work would have been possible. I also need to thank the Luscombe Group, past and present, for all their advice, thoughts, ideas, and support. Without them, I would still be just as lost today as I was in my first year of grad school. I also want to take a moment to thank all of the master's students, as well as undergraduates who have worked with me along the way. Thanks for helping me to be both a better mentor, and a better teacher, and thanks for your patience while I got there. Thanks also go to my committee members for agreeing to go on this long journey with me. Your inputs have been appreciated, and I've been grateful to get to share my research with such smart and caring people.

I also want to thank those who me find this path. Mr. Phil Sarver first encouraged me to explore chemistry and find joy in science. Prof. David Schiraldi showed me the magic that is polymer science. Prof. Stuart Rowan took me into his lab and mentored me. Without the support from both Prof. Schiraldi and Prof. Rowan, none of this would have been possible.

Thanks to all of my collaborators along the way, many of whom exposed me to topics I would have never gotten an opportunity to explore without them. Thank you all for being excited to share the work you've done, and for letting me be along for the ride. Huge thank you to my DMREF collaborators in particular, for being so open and so enthusiastic about the work we shared. You all always made me feel welcomed and supported. Thank you also to Dr. Micah Glaz, Dr. Liam Bradshaw, and the whole staff of the MAF for all your help.

Thanks also goes out to the Clean Energy Institute, including Suzanne Offen, Prof. Dan Schwartz, and Prof. Dave Beck, for supporting my research, and for supporting the efforts of GRID and DICE. You all made my PhD so much broader than I could have ever anticipated.

There are a few people who have gone above and beyond for me, and without whom my PhD would not have been so rich. Thank go to Dr. Lauren Kang, for constantly reminding me that life is more than your PhD, and for helping me figure out how to be healthy, happy and successful in the lab. Thank you to Dr. Sarah Holliday, for sharing your love of science, and more importantly, life, and for your answers to my endless questions about chemistry. And finally, thanks to (soon-to-be-Dr.) Wesley Tatum, for literally everything. He has been an essential friend and co-conspirator in everything I've done throughout my time at UW. We started this program together and have worked together every step of the way. It's only fitting that we should graduate at the same time. Congrats, and thank you Wes.

I also want to thank my family. You helped me to grow into the person who could be successful in a PhD. Thanks to all of my sisters for supporting me, even when they didn't know what I was working on. Thanks to my parents, Diane and Jeff, for your belief in my abilities and encouraging me to chase big things. I appreciate you all.

Finally, to my wife, Stephanie. You have been so patient through this long and difficult process. Without your love, encouragement, and support, none of this would be possible. Thank you for everything. You are amazing, and I am blessed to have you in my life.

Dedication:

I dedicate this thesis to my wife, my family, and my friends. Your love and support have made all the difference, and none of this would have been possible without you all.

Thank you.

Contents

List of Figures

List of Tables

List of Schemes

Ch. 1: Introduction to MIECs and Conjugated Polymers

Mixed ionic/electronic conductors (MIECs) are a class of materials with growing interest from the academic community due to their wide variety of potential uses. As MIECs are materials that can conduct both electrons and ions, they serve a unique functionality in electrochemical devices, enabling their use in sensors,[1,2] actuators,[3,4] batteries,[5,6] fuel cells,[7] and organic electrochemical transistors (OECTs).[8,9] MIECs can be fabricated from both ceramics and polymers; however, this work will be focused specifically on polymeric MIECs, and will use the term MIEC to refer only to polymeric MIECs.[10,11]

MIECs come in several distinct architectures. The most common type currently is a blended architecture, where a polymer that possesses electronic conduction is blended with a polymer that possesses ionic conduction.[5,12] Together, this blended material enables motion of both ions and electrons. The prototypical material for this, shown in Figure 1.1, is poly(ethylenedioxythiophene):poly(styrenesulfonate) [PEDOT:PSS], wherein the PEDOT component provides electronic conduction, and the PSS component provides ionic conduction.[13,14] Additional architectures include block copolymers,[15,16] and homopolymers.[17] Due to the highly complex phase-behavior of these materials, the links between morphology and MIEC performance are still poorly understood. This work uses chemical structure design to investigate the relationship between material performance and polymer architecture.

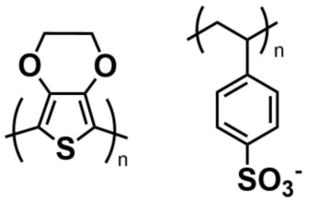

Figure 1.1: Structure of PEDOT:PSS, a commonly used MIEC polymer.

1.1 Crystallinity and the Effects of Morphology

Conjugated polymers have the ability to conduct charge because of the overlapping p-orbitals of adjacent, alternating, double and single bond sequences, as shown in Figure 1.2, top left.

These p-orbitals allow for the free motion of electrons between adjacent atoms, delocalizing charge across multiple atomic centers, and allowing charges to travel for as long as the conjugation extends. If multiple chains stack such that their π-orbitals overlap, charges can transfer between chains, as shown in Figure 1.2, bottom left, minimizing the amount of charge hopping, which is a slower process and results in reduced charge mobility. Polymeric materials are by nature semicrystalline, possessing domains of amorphous and crystalline regions. Due to the structure of the polymer backbone, no polymer can be completely crystalline, though it is possible for a polymer to be completely amorphous. The amorphous regimes are defined as regions of the bulk material that possess polymer chains with no long-range ordering, though short-range ordering and aggregation can occur. In the crystalline regions, polymer chains pack into ordered, repeating structures. This packing is partially driven by the π-π interactions between chains, causing these chains to interact and stack, as shown in Figure 1.2, bottom left. Due to the relatively weak interactions between chains, and the length of said chains, when polymers are in solution, they have a wide range of conformations that they can adopt. When ordering from solution into a solid-state structure, polymers are kinetically limited in their ability to diffuse and order, and there are often large potential energy barriers to reorganizing and ordering the polymer chain. As such, the polymer is not able to adopt a completely crystalline structure, instead forming crystalline and amorphous domains. Side chains, which are typically added for solubilizing the semiconducting polymer, play a significant role in this crystallization. For example, in poly(3-alkylthiophenes), when increasing chain length from poly(3-hexylthiophene) [P3HT] to poly(3-dodecylthiophene), the quality of the crystallite (as measured by ΔH_f^0) drops by half.[18] Even with seemingly small changes in chemistry of the side chains, significant changes in the morphology can be observed, which can have profound effects on the ability of the material to conduct electrons.

1.2 Conduction in Traditional Systems

1.2.1 Electronic Conduction in Conjugated Polymers

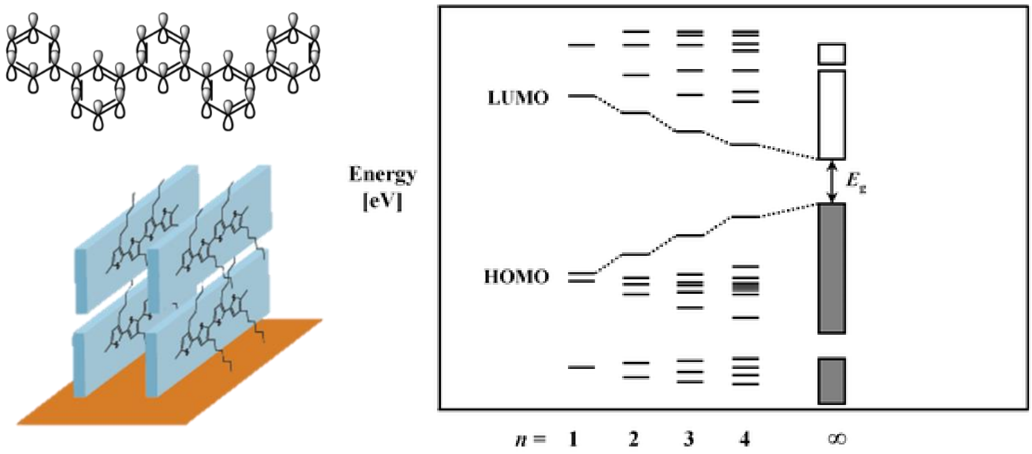

Figure 1.2: Top left, π-orbitals in a conjugated system. Bottom left, arrangement of P3HT in a crystalline stack. Right, generation of a band gap with increasing monomers incorporated into a conjugated polymer. Right figure reproduced from Ref. 19 with permission from the Royal Society of Chemistry.

Electronic conduction in polymeric materials occurs through the overlap of π-orbitals. In conjugated polymers, charge transport along the backbone is enabled through the overlap of these adjacent π-orbitals as shown in Figure 1.2. Charges are able to be delocalized over a range of monomers depending on their coplanarity; increasing the coplanarity of the conjugated backbone, the range over which atomic orbitals interact is extended. This range of interaction is called the conjugation length, and directly relates to the polymer's band gap. As the conjugation length increases, the band gap decreases, resulting in the formation of a band-like structure, as shown in Figure 1.2.[19] Planarity of a polymer backbone is highly important to charge conduction, as it extends the range over which a charge can be conducted before interchain transport becomes necessary. Interchain charge transfer is possible through π-stacking, allowing electrons to transport between the π-orbitals of adjacent polymer chains. This interchain charge transfer process is a relatively slow process as compared to along-backbone transport. Increasing the frequency of interchain transfer necessary results in a reduction in charge mobility.[20]

For charges to be transported at bulk, device-level scales, good charge transport must exist in two directions. This is because charges must have alternative pathways to travel when defects in the polymer chain or chain ends cause the along-backbone conduction pathway to end. This interchain transport is enabled and improved by the quality of the polymer's π-π stacking. Similar to transport along the backbone, planarizing groups are beneficial as they ease interactions between π-orbitals on adjacent chains. This stacking is the basis for crystallite formation in organic electronics, and typically the higher the percentage of crystallinity, the higher the mobility.[21] This is due in part to the lack of order in the amorphous regions, resulting in a high percentage of trap states and an increased likelihood of charge recombination, as shown in Figure 1.3c.[22,23] Tie-chains are single polymer chains that bridge multiple crystalline domains, providing along-backbone charge conduction between adjacent crystallites, as shown in Figure 1.3a,b. In order for charges to cross amorphous regions, tie-chains are critical, providing improvements in mobility from 10^{-5} to 10^{-2} cm^2/Vs for P3HT.[24]

The chemical structure of the polymer repeat unit has a significant impact on the charge mobility. By increasing the length of the solubilizing alkyl side chain from P3HT to P3OT, a reduction from 1.1×10^{-2} to 1.4×10^{-4} cm^2/Vs in charge mobility is observed.[25,26] A similar phenomenon is seen with branching chains; introducing an ethyl-branch into a hexyl side chain, poly(3-(2-ethylhexyl)thiophene), reduces the observed field effect mobility by an order of magnitude.[27] Increasing the rigidity of the backbone also increases the mobility, poly(2,5-bis(3-alkylthiophen-2-yl)thieno[3,2-*b*]thiophene) has a charge mobility approximately an order of magnitude higher than P3HT by substituting a two thiophene repeat units for a fused thienothiophene unit.[28] Other strategies for improving mobility include synthesizing donor/acceptor copolymers,[29–31] adjusting surface energy levels,[32,33] and increasing regioregularity.[34,35] These strategies revolve around rigidifying the polymer backbone and densifying the crystallites, both features which negatively contribute to ionic conduction. An interesting point is the recent discovery that high charge mobilities are possible even in highly amorphous material, if a polymer has a high molecular weight, and is sufficiently planar.[36] This is possible because of the connections between local aggregates by the tie chains formed from the long polymer chains. From this, it could be possible to develop a highly open, aggregate-based conjugated polymer that could co-optimize conduction of electrons and ions.

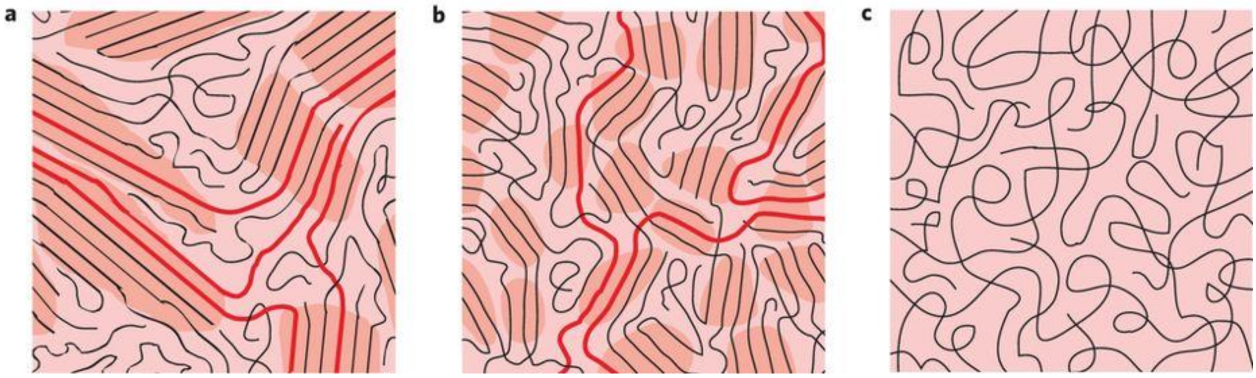

Figure 1.3: a. Semicrystalline polymer morphology with tie chains highlighted in red. b. Small, disordered aggregates with tie chains highlighted in red. c. Fully amorphous polymer. Figure reproduced with permission from Nature Publishing Group, reference 36.

1.2.2 Ionic Conduction in Non-conjugated Polymers

Ionic conduction in non-conjugated polymers is a well-studied phenomenon. Contrary to electronic conduction, ionic conduction requires less dense structures, an effect that is due to the relative size of ionic species. In a solid-state sample, ions move by random hopping between open adjacent positions in the structure. Due to the random nature, no net conduction of ions occurs. However, when a voltage is applied to the solid, the ions in the sample experience a diffusive driving force in response to the voltage, resulting in a biased-random walk, and a net conduction.

The nature of the ion to be conducted has an influence on the conduction; typically, for the same structure, the larger the ion being conducted, the slower the conduction. This is due to the increased lattice distortion that has to occur to allow such an ion to pass, presenting a larger activation barrier to hopping. That said, even ions as large as Cs^+ can be transported with the right material selection.[37] In addition to the size of the ion, the identity of the salt from which the ion is dissociated is highly important. If the ion pair does not dissociate, it will not respond to an applied voltage, and will not participate in conduction. As such, it is important to choose a counterion that is readily dissociated from the ion of choice. In lithium salts, bulky counterions such as TFSI, and PF_6 tend to find use, as they do not readily transport in PEO structures, simplifying conductivity. The extent of dissociation is also influenced by the dissolution media; incorporating polar, coordinating atoms into the polymer acts to increase the extent of dissociation by stabilizing the charge of the free ion. Typically, atoms like oxygen and nitrogen are used for this purpose, due to the difference in electronegativity between these atoms and carbon. The relatively small size is also advantageous, as it allows a greater coordinating density, resulting in highly general coordination for ions. The conductivity of the sample is dependent upon this dissociated ion concentration, N_{ion}, through Equation 1.1:

$$\sigma_{ion} = N_{ion} \times e \times \mu_{ion} \qquad \text{Equation 1.1}$$

Where μ_{ion} is ionic mobility, e is the charge of an electron, and σ_{ion} is ionic conductivity.

In addition to dissociating ions, the polymer structure plays an important role in the transport of the ionic species. The random hopping of these ionic species is assisted by the reptation, or polymer chain motion, of the coordinating polymer. The reptation of a polymer chain is increased with increasing temperature, so ionic conductivity tends to also increase. This reptation can induce both intrachain and interchain transport of ions. The mechanism for each is shown in Figure 1.4, left.[38]

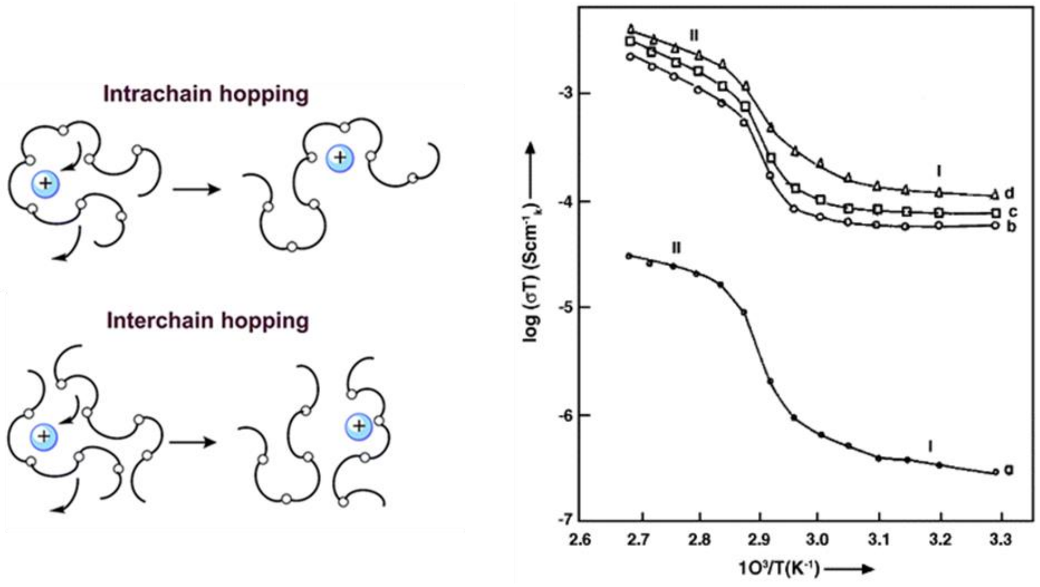

Figure 1.4: Left, Mechanisms of ionic conduction in solid polymer electrolytes. Figure reproduced from Ref. 38 with permission from the Royal Society of Chemistry. Right, Changing ionic conduction of a series of PEO electrolytes with increasing temperature. The strong rise at approximately 70 °C is due to a melting transition in the PEO, resulting in a significant increase in segmental mobility. Figure reproduced from Ref. 39 with permission from Elsevier.

The prototypical solid-state ionic conductor is poly(ethylene oxide) [PEO]. PEO is a particularly attractive ionic conductor, due to several properties arising from its chemical structure. The polymer has a T_g well below room temperature, allowing for ready motion of chains in the amorphous regions.[39] It also has high chain flexibility, allowing coordination of a variety of cations (*e.g.* Na^+, Li^+, Mg^{2+}, K^+, etc.), making it a highly general ion conductor.[40] Unfortunately, PEO also has a strong tendency to crystallize, resulting in poor intrinsic conduction below its melting temperature due to inhibited chain motion, as depicted in Figure 1.4, right.[41,42] To remedy this, several strategies, including introducing chain branching,[43,44] adding plasticizing agents,[45,46] and synthesizing brush polymers[47,48] have been used to suppress crystallization.

While there is evidence that ionic transport in crystalline PEO still occurs, it is unclear if such transport occurs in MIEC crystallites due to the π-π interactions, and thus limited space for ions to move.[49] Conjugated polymers are often doped with small molecules to increase conductivity; these small molecules either donate or remove an electron from the backbone, increasing the charge-carrier density. Recent work has provided some insight into the effects of this doping process, indicating that these dopant molecules do not enter into the crystallites, and instead reside in the amorphous regions of the polymer, due to the increased free volume available.[50,51] It thus remains unclear whether MIECs, due to the introduction of ion transporting groups, will demonstrate the same behavior, or will demonstrate crystal intercalation and transport in the crystalline regimes.

1.3 Mixed Ionic/Electronic Conductors

Systematic studies into the influence of morphology on ionic conductivity in MIECs are currently lacking.[52] Most studies have focused on the use of the MIEC, PEDOT:PSS, due in part to its high transconductance and wide commercial availability; however, these studies have primarily investigated changes in electrical conductivity.[52,53] PEDOT:PSS is supplied as a suspension in water, where the structure is composed of PSS polyanions surrounding PEDOT-rich domains.[54] After spin-coating, this complex morphology remains, resulting in a skin layer that is rich in highly-insulating PSS, reducing the bulk conductivity.[55] By removing that insulating layer, significant improvement in the electronic conductivity has been observed.[56] As such, there has been significant effort towards removing this skin layer, with the intent of increasing electronic conduction. A common method is the use of selective solvents, such as DMSO,[57] or diethylene glycol,[58,59] to induce stronger phase segregation and thin or remove the PSS^- layer. Generally, the argument for how this works is through solvent-screening of PSS^-, resulting in better phase-segregation.[60,61] While this has proven effective in significantly improving the electronic conduction (to extents of greater than three orders of magnitude), recent studies on the use of these secondary dopants or selective solvents in MIECs have determined that it comes at a cost of reduction in ionic conduction, likely due to the increase in crystallinity of the PSS layer.[52] Characterization of the effects of these treatments has proven difficult due to the complexity of the morphology, and the intrinsic disorder across multiple length scales.[62] Surface-sensitive techniques such as AFM have been able to distinguish that some solvent treatments result in a reduction in the surface concentration of PSS, and the appearance of continuous, relatively pure PEDOT pathways for charge conduction.[63,64] Techniques such as synchrotron X-ray scattering and small-angle neutron scattering have been partially successful, giving indications of how the solution structure of the blend influences the solid-state morphology.[54,65]

Some studies into the combined MIEC performance of PEDOT:PSS have been performed, studying the influence of morphology on the produced components. Hydration of PEDOT:PSS films appears to have a significant effect on ion uptake and mobility. When a film was swelled with water, ions moved into the film, and the experienced a significant increase in conductivity, reaching mobilties similar to those of the ion in water.[66] It was noted also that cross-linking, which acted to reduce the extent of swelling, also reduced the ionic conductivity.[66,67] By introducing increasing fractions of ethylene glycol as a co-solvent in a suspension of PEDOT:PSS, the extent of phase purity, and thus crystallinity, of the respective phases is increased. This results in a decrease in ionic conductivity due to an increase in the tortuosity of the ionic diffusion pathways, but a significant increase in the electronic mobility. The optimal transconductance is determined at a point when neither the electronic mobility or the ionic conductivity is maximized, as shown in Figure 1.5.[52] Similar enhancements could also be achieved by treating the cast PEDOT:PSS films with H_2SO_4, acting to increase the crystallinity and domain purity of each phase, and resulting in an edge-on orientation and a high transconductance of 19 mS, though the separated ionic conductivity was not reported.[68]

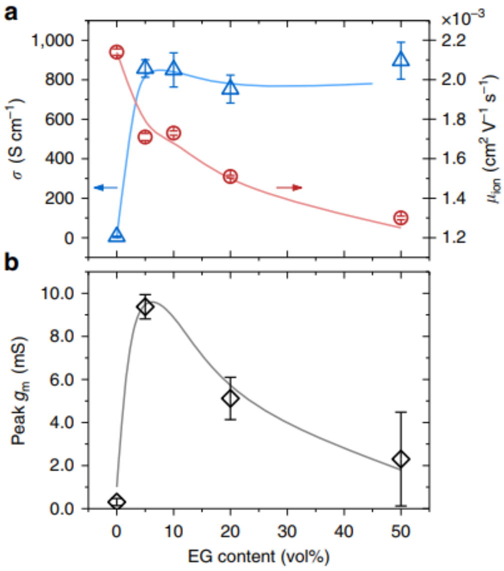

Figure 1.5: Evolution of ionic and electronic conduction in a single sample with increasing ethylene glycol content in the casting solvent for PEDOT:PSS. Figure reproduced with permission from Springer Nature from Reference 52.

Investigations into alternative MIECs to PEDOT:PSS have recently been appearing. Introduction of an oligoethylene glycol side chain to PBTTT enables ion conduction, allowing for bulk doping of an organic electrochemical transistor (OECT) film, whereas only introducing an alkoxy chain did not give similar performance.[69] Additionally, an n-type MIEC with varying degrees of oligoethylene glycol substitution was synthesized. By increasing the density of ethylene glycol side chains present along the polymer backbone, the extent of ion uptake into the polymer structure was increased, as was the transconductance. This effect was attributed to the increase in the pi-stacking distance, reducing the density of the structure.[70] While side chains can play a role in morphology and crystal structures of semiconducting polymers, which in turn effects the electronic properties, the side chains themselves do not participate in electron conduction. As such, modifying the side chains is a promising approach towards introducing ion-conducting functionality into conjugated polymers while minimizing disruptions to charge transport.

In the following chapter, we will explore the complex relationship between morphology and MIEC performance, highlighting the trends seen for a wide range of MIEC categories. We will explain the logic behind the development of different material categories, as well as their strengths and limitations. It is our hope that it will provide a baseline understanding, as well as common language to discuss the categories of MIECs and their performance.

Ch. 2: Structural Elements and Influences in MIECs

**This chapter is reproduced from previous work published in Materials Systems Design and Engineering with permission from the Royal Society of Chemistry.[71]

2.1 Polymer Blends

2.1.1 PEDOT:PSS

PEDOT:PSS-based MIECs have dominated research interests in MIECs thus far. PEDOT:PSS is a blended material of poly(ethylenedioxythiophene) and poly(styrene sulfonate), where the sulfonate group of the PSS provides ionic conduction, and the polythiophene backbone of the PEDOT provides electronic conduction.[72–74] PEDOT:PSS is available as a commercial suspension in water, and is also readily synthesized and derivatized.[75–77] Additionally, the sulfonate group acts to dope the PEDOT backbone, increasing electronic conductivity of the PEDOT backbone dramatically when compared to neat PEDOT.[78,79] These advantages, along with its excellent film-forming capacity, make PEDOT:PSS an attractive material for MIECs, but predictive relationships remain limited due to its complex morphology. The headway that has been made to understanding the structure-property relationships of PEDOT:PSS MIECs are described below.

PEDOT:PSS adopts a solid-state morphology with PEDOT rich domains separated by a PSS rich matrix; an example of this shown in Figure 2.1.[55,80] This morphology is generated from the solution state, where PSS anions encapsulate PEDOT-rich domains, solubilizing them in water.[54,59] This skin layer of PSS is maintained after spin-coating, and provides an electrically insulating layer around the PEDOT layer, reducing the overall electronic conduction.[52] In order to improve this conduction, several strategies have been employed, largely revolving around changing or controlling the morphology.

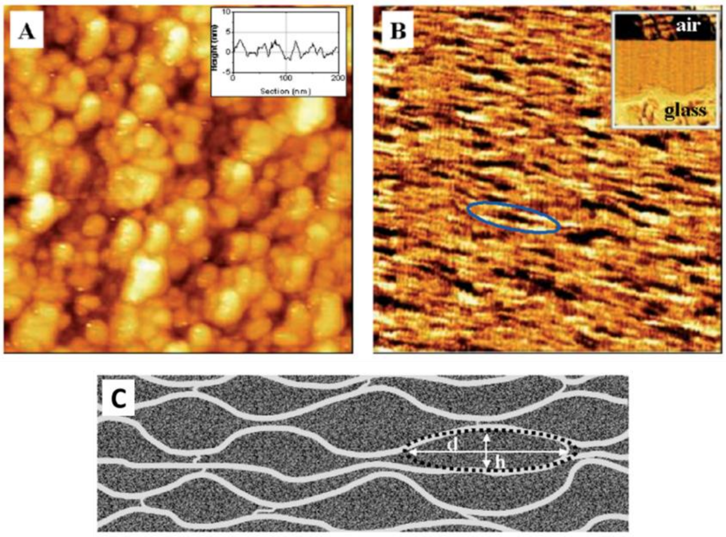

Figure 2.1: A: Top-down view of PEDOT:PSS spin cast on glass. B. A view of cleaved PEDOT:PSS on glass, with the inset showing the orientation of the sample. C: A schematic representation of the morphology seen, with d indicating the length of PEDOT domains, and h, the height. Figure adapted with permissions from Wiley Publishing Company from Reference 55.

One of the primary ways that researchers have worked to change this morphology is by co-processing with a solvent additive. The exact mechanism of enhancement is still unclear, but several theories for the observed electronic conductivity increases have been suggested.[81] One is that these solvents selectively solvate the polar PSS, resulting in a reduction of PSS content in the film.[59,60,81] This reduced PSS content also leads to an increase in the phase purity of the PEDOT domains. This results in a transition from a 1D electronic charge hopping method to a 3D interconnected network for charge transport, resulting in a significant increase in conductivity by as much as three orders of magnitude.[55,82] Another proposed theory is that the introduction of these solvents acts to screen excess PSS from PEDOT, allowing reorienting and better phase-segregation between PEDOT particles.[83] This also results in greater interconnectedness between adjacent PEDOT particles, increasing the electronic conductivity.[83] Processing with a co-solvent can also change the structure of the polymer backbone. For example, with a highly polar co-solvent, the PEDOT chains change from a coil-like structure to an extended coil or even a linear structure.[84,85] This structural change results in better π-stacking interactions between PEDOT chains, enhancing charge transport.[86]

Unfortunately, this solvent processing seems to result in a concomitant reduction in ionic conduction, and co-optimization has proven to be difficult. In the case of the ethylene glycol cosolvent treatment, it was observed that with increasing ethylene glycol content, though the electronic conductivity increased, the ionic conductivity decreased. This resulted in an initial increase in transconductance, but then a decrease, as shown in Figure 2.2.[52]

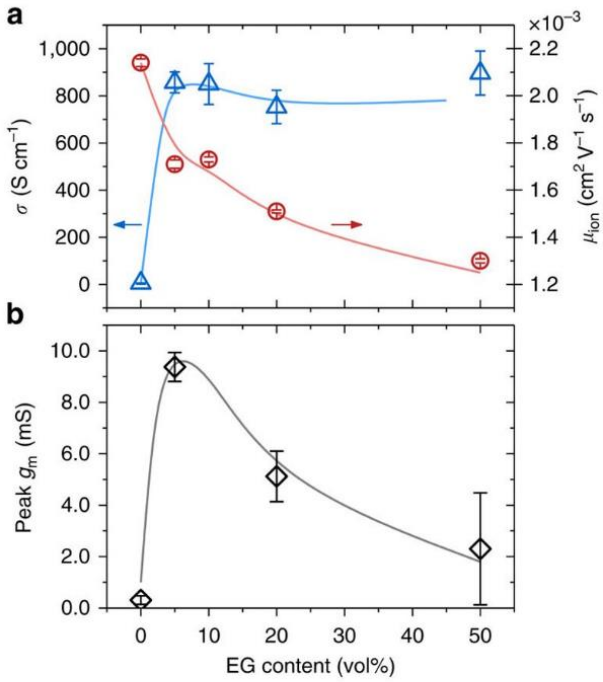

Figure 2.2: a) The evolution of electronic conductivity and ionic mobility and, b) demonstration of the evolution of transconductance with increasing ethylene glycol content, and thus crystallinity. Figure reproduced with permission from Springer Nature from Reference 52.

Post-processing treatment of films with strong acids, such as concentrated sulfuric acid, has also resulted in an exceptionally high electronic conductivity of 4,380 S/cm. This was done through the formation of nanofibrils of PEDOT:PSS, and also through the removal of excess PSS.[87] However, to achieve this extremely high conductivity, more than 70% of the PSS content was removed, likely resulting in extremely poor ionic conduction.[53] Similar experiments using several other acids showed similar, albeit lesser increases in conductivity, but did not show the formation of nanofibrils.[88,89] Instead, similar to changes observed from co-solvent processing, the increases were attributed to a conformational change and a reduction of PSS content.[90,91] While not explicitly measured, it would be reasonable to assume that similar to the co-solvent treatment effects, acid treatment would reduce ionic conduction.

In addition to solvent-based processing, researchers have investigated the effects of introducing cross-linking agents to PEDOT:PSS. In conjugated polymers, introduction of cross-linking agents results in an increase in the density of the structure, and a reduction in the ability of the structure to move.[92] The predominant cross-linking agent for PEDOT:PSS is (3-glycidyloxypropyl)trimethoxysilane (GOPS), which reacts primarily with the sulfonate group of the PSS, as well as with residual hydroxyl groups on substrate surfaces, as shown in Figure 2.3.[93–95]

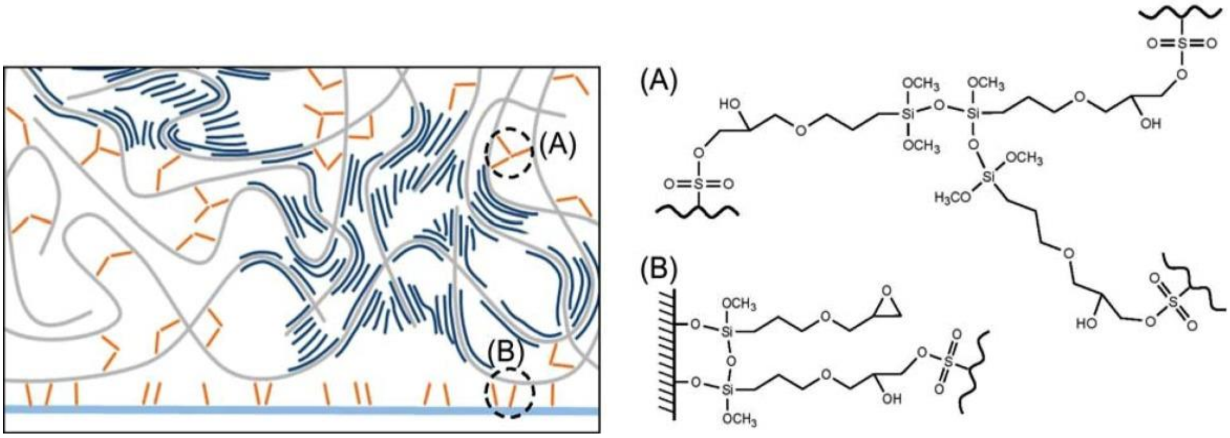

Figure 2.3: Schematic representation of the morphology and mode of interaction from GOPS treated PEDOT:PSS. Shown at the right are GOPS interactions with A, PSS in the polymer film and B, the substrate. Figure reproduced with permission from Wiley Publishing Group, Reference 67.

While GOPS increases the aqueous stability of PEDOT:PSS based devices, it also reduces both the electronic and ionic conductivity of the sample.[66,96,97] Since GOPS only reacts with the excess PSS, and does not cause a change in the extent of oxidation of the PEDOT, this implies that the reduction in electrical conductivity is only due to a morphological change.[67] The decrease in ionic conductivity was argued to be due to the reduction in swelling of the polymer with water, resulting in a denser polymer structure and reduced space for the ion to be transported through.[66,68,98] The electronic conductivity decrease was proposed to be due to an increase in the degree of separation between conducting PEDOT domains.[67,98] Further work has shown that the degradation of electronic conductivity is proportional to the loading of GOPS, and by tailoring the concentration of GOPS, specific and controllable electronic conduction, as well as aqueous stability, can be obtained.[98] A newer cross-linking agent, divinyl sulfone, demonstrates less of an impact on the electronic conduction, likely due to the difference in cross-linking mechanism, which occurs with residual nucleophiles in the PEDOT:PSS suspension rather than with the PSS.[99] This formulation also presents the interesting advantage of being capable of forming free-standing films with reasonably high stretchability (15% maximum elongation), potentially enabling use as a stretchable, biointerfacing device.[100] Though no morphological studies have been performed, crosslinking with the divalent cation Mg^{2+} through PSS anions results in only a 20% decrease in conductivity as compared to neat PEDOT:PSS, and could present an interesting mode of crosslinking for further study.[101]

In summary, PEDOT:PSS provides a complex morphology that often complicates analysis of the connection between said morphology and its performance. However, it has been shown that treating PEDOT:PSS with solvents results in a significant increase in electronic mobility, but also a significant decrease in ionic conduction due to the increase in phase-segregation and a reduction in overall PSS content. Further, treatment with acid shows the same results, by increasing the degree of order of the PEDOT domains, and by reducing the overall PSS content. Crosslinking presents an interesting way of addressing the lack of stability of PEDOT:PSS in water. By crosslinking, the electronic mobility decreases slightly due to increasing separation between adjacent conducting PEDOT-rich domains. Ionic conduction decreases due to a decrease in the available free PSS, and a reduction in swelling.

2.1.2 Alternative Polymer Blends

While PEDOT:PSS represents an important MIEC blend, several other blended polymers have been investigated to address some of its drawbacks, such as cell toxicity and its high acidity.[102,103] There is not as extensive of literature on other blended polymers; however, efforts, especially into quantifying electronic conductivity, have started appearing. A study into the effects of adjusting the polyelectrolyte in PEDOT:PSS determined several interesting effects. Similarly to PEDOT:PSS, in PEDOT:poly[4-styrenesulfonyl (trifluoromethyl sulfonyl) imide potassium salt] (PSTFSIK) it was observed that there is a relationship between the extent of swelling and the ion conduction of a sample. The greater the extent of swelling, the higher the ionic conduction observed.[104] Unlike PEDOT:PSS, PEDOT:PSTFSIK forms highly interconnected agglomerates upon dispersion from water, which could account for the high electronic conductivity without the need for solvent treatments. PEDOT:PSTFSIK also showed electronic performance enhancement and increased phase purity upon DMSO solvent treatment.[105] Interestingly, increasing the molecular weight of the ionically conducting polymer had a small, negative effect on the overall ionic conductivity, though it also resulted in a small increase in the electronic conductivity.[104] It was noted that counterions for the PEDOT synthesis (K^+ vs. Li^+) have minimal impact on the overall performance of the produced polymer.[104,105] In PEO blends with PEDOT:PSS, with additional PEO content, higher electronic conductivity is seen in the PEDOT phase.[106,107] This was observed to occur through the increased interaction of

PSS with PEO, resulting in PEDOT which was better interconnected and more phase pure.[106,108] Encouragingly, this also results in an increase in ionic conductivity.[106,107] Additionally, these materials demonstrate a high ionic conduction in non-aqueous (acetonitrile) electrolytes, whereas samples with only PEDOT:PSS shows poor ionic conduction, a result likely due to both the partial solubility of PEO in acetonitrile (enabling swelling), and due to the intrinsic conductivity of PEO.[107] This result implies the generality of solvent swelling on ionic conduction, even with intrinsically ionically conducting polymers. An unexpected benefit of blending PEO with PEDOT:PSS is that the material becomes stretchable, able to reach elongations of approximately 35%.[108] In another study, poly[2-methoxy-5-(2-ethylhexyloxy)-1,4-phenylenevinylene] (MEH-PPV) was blended with PEO, and the effects of variations in solvent additives during processing were investigated. The solvent additives were chosen to behave as surfactants, with polar and nonpolar ends, increasing the degree of interaction of the ionic and electronic conductors and resulting in an interpenetrating network of MEH-PPV with PEO, as shown in Figure 2.4.[109] Similar networks are observed with the blending of MEH-PPV and PEO without surfactants, though the extent of phase-segregation appears to be less.[110] This highly interconnected network is ideal for some MIEC devices, as it allows high mobility of ions and electrons, and ready doping of the conjugated backbone, leading to a strong and quick response to an electrochemical signal.[109,110] It is interesting to note that the introduction of a bifunctional additive appears to significantly improve the lifetime of polymer light-emitting electrochemical cells, likely by stabilizing the interpenetrating network morphology and preventing aggregation.[109] This reduction in degree of phase-separation can also be induced by introducing functionalities into the polymer backbones that improve the compatibility of the ionic and electronic conducting polymers, the domain sizes can be decreased, and the degree of intermixing of the two components improved.[109,111,112]

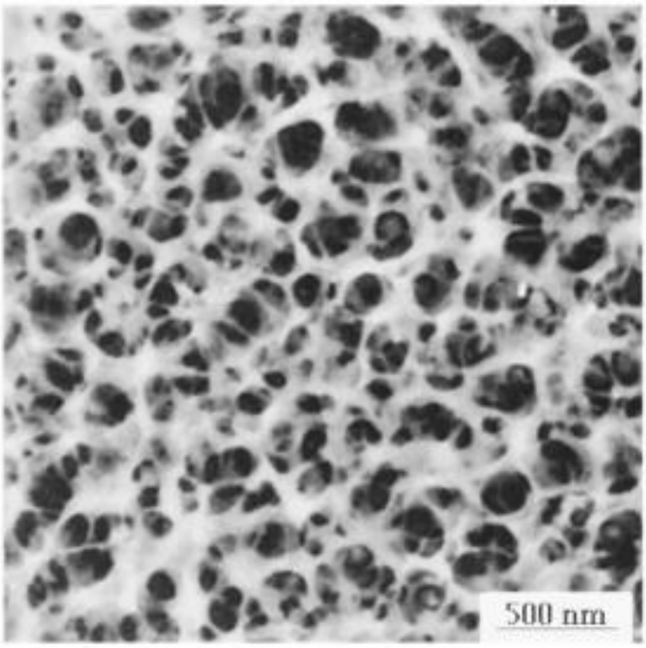

Figure 2.4: SEM image of an MEH-PPV-b-PEO film cast from a blend containing a surfactant. For this image, the PEO was dissolved out of the material to emphasize the interconnected morphology. Figure reproduced with permission from American Institute of Physics, Reference 112.

There are still many unanswered questions about the relation between morphology and MIEC performance in blended polymer MIECs. However, some initial trends have become clear. It is critical to balance the loading and final quantities of the ionic and electronic conducting components, to ensure that both conduction pathways will be viable. Ionic conduction requires disorder and amorphous structures, whereas electronic requires compact and crystalline.[113] Changing the polyanion for PEDOT synthesis to PSTFSIK results in a morphology with highly interconnected PEDOT domains, which results in a significant increase in conductivity compared to PSS. In polymer blends containing PEO, reducing the size of the domains for each polymer results in better performance of the MIEC by increasing transconductance. Specifically, in blends of PEDOT:PSS with PEO, the PEO acted to increase the purity and ordering of the PEDOT domains, increasing both ionic and electronic conductivity.[106,107] Also, treatment of blends with surfactants could result in a reduction of size scale of phase-segregation, and result in the formation co-continuous interpenetrating networks of ionic and electronic conduction.

2.2 Block Copolymers

Block copolymers (BCPs) can demonstrate phase-segregation between the block phases, a phenomenon which can drive interesting morphological features. This segregation is often generated through hydrophobic/hydrophilic interactions, which is also the case in common block copolymer MIECs; the ion-conducting component is hydrophilic to facilitate interactions with ions, whereas the electron-conducting component is typically hydrophobic. These types of interactions often lead to increased ordering of the respective phases, and, due to the nanoscale length of segregation, results in highly intermixed phases.[114,115] This highly ordered and intermixed morphology seems promising for MIEC performance.

Early work in block copolymers showed that when combined with an insulating block such as polystyrene, P3HT showed self-assembly into nanofibrillar P3HT structures, resulting in an increase in the neat electronic conductivity due to improved ordering of the polymer backbone.[116] The introduction of ionic salts into block copolymers acts to stabilize the phase-separation, increasing the temperature over which BCPs maintain a phase-segregated morphology.[117,118] By replacing the insulating blocks with ionically conducting blocks, additional functionality can be introduced; one such example of this mixed functionality was shown with P3HT-*b*-PEO. The phase-segregation present in this sample, as shown in Figure 2.5, resulted in an increase in the electronic conductivity in spite of the reduction in P3HT volume fraction, due to the increase in ordering.[15,16]

The lamellar morphology also resulted in bicontinuous pathways for both ionic and electronic conduction, allowing for ionic conductivities of approximately 0.1 mS/cm.[16] By heavily doping the P3HT phase, significant electronic conductivity increases are seen.[119] This result has the added advantage of preventing over-discharging in battery electrodes, as the resistance increases significantly with increasing state of discharge due to the reduction in oxidation state. The relative molecular weights of the two blocks also play a significant role. By varying the molecular weight of the components of the block copolymer between 9 kg/mol-2 kg/mol and 5 kg/mol-4 kg/mol P3HT-PEO, the morphology switches from a nanofibrillar to a lamellar phase. This morphological change seems to improve the ionic conduction, though that result could also be due to the increase in PEO weight fraction.[15] It appears that this transition results in a nearly complete exclusion of lithium from the P3HT phase.[15] A reduction of the enhancement of electronic conduction from the addition of PEO is also seen with transition from nanofibrillar to lamellar, though this change could also be due to a reduction in the P3HT content, which has been shown to limit electronic conduction enhancements from phase segregation.[15,16,120]

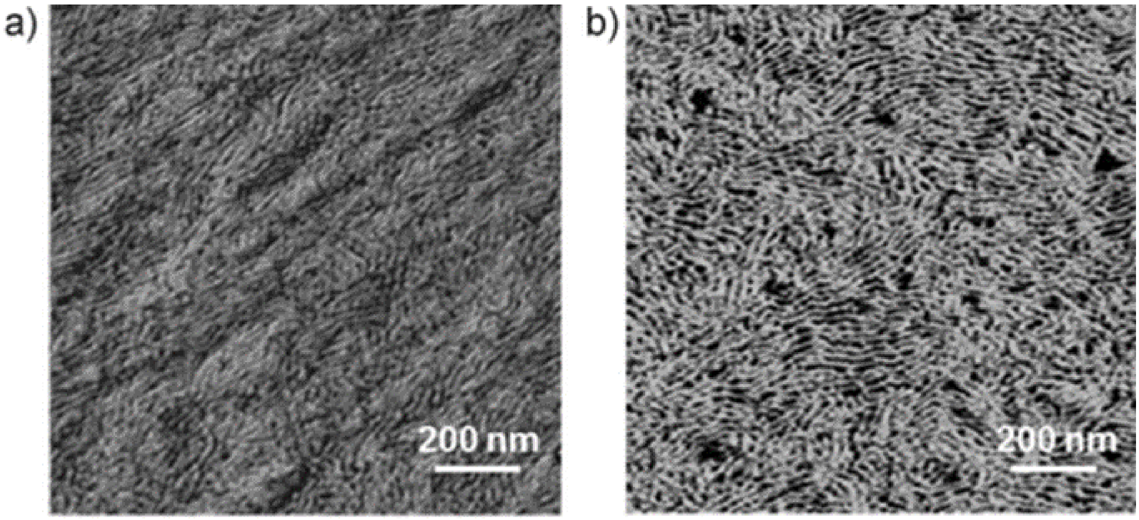

Figure 2.5: Tapping-mode AFM phase image of a) P3HT homopolymer and b) P3HT-PEO. Figure reproduced with permission from John Wiley and Sons, Reference 16.

P3HT-PEO block copolymers present several interesting morphological features that have notable influences on the MIEC performance. Phase-segregation in these materials drives the formation of P3HT nanofibrils in a matrix of PEO, which results in an increased electronic mobility by comparison to neat P3HT. This phase-segregation results in a bi-continuous network of ionically conducting PEO and electronically conducting P3HT with a relatively small degree of separation between the phases due to the chemical bonds between the P3HT and PEO units of the block copolymer. By changing the relative lengths of the P3HT and PEO units, the nanofibrillar morphology can be changed to a lamellar one, a transition which results in an increase in the ionic conductivity. Research into block copolymer MIECs beyond P3HT-*b*-PEO are still quite limited, and currently focus exclusively on morphological characterization, rather than electronic or ionic conduction.[121–123] As such, discussion of these materials has been excluded from this work, though they represent promising potential chemistries, and should be the subject of future research work for MIECs.

2.3 Homopolymers

Some of the earliest work with MIECs involved the investigation of homopolymers such as poly(3-methylthiophene), polycarbazole, and polyacetylene.[124–127] They were poor conductors of ions however, due to the significant hydrophobicity of these polymers.[9] Hydrophobicity results in strong phase-segregation of the ions out of the MIEC matrix and a reduction in the dissociation of the ionic salt, thus reducing both the concentration of ions and the ionic conductivity. Polymers such as polyaniline and polypyrrole saw greater success, due to the increased hydrophilicity of their backbones.[5,128,129] Early work with polyaniline saw difficulties in maintaining consistent morphologies from electrochemical polymerizations, and also incomplete ion-migration into the bulk of the film.[128] Polyaniline and polypyrrole saw significant use as pH sensors, demonstrating marked changes in conductivity.[128,130] An interesting method that resulted in significant increases in electronic conductivity of polyaniline was to gate the material using sulfuric acid, resulting in conductivities as high as 1,000 S/cm. The origination of such a strong increase was proposed to be due to the ability of the weakly bound protons to diffuse through the amorphous regions between highly crystalline islands, effectively mitigating the low conductivity amorphous regions and improving crystalline domain connectivity.[131] In an attempt to mitigate the low ionic conductivity of polypyrrole, a PEO-modified polypyrrole was synthesized, which enabled improved injection of ions into the polypyrrole material, though no discussion as to the morphological basis for this improvement was provided.[132] Recent work using a polymer acid (poly(2-acryl-amido-2-methyl-1-propanesulfonic acid)) as a template has resulted in increased stability, and improved water dispersibility of polypyrrole, which has led to its use in fuel cells and in battery electrodes.[5,7,133]

Polyaniline and polypyrrole both possess significant drawbacks that have limited the scope of their usage. Polypyrrole has an irreversible loss of conduction upon H_2O_2 exposure, and polyaniline loses its conductivity in environments with $pH > 5$. From these significant drawbacks, and the difficulty of processing polypyrrole and polyaniline, recent research has begun to investigate alternative conjugated backbone chemistries, specifically those conjugated polymers containing hydrophilic moieties to enable improved ionic conduction. A method for introducing hydrophilic groups is exchanging the typical alkyl side chains of conjugated polymers for oligoethylene glycol chains. As the side chains do not participate in electronic conduction, they can be exchanged without significantly altering the band-gap of the polymer, though they can have a significant influence on the aggregation and crystallization behavior.[27,134,135] Early studies of oligoethylene glycol-modified polythiophene showed that it demonstrated excellent doping stability, an effect attributed to the increased interactions between the hydrophilic side chains and the small-molecule dopants.[136] A study into the effect of either an alkoxy or oligoethylene glycol side chain for a PBTTT backbone showed that, though the morphology of the two was similar, the oligoethylene glycol allowed for bulk ionic transport (which was unfortunately not quantified), whereas the alkoxy did not show any. This could be a result of the intrinsic conductivity of the oligoethylene glycol chains, or it could be a product of swelling. Given results from PEDOT:PSS systems, it seems likely that swelling is a significant component.[66] However, an interesting point was that the volumetric capacitance of the sample was approximately six times larger for this polymer than for PEDOT:PSS. This implies that though ionic conductivity was lower (10% swelling as compared to 155% in PEDOT:PSS), there was a greater availability of electronic doping sites, likely due to the close proximity of ion conducting and electron conducting moieties.[69] If this result proves to be general, it would be a significant advantage for homopolymer MIECs. While an edge-on texture does appear to result in an increase in electronic mobility, it appears to have minimal influence over the ionic conductivity.[137] A more significant influence appears to come from the oligoethylene side chain density. Too high of a density of oligoethylene glycol side chains leads to a reduction in performance, as it is too detrimental to ordering and packing of the π-stack, whereas too low a density results in too dense packing, placing too strong a restriction on ionic transport.[70,137] This modification of conjugated polymers with oligoethylene glycol side chains has also been extended to n-type semiconductors, with a recent paper investigating MIEC performance of an naphthalenediimide (NDI)-based MIEC.[70] The introduction of oligoethylene glycol side chains resulted in a reduction of electronic mobility, a result due to an increase in paracrystalline disorder and a crystalline form transition from 60% Form I and 40% Form II to 90% Form I, reducing π-overlap. Though the comparison is made with different conjugated backbones, increasing the length of the oligoethylene glycol side chains appears to increase the extent of swelling (10% in the PBTTT as compared to 100% in NDI).

In addition to oligoethylene glycol-substituted conjugated polymers, ionic conductivity can be introduced into conjugated polymers by synthesizing a conjugated polyelectrolyte.[138,139] In one such polymer, poly(3-carboxypentylthiophene), it was shown that the introduction of a polar group, a carboxylic acid, on the terminus of an alkyl side chain was sufficient to enable ionic transport.[140] The effects of solvent treatment with ethylene glycol on another conjugated polyelectrolyte, poly(6-(thiophene-3-yl)hexane-1-sulfonate) tetrabutylammonium [PTHS], were studied. Similarly to PEDOT:PSS, this treatment resulted in increased ordering of the conjugated backbone, resulting in the formation of a fibrillar morphology.[9,83] This results in an increase in electronic conduction, as measured by an approximately sevenfold increase in drain current as compared to pristine PTHS.[9] Contrary to the results in PEDOT:PSS, this treatment actually also increases the swelling of the sample by 20% over the untreated sample and an increase in the ionic conduction, an effect which was attributed to the formation of the fibrillar morphology, as shown in Figure 2.6.[9,52]

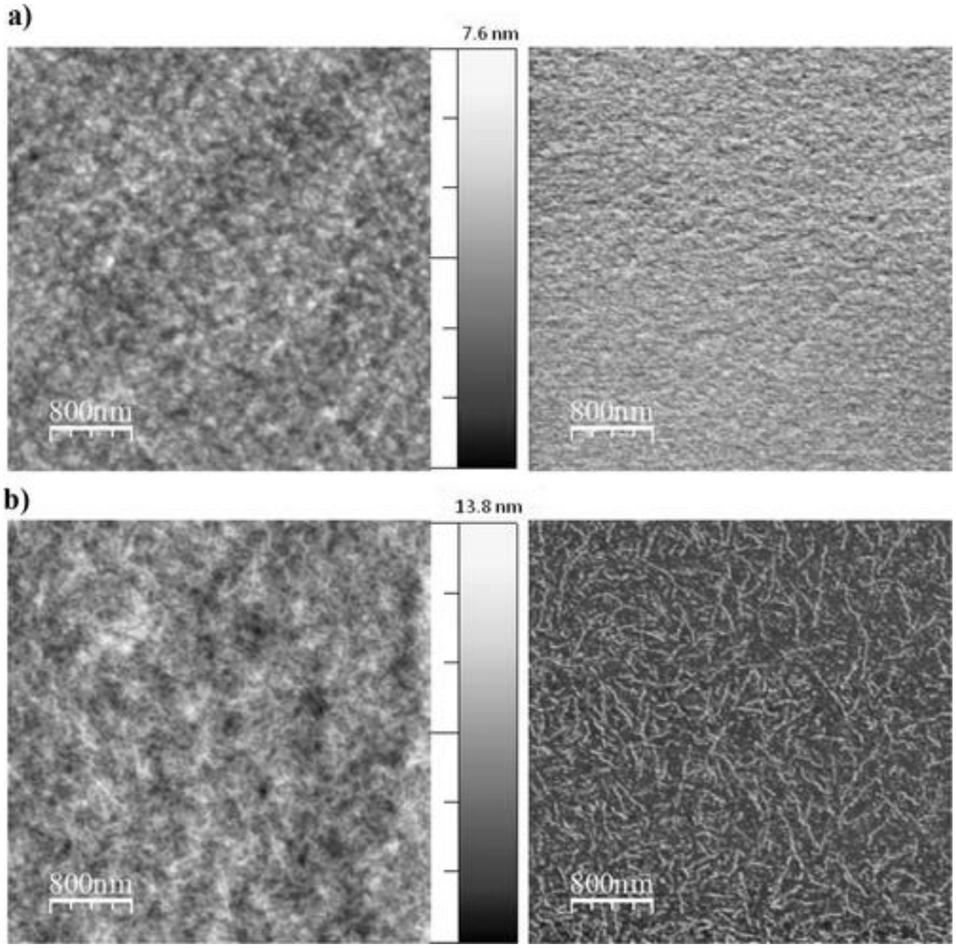

Figure 2.6: The formation of a nanofibrillar morphology of PTHS upon treatment of the polymer with ethylene glycol. A is the untreated morphology, and B is the treated. Shown to the left is the height, and the right is the phase image for each sample. Figure reproduced with permission from John Wiley and Sons, from Reference 9.

There remains significant room for improvement in understanding the connection between morphology and MIEC performance in these homopolymer materials, particularly in understanding the effects of side chain architectures on ionic conduction; however, recent progress has been highly encouraging. Hydrophilicity of at least a component of the system is critical to increasing ion uptake and ionic conductivity. Increasing the availability of electronic sites for doping interactions leads to an increase in volumetric capacitance, an effect which occurs by reducing the distance over which the electronically conducting and ionically conducting segments are separated. The spacing of oligoethylene glycol side chains is critical. At too dense a spacing, the disruptions to the π-stacking ability results in a significant decrease in electronic conductivity, and at too high of a spacing, the crystallite packing becomes too dense, and there is a reduction in the swelling of the polymer, reducing ionic conductivity. In PTHS, the formation of nanofibrillar structures through ethylene glycol treatment resulted in both an increase in ionic and electronic conductivity, in marked contrast to the results seen in PEDOT:PSS, and an encouraging result, pointing to the possibility that co-optimizing ionic and electronic conductivity is possible.

2.4 Conclusions and Future Outlook

Herein, the morphological considerations for MIEC performance were discussed for three types of MIEC materials, blended polymers, block copolymers, and homopolymers. Each architecture used for producing MIECs offers its own unique advantages and presents its own challenges. The trends observed for each material class do not necessarily follow between architectures, however, the information gained regarding one system can provide insights into effective methods for other architectures. For example, the treatment of PTHS with ethylene glycol was inspired by the treatment of PEDOT:PSS with ethylene glycol, but the results were not the same for both materials. More work is needed to understand and connect what morphological properties are advantageous for ionic and electronic conduction enhancement, with the ultimate goal to be to develop structure/property relations for each of these architectures of materials.

By summarizing the work that has been done to connect the morphologies generated for each of these architectures to the resultant properties, it is hoped that an expanded appreciation of the importance of this understanding is gained. The consideration of morphology and its influence on MIEC performance is still relatively new, but it presents an opportunity for significant advancement of MIECs and their use in a number of applications. Unexpected results, such as the increasing ionic conductivity with increasing crystallinity in PTHS, should be investigated deeply, then investigated in other polymer systems, for pushing the bounds of our current knowledge. Further investigation into modifying both the length and the polarity of the ion-conducting side chains could prove advantageous. It is currently unclear to what extent changing the length of these chains will modify the ionic and electronic conduction and what effect it will have on the polymer morphology. An additional important consideration is migrating from aqueous electrolytes to organic electrolytes. In particular, it will be interesting to see if the same performance trends observed with aqueous electrolytes are maintained for organic electrolytes, due to the differences in swelling that would be expected for a more non-polar electrolyte. Finally, ionic liquids have proven to be quite powerful in improving the ionic conduction in electrolytes, and incorporation of such moieties into a polymer backbone could result in significant improvements in ionic conductivity, especially when coupled with an ionic liquid as a gating electrolyte. The potential for improvements possible through improved morphological understanding is encouraging and could potentially allow the application of this technology in a host of devices, including such devices as body-integrated sensors and in electrochemical devices such as batteries.

Ch. 3: Influence of side-chain chemistry on structure and ionic conduction characteristics of polythiophene derivatives: a computational and experimental study

**This chapter is reproduced from previous work published in Chemistry of Materials with permission from the American Chemical Society.[141]

Statement on Distribution of Work: The work done herein was a combination of efforts by Dr. Ban Dong, Dr. Christian Nowak, and I. Specifically, I was responsible for all synthetic components of this work, as well as SEC and DSC analysis, and contributed writings associated with those tests. We also discussed ideas and conclusions from the data collaboratively prior to the writing of this paper.

Abstract:

Although extensive efforts have been devoted to understanding electronic transport in conjugated polymers, little is known about their ionic conduction characteristics in relation to polymer chemistry, processing, and morphology. This work presents a combined computational and experimental study on morphology and ion transport in thin-film blends of polythiophene derivatives bearing oligoethylene glycol side chains and lithium bis(trifluoromethanesulfonyl)imide (LiTFSI). Using molecular dynamics (MD) simulations, we show that in the amorphous phase, the polythiophene derivative P3MEET bearing oligoethylene glycol side chains with oxygen directly attached to the thiophene rings possesses lower Li^+ ionic conductivity compared to its analog P3MEEMT that has a methyl spacer between the oxygen and the thiophene rings. Structural characterization of P3MEET and P3MEEMT thin film upon blending with LiTFSI indicates that adding LiTFSI expands the side chain domains of the polymer crystallites and reduces the total degree of crystallinity at the same time. Moreover, LiTFSI is found to infiltrate both the amorphous and crystalline regimes at low concentrations but preferably

resides in the amorphous domain at high LiTFSI concentrations. Ionic transport measured by electrochemical impedance spectroscopy in both P3MEET- and P3MEEMT-LiTFSI thin films is found to occur predominately in the amorphous domain, and ionic conductivity in P3MEEMT-LiTFSI is always higher than in P3MEET-LiTFSI samples, consistent with predictions from MD simulations. Our work provides a platform to predict and study the influence of polymer chemistry on the ionic conductivity of conjugated polymers.

3.1 Introduction

Due to their solution processability, mechanical flexibility and the fact that facile molecular design/synthesis strategies can be readily employed to tailor their optical and electronic properties, conjugated polymers continue to be of interest in scientifically and commercially diverse applications.[15,16,142–145] Traditionally, the electronic transport functionality of conjugated polymers have long played a vital role in the advancement of organic electronics applications such as xerography,[146] organic light-emitting diodes (OLEDs),[147,148] organic thin-film transistors (TFTs)[144] and organic photovoltaics (OPVs).[149,150] More recently, conjugated polymers have also made their way into many novel electrochemical applications that require simultaneous electronic and ionic conducting capability raging from bioelectronics[151–154] to energy applications including batteries,[155,156] pseudo capacitors,[157] electrochromic windows,[158] dye-sensitized solar cells[159], and mechanical actuators.[160] In addition to the inherent advantages over their inorganic counterparts, the "soft" nature of conjugated polymers and other organic materials enables the high quality interface between biological entities and electronics, rendering them particularly useful for bioelectronics applications.[152,161]

The key performance metrics of devices based on mixed ionic/electronic polymeric conductors such as mechanical, electrical or biological responses rely on electronic and ionic transport, which are strongly bound to the morphology of the polymers. Therefore, designing high performance mixed conducting polymers requires an understanding of the interplay between polymer chemistry, processing, and morphology on the ionic and electronic conduction characteristics.[50] In contrast to inorganic semiconductors where the atoms are covalently bonded, the weak intermolecular bonding between macromolecular chains in conjugated polymers results in numerous degrees of conformational freedom, giving rise to their complicated microstructures. The typical structure of conjugated polymers is semicrystalline, consisting of crystalline/aggregate domains embedded in a disordered amorphous matrix. Past work has shown convincing evidence suggesting that electronic carriers traverse mainly through the crystalline domains and only occasionally transport through amorphous domains via bridging tie-chains.[162–166] Ionic transport in conjugated polymers, however, has been explored only on a limited basis. Studying ion transport in conjugated polymer has remained a challenging task due to the dominance of electronic transport over ionic transport which renders most of the common techniques used to measure ion transport ineffective. Additionally, most of the ion transport studies on conjugated polymers have been performed on poly(3,4-ethylenedioxythiophene) doped with poly(styrenesulfonate) (PEDOT: PSS) which has a rather complicated structure, preventing its use as a model system for structure-function relationship studies.[52,66,167] Despite recent work focusing on developing "non-PEDOT" conjugated polymers having polar side chains and ion-conducting functionality,[69,137,168] detailed investigations on the influence of polymer chemistry on ion uptake, polymer morphology and ionic transport are still lacking.

To this end, in this work we report a systematic investigation on influence of ion uptake on structure and ion conducting behavior of two polythiophene derivatives bearing different oligoethylene glycol side chains. Using molecular dynamics (MD) simulation, we show that

P3MEET, a polythiophene derivative bearing oligoethylene glycol side chains with an oxygen bonded directly to the thiophene rings, has lower segmental mobility compared to its analog P3MEEMT that have a methyl spacer between the oxygen and thiophene rings. Consequently, the Li^+ ions conductivity in amorphous P3MEEMT is predicted to be approximately a factor of 5 higher than in amorphous P3MEET. Structural characterization of P3MEET and P3MEEMT thin film upon blending with lithium bis(trifluoromethanesulfonyl)imide (LiTFSI) indicates that LiTFSI infiltrates into both crystalline and amorphous domains at low LiTFSI concentration but preferably resides in amorphous domain at high LiTFSI concentration. The ionic conductivity is determined experimentally using electrochemical impedance spectroscopy (EIS) due to the relatively high ionic conductivity over electronic conductivity of both polymers. Using a combination of simulation and experiment results, we infer that ionic transport in both P3MEET and P3MEEMT occurs in amorphous domain. Moreover, in excellent agreement with our MD simulation prediction, the experimental ionic conductivity in P3MEEMT is always higher than in P3MEET at all temperatures and concentrations studied. Our results highlight the importance of side chain chemistry in dictating ionic transport of conjugated polymers.

3.2 Experimental

3.2.1 Materials and Sample Preparation

P3MEET and P3MEEMT were synthesized by first synthesizing the monomers 2,5-dibromo-3-(methoxyethoxyethoxy) thiophene [3MEET] and 2,5-dibromo-3-(methoxyethoxyethoxymethyl) thiophene [3MEEMT], then polymerizing using Kumada Catalyst Transfer Polymerization (KCTP). Additional synthetic details are provided in the results and discussion section.

All substrates used in this study were cleaned by ultrasonication in acetone and 2-propanol for 15 min in each solvent, followed by ozone-plasma treatment for 3 min. Grazing incidence wide angle

X-ray scattering (GIWAXS) and spectroscopic ellipsometry measurements were performed on films deposited on Si substrates with 1.5 nm of native SiO_2. UV-vis absorption measurements were performed on films deposited on glass substrates. Conductivity measurements were performed on films deposited atop custom-fabricated, 1000 nm thick interdigitated gold electrodes on Si substrates.

Solutions of P3MEET and P3MEEMT were prepared by dissolving the materials in anhydrous chloroform and anhydrous acetonitrile, respectively, at a concentration of 10 mg/mL and stirred overnight before being filtered through a 0.45 µm filter. Bis(trifluoromethane)sulfonimide lithium salt (LiTFSI) (Sigma Aldrich, battery grade) was dissolved in anhydrous acetonitrile, also with a concentration of 10 mg/mL. P3MEET, P3MEEMT and LiTFSI solutions were then mixed at the appropriate ratios to achieve different LiTFSI blending concentrations: $r = [Li^+]/[EO] = 0$ (neat sample), 0.01, 0.05, 0.10 and 0.15. The mixed solutions were then stirred for several hours before being spin coated under a nitrogen atmosphere onto the prepared substrates at 2000 rpm for 2 min. Film thicknesses of all samples in this study were kept at *ca.* 50 nm, as confirmed by spectroscopic ellipsometry measurement.

3.2.2 Electrochemical Impedance Spectroscopy (EIS)

Electrochemical Impedance Spectroscopy (EIS) measurements were performed on sample fabricated on top of interdigitated gold electrode devices (IDE) using a Gamry 600+ Potentiostat inside an argon-filled glovebox. An optical image of the IDE device is exemplified in Figure 3.7a. Prior to conductivity measurements, the excess amount of materials on the electrode pads was scraped away. The electrical connection from the IDE to the Potentiostat was made using two custom-built microprobes. The EIS characterization was performed from 1 MHz to 0.1 Hz with an oscillatory peak potential of 100 mV. The collected impedance data were then fit to the appropriate equivalent circuits in order to extract the sample ionic resistance, R_{ion}, and electronic resistance, R_e, from which the ionic conductivity can be calculated. More details of selecting equivalent circuits and conductivity calculations are presented in the Results and Discussion section.

3.2.3 Grazing Incidence Wide-Angle X-Ray Scattering (GIWAXS)

GIWAXS measurements were performed at beamline 8-ID-E of the Advanced Photon Source, Argonne National Laboratory with 10.86 keV ($\lambda = 0.11416$ nm) synchrotron radiation. Samples were enclosed and measured inside a low vacuum chamber (10^{-3} mbar) to minimize concerns about radiation damage as well as to prevent extraneous scattering from ambient air. The measurement time was chosen to be 10 s per frame. For each sample, 3 data sets were taken from 3 adjacent spots on the sample and then summed in order to enhance the signal-to-noise ratio. In our work, the samples were tilted at an angle of incidence of 0.14° with respect to the incoming beam. This angle was chosen to be above the estimated critical angle of sample (*ca.* 0.13°) but below the critical angle of the Si substrates (*ca.* 0.17°). The scattering signal was recorded with a Pilatus 1MF pixel array detector (pixel size = 172 µm) positioned 228 mm from the sample. Each data set was stored as a 981x1043 32-bit tiff image with 20-bit dynamic range. The Pilatus detector has rows of inactive pixels at the border between detector modules. In order to fill these gaps, after each measurement the detector was moved to a new vertical direction and the measurement on each spot was repeated, then the gaps were filled by combining the data from two detector positions. The signals were reshaped and output as intensity maps in q_z vs q_r ($= \sqrt{q_x^2 + q_y^2}$) space. We also performed detector nonuniformity, detection efficiency, the polarization effect and solid-angle variation for each image. Vertical line-cuts were performed as a function of intensity along the q_z direction. All the GIWAXS data processing and extraction were executed using the GIXSGUI package for MATLAB.[169]

To construct the pole figure of the (100) reflection in each sample, wedge cuts with an angular breadth of 1° were extracted from GIWAXS images, performed using GIXSGUI. Each wedge cut was first fit to an empirical baseline function in order to enable the background intensity and amorphous scattering to be subtracted. The background-subtracted wedge cut was then fit to a Voigt function in order to extract the integrated intensity as well as the position of the reflection of interest, q_{100}. The integrated intensity of each peak was reported as a function of the polar angle χ between the scattering vector and pole vector (substrate normal). Additional details of the complete pole figure construction can be found elsewhere.[170]

3.2.4 UV-Vis Absorption Spectroscopy

The UV−vis absorption spectroscopy measurements were performed using a Shimadzu UV-3600 Plus UV-VIS-NIR Dual Beam Spectrophotometer at the Soft Matter Characterization Facility (SMCF) at the University of Chicago.

3.2.5 Size Exclusion Chromatography

Size exclusion chromatography (SEC) was performed using a Malvern Viscotek TDA 305 with a coupled UV-Detector, with a detector temperature of 30 °C. Chloroform with a 1.0 mL/min flow rate was used as an eluent, with sample concentrations of 1 mg/mL. Molecular weight of the polymers was measured relative to polystyrene standards.

3.2.6 Nuclear Magnetic Resonance Spectroscopy

NMR Spectroscopy was performed using a Bruker AV 300 instrument for small molecule studies, and a Bruker AV 500 for polymer studies. All experiments were performed at 25 °C in $CDCl_3$.

3.3 Results and Discussion

3.3.1 Computational Simulation

In the first phase of our investigation, we employ molecular dynamics (MD) simulations to search for relevant chemistries in order to guide complementary synthesis and characterization efforts. We chose to use polythiophene derivatives due to the vast literature available on their structure and charge transport models.[36,165,171–174] Additionally, the morphological structure of polythiophene can be investigated with common techniques such as X-ray scattering or optical methods.[172,175,176] To introduce ion conducting functionality into polythiophene, we attach polar oligoethylene glycol side chains to the polythiophene backbone. The originally proposed chemistry, P3MEET (left side of Figure 3.1a), consists of a thiophene backbone and an oligoethylene glycol side chain with an oxygen atom directly bonded to the thiophene ring. Although placing the electron donating oxygen atom right next to the thiophene core is known to reduce the ionization energy and improve electrochemical stability of the polymer,[69,137,177] it could negatively impact the ionic conductivity due to the reduced segmental motion of the oxygen atom covalently bonded to the rigid polythiophene backbone. Thus, to improve ion transport, a second chemistry, P3MEEMT (right side of Figure 3.1a), is proposed. P3MEEMT is chemically very similar to P3MEET but possesses a methylene spacer between the backbone and the first oxygen atom of the oligoethylene glycol chain.

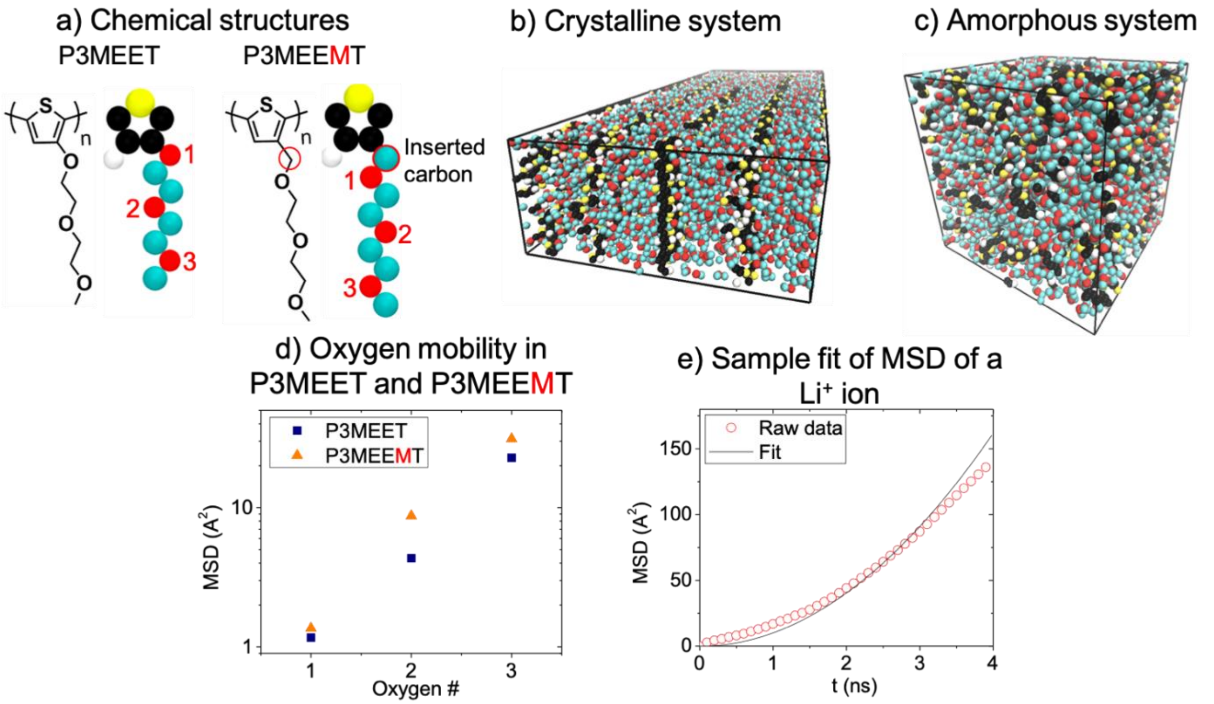

Figure 3.1: (a) Chemical structures of P3MEET and P3MEEMT. (b) (c) Snapshots of equilibrated crystalline and amorphous systems used in this study. (d) Long-time plateau mean square displacement (MSD) of 3 oxygen atoms in the side chain of P3MEET and P3MEEMT. The oxygen # is noted in (a). (e) A typical plot of the MSD of a mobile Li+ ion within P3MEEMT crystalline system and the fit used to calculate ion mobility

Due to the semicrystalline nature of conjugated polymers, we use MD simulations to predict ion conductivity in the two limiting scenarios of purely crystalline and amorphous systems. To simulate the systems of interest, a hybrid all-atom (AA)/united-atom (UA) model is used where the ring is simulated with the OPLS-AA forcefield, while the side chains are modeled using the OPLS-UA forcefield, as shown in Figure 3.1a. The AA model is used for he thiophene rings as it is better suited to capture the ring-ring stacking. The side chains are modeled with the UA model for computational efficiency. Parameters for the model are given in the supplementary information (SI).

Different methods were used to obtain equilibrated structures of the phases of interest. For the crystalline phase, the initial configuration was equivalent to the crystalline structure of poly(3-hexylthiophene) (P3HT) (Isomorph I)[178] except that the crystals of both P3MEET and P3MEEMT were expanded to accommodate the longer side chains. The system was thermalized at 300 K and

1 atm (using the Nosé-Hoover barostat[179]) until metrics such as $E_{non\text{-}bonded}$, E_{bonded}, and the pressure tensor components become time-independent. For amorphous configurations, a CG model[180] which represents the ring as one bead, and the hexyl side chain as two beads was adapted to model poly-(3-nonylthiophene) (P3NT) by adding another bead to the side. Once the CG systems were equilibrated, an in-house reverse coarse graining code was used to generate a configuration of the UA/AA model. This configuration was then allowed to also equilibrate at 300 K and 1 atm. Snapshots of the equilibrated crystalline and amorphous morphology of P3MEEMT are given in Figure 3.1b and c. Crystalline and amorphous structures of P3MEET appear similar and are thus not shown.

Former studies on the ionic conductivity in polymer electrolytes have correlated higher chain segment mobility with greater ionic conductivity.[181,182] Thus, after equilibrating the crystalline and amorphous structures, we investigated the segmental mobility of P3MEET and P3MEEMT side chains by calculating the mean square displacement (MSD) of the three oxygen atoms in their side chains as depicted in Figure 3.1a.We expectedly found that the MSD of each atom increases and then plateaus beyond a certain time period since the side chain is covalently bound to the rigid polythiophene backbone (see Supporting Information). Figure 3.1d shows the plateau MSD of the three oxygens in ion-free P3MEET and P3MEEMT crystalline systems. For both polymers, the MSD of the oxygen atom expectedly increases with greater distance (from the anchoring thiophene backbone) along the oligoethylene side chain. Moreover, adding the carbon spacer in P3MEEMT increases the MSD, and hence the segmental mobility of oxygen atoms at corresponding positions relative to P3MEET for both crystalline and amorphous systems.

To calculate the ionic conductivity, free Li^+ ions were added to the systems at a concentration $r = [Li^+]/[EO] = 0.02$ and their mobility tracked upon the application of a large electric field of 500

MV/m. The choice of r is such that ions are sufficiently dilute to minimize ion-ion interactions, but also abundant enough to allow for good statistical sampling. Free Li^+ ions are used instead of entire salts to avoid the need to simulate the very long time-scale associated with salt dissociation. This implicitly assumes a 100% dissociation ratio which is a sensible assumption for LiTFSI in PEO-like environments. The electric field value chosen is large enough to allow for good sampling of the ionic motion (given the accessible simulation time scale), but still sufficiently moderate to yield a linear response behavior (Ohm's law). While applying such a large electric field, a tethering potential was used to keep the thiophene backbones near their original positions and avoid destroying the overall microstructure. Simulations were run for 30 ns in a constant volume ensemble with a set temperature of 400 K to allow for better sampling. For calculating the ionic conductivity $\langle m \rangle$, three replicate simulations were run and only "mobile" ions are considered, i.e., those showing a parabolic dependence of MSD on time as in the example plotted in Figure 3.1e. For such ions, the MSD dependence is fitted to the following equation from which the ionic mobility $<\mu>$ can be extracted:

$$MSD \approx (vt)^2 = (E\mu)^2 t^2 \qquad \text{Equation 3.1}$$

Where v, t, and E, are drift velocity, time, and electric field strength, respectively. The ionic conductivity, $\hat{\sigma}$, is then calculated as:

$$\hat{\sigma} = \langle \mu \rangle \langle N_{mobile} \rangle \qquad \text{Equation 3.2}$$

where $\langle N_{mobile} \rangle$ is the average number of the "mobile" ions. More details of these conductivity calculations can be found in the Supporting Information. We then normalize the conductivity by the conductivity of amorphous P3MEET. The average mobility, fraction of mobile ions and normalized ionic conductivity of P3MEET and P3MEEMT in both crystalline and amorphous systems is summarized in Table 3.1. Interestingly, while in the amorphous phase the normalized conductivity is *ca.* 5 times higher in P3MEEMT than in P3MEET, the trend reverses in the crystal phase; *i.e.*, the normalized conductivity is *ca.* 5 times higher in P3MEET than in P3MEEMT. To explain this behavior, we show in Figure 3.2 a snapshot of P3MEEMT and P3MEET side chain conformation in the presence of Li^+ ions within the crystalline domain. In pure PEO, two chains can form a "cage" around the ion, forming a deep kinetic trap for the ions.[183] A condition of cage formation is that the ion is only coordinated by two side chains, otherwise there are more chains coordinating the ion. To quantify cage formation, we determine the number side chains which have an atom within a 3.5 Å cutoff of each ion and find the average number of atoms which are coordinating the ion. We find these values for P3MEET and P3MEEMT to be 2.47 ± 0.03 and 2.14 ± 0.003, respectively. This agrees with the idea that cage formation is higher in crystalline P3MEEMT, where the regular arrangement of side chains and mobility of the oxygen near the backbone allow for cage formation. In contrast, in P3MEET the lack of mobility for the oxygen near the thiophene backbone reduces the chance of cage formation. In the amorphous systems, ion-trapping cages are more difficult to form because of the irregular arrangement of the side chains. While our simulation results only predict Li^+ ion transport behavior, we expect similar trends with the $TFSI^-$ anion since transport of both ions rely on segmental motion of PEO side chains. Overall, our simulation results indicate the strong influence of side chain chemistry on ionic transport characteristics of semicrystalline conjugated polymers.

Table 3.1: Calculated ion mobility, fraction of mobile ion and normalized ionic conductivity of P3MEEMT and P3MEET in equilibrated crystalline and amorphous systems from MD simulation

	Crystaline P3MEET	**Crystaline P3MEEMT**	**Amorphous P3MEET**	**Amorphous P3MEEMT**
Mobility ($cm^2V^{-1}s^{-1}$)	4.52×10^{-6}	4.00×10^{-6}	1.82×10^{-6}	2.25×10^{-6}
N_{mobile}/N_{total}	0.133	0.031	0.025	0.1
Relative conductivity	13.33	2.78	1	5

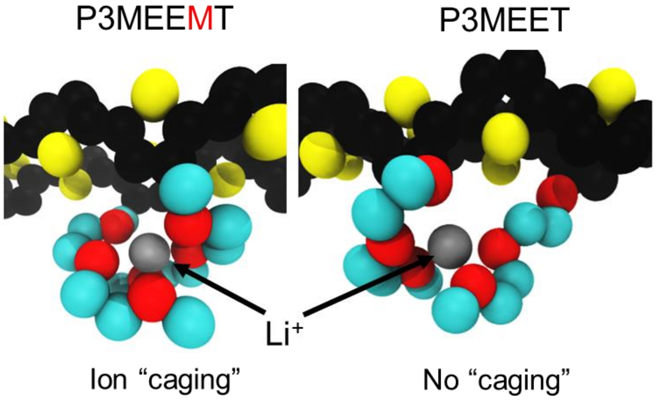

Figure 3.2: Snapshot showing the ion caging that is frequently seen in crystalline P3MEEMT but almost never in crystalline P3MEET.

3.3.2 Synthesis

Motivated by insights learned from computational simulation, we begin to synthesize two polythiophene derivatives, P3MEEMT and P3MEET, following the synthesis pathways described in

Figure 3.3a. Following the successful synthesis of both monomers, P3MEET and P3MEEMT are synthesized using Kumada Catalyst Transfer Polymerization (KCTP), as detailed in

Figure 3.3a. Regioregularity of the P3MEET and P3MEEMT samples were determined to be approximately 95% and 94% by comparing the signals of head-tail and head-head signal in

H^1NMR spectra (See Supporting Information for details). The number average molecular weight (M_n) of the polymers were determined through size exclusion chromatography (SEC); the measured M_n were 12 kg/mol for P3MEET and 15 kg/mol for P3MEEMT. The similarity between these two polymers implies that any difference between the two samples will be due to differences in chemical structures, rather than molecular weight or dispersity.

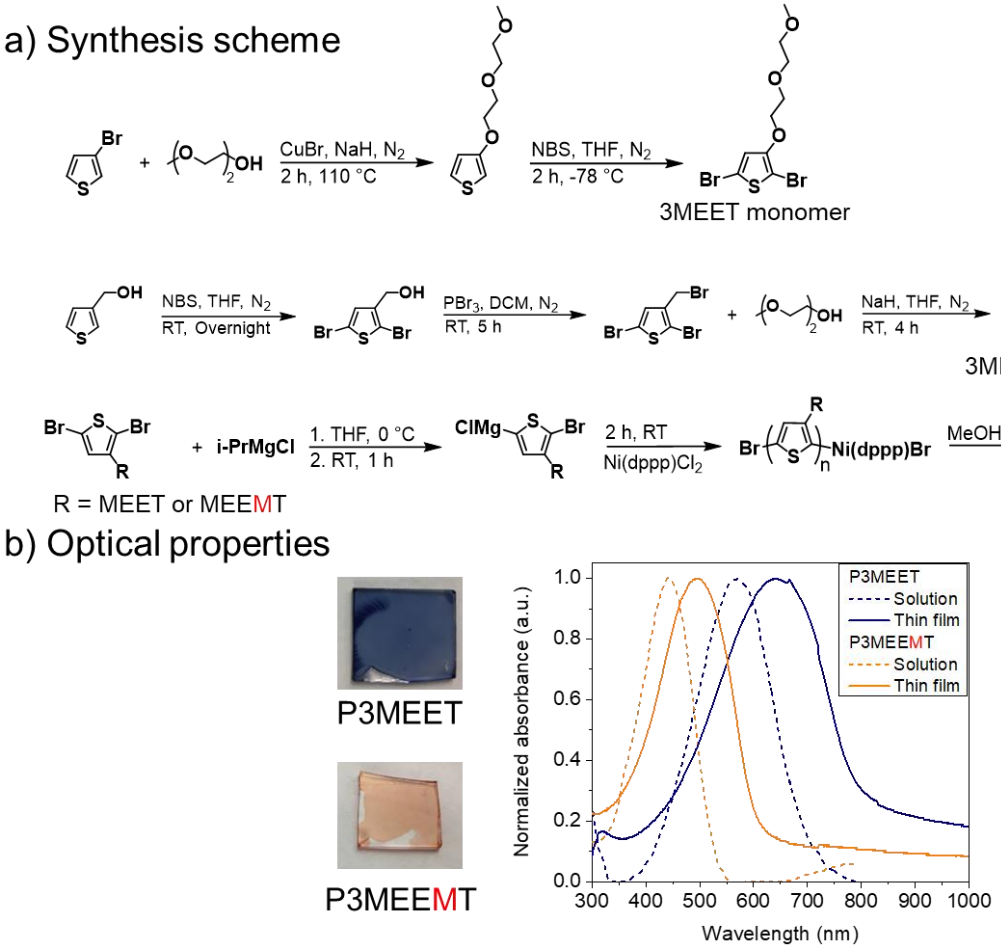

Figure 3.3: (a) Synthesis scheme and (b) Optical images and normalized UV-vis absorption spectra of P3MEET and P3MEEMT both in solution and thin film states

To fabricate thin films of P3MEET and P3MEEMT, we dissolve the polymers in chloroform and acetonitrile, respectively, which are not only good solvents for the polymers but also miscible with LiTFSI solution, allowing for the formation of homogeneous spin casting solutions. Additionally, chloroform and acetonitrile have very similar boiling points, permitting reasonable comparison between P3MEET and P3MEEMT structure, as the boiling point and vapor pressure of casting solvents have strong effects on the final polymer morphology.[184]

Figure 3.3b depicts the optical images as well as the absorption spectra of P3MEET and P3MEEMT in solution and thin film states. Both P3MEET and P3MEEMT exhibit pronounced red-shifts going from solution to solid states, suggesting the aggregation and planarization of their conjugated backbone after spin-casting. Notably, the optical properties of P3MEET are significantly different from P3MEEMT despite only a small difference in side chain chemistry. In the case of P3MEET, placing the oxygen atom right next to the polythiophene backbone results in a marked red-shift in absorption spectra compared to P3MEEMT. This is due to the electronic donating ability of the conjugated oxygen atom to the thiophene core that shifts the ionization energy and lowers the band-gap of P3MEET, similar to previous observations in literature.[137,177]

3.3.3 Influence of LiTFSI Doping on Semicrystalline Morphology of P3MEET and P3MEEMT

In order to study ionic transport in P3MEEMT and P3MEET, we introduce the ionic dopant LiTFSI by spin-casting the blended solutions of P3MEET-LiTFSI and P3MEEMT-LiTFSI onto the desired substrates. AFM images (see Supporting Information) and X-Ray diffraction patterns (as will be discussed below) indicated no signal of LiTFSI aggregation, suggesting that LiTFSI is well-mixed within the polymer matrix. To study the influence of ion addition on the morphological structure of P3MEET and P3MEEMT, we employ grazing incidence wide-angle X-ray scattering (GIWAXS) to investigate the solid-state structure of P3MEET and P3MEEMT thin films as a function of LiTFSI blending concentration r = [Li$^+$]/[EO]. The GIWAXS patterns of P3MEET-LiTFSI thin films are shown in the top row of Figure 3.4.

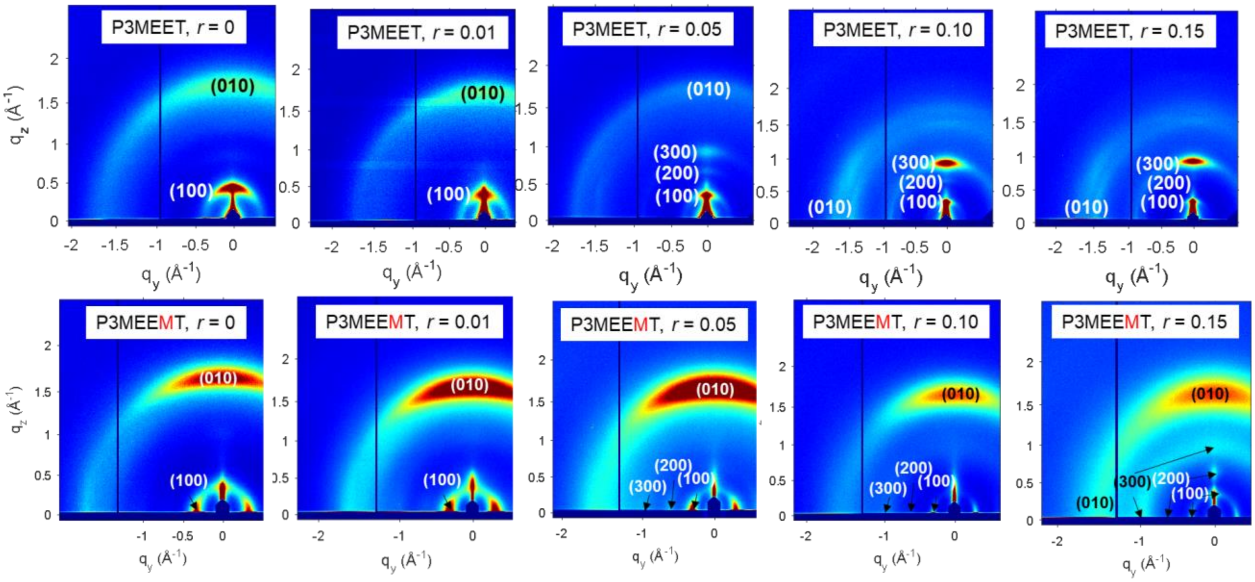

Figure 3.4: GIWAXS patterns of P3MEET (top row) and P3MEEMT (bottom row) at different LiTFSI blending concentration r = [Li$^+$]/[EO].

For the neat P3MEET sample (r = 0), we observe both the side chain stacking peak (100) and π-π stacking peak (010) predominantly in the out-of-plane direction, indicating that P3MEET exhibits a mixed orientation of both "face-on" and "edge-on" orientation of polymer crystallites. Upon introducing LiTFSI, the structure of P3MEET progressively changes. Specifically, we observe the sharpening of the (100) peak together with the appearance of the (200) and (300) peaks for r equal to or large than 0.05, suggesting that P3MEET crystallites become more oriented by the addition of LiTFSI. Additionally, at very high LiTFSI concentration r = 0.10 and r = 0.15, the side chain diffraction peaks (h00) are observed in the out-of-plane direction whereas the (010) is observed mainly in the in-plane direction, indicating that the polymer crystallites mostly adopting the edge-on orientation at these concentrations. Finally, the intensity of the π-π stacking peak (010) also significantly reduces which is indicative of the disruption of interchain π-π stacking upon introducing LiTFSI.

The GIWAXS patterns of P3MEEMT-LiTFSI samples are shown in the bottom row of Figure 3.4. Despite some certain differences, P3MEEMT shows similar transitions to P3MEET upon introducing LiTFSI. In the diffraction pattern of the neat P3MEEMT film, the (100) side chain diffraction peak is predominantly in the in-plane direction whereas the (010) π-stacking diffraction peak is predominantly in the out-of-plane direction, suggesting the bias toward face-on orientation of P3MEEMT. Upon introducing LiTFSI, the (100) peak shape of P3MEEMT becomes sharper together with the appearance of the (200) and (300) peaks, indicating the improvement in the molecular order of P3MEEMT which is similar to P3MEET. One noticeable difference with P3MEET is that the diffracting intensity of the (010) peak still remain relatively high even at the highest LiTFSI concentration $r = 0.15$. This observation suggests that the crystallite structure of P3MEEMT is more resilient to the addition of the ionic dopants.

To quantify the influence of LiTFSI on molecular orientation as well as relative degree of crystallinity (rDoC) of P3MEET and P3MEEMT, we construct partial pole figure of (100) reflection as a function of the polar angle χ between the scattering vector, q_{100}, and the substrate normal. [170,172,185] The integrated intensity at each polar angle was further scaled by the geometrical factor $\sin(\chi)$ to correctly quantify the population of crystallites at a particular orientation.[186] In our experiment, data for $\chi < 2°$ is not available since the reciprocal lattice vector does not intersect with the Ewald sphere in this regime whereas data for $\chi > 83°$ is impacted by standing waves and excluded from our analysis.[175,185] Shown in Figure 3.5a and b are the geometrically corrected partial pole figures of (100) reflection in P3MEET and P3MEEMT, respectively. The pole figure of P3MEET neat sample $r = 0$ shows peak intensity near $\chi = 30°$ and the peak shifts to lower value of χ with increasing r, indicating that P3MEET crystallites transition from face-on dominated to edge-on dominated orientation upon introducing LiTFSI. Similarly, the pole figures of P3MEEMT samples show a peak near $\chi = 90°$ for $r = 0, 0.01, 0.05, 0.10$ but the peak shifts to $\chi \sim 0°$ for $r = 0.15$ sample, suggesting that the crystallites of P3MEEMT also shift to edge-on orientation at high

LiTFSI concentration. These outcomes agree with visual inspection using raw detector images in Figure 3.4.

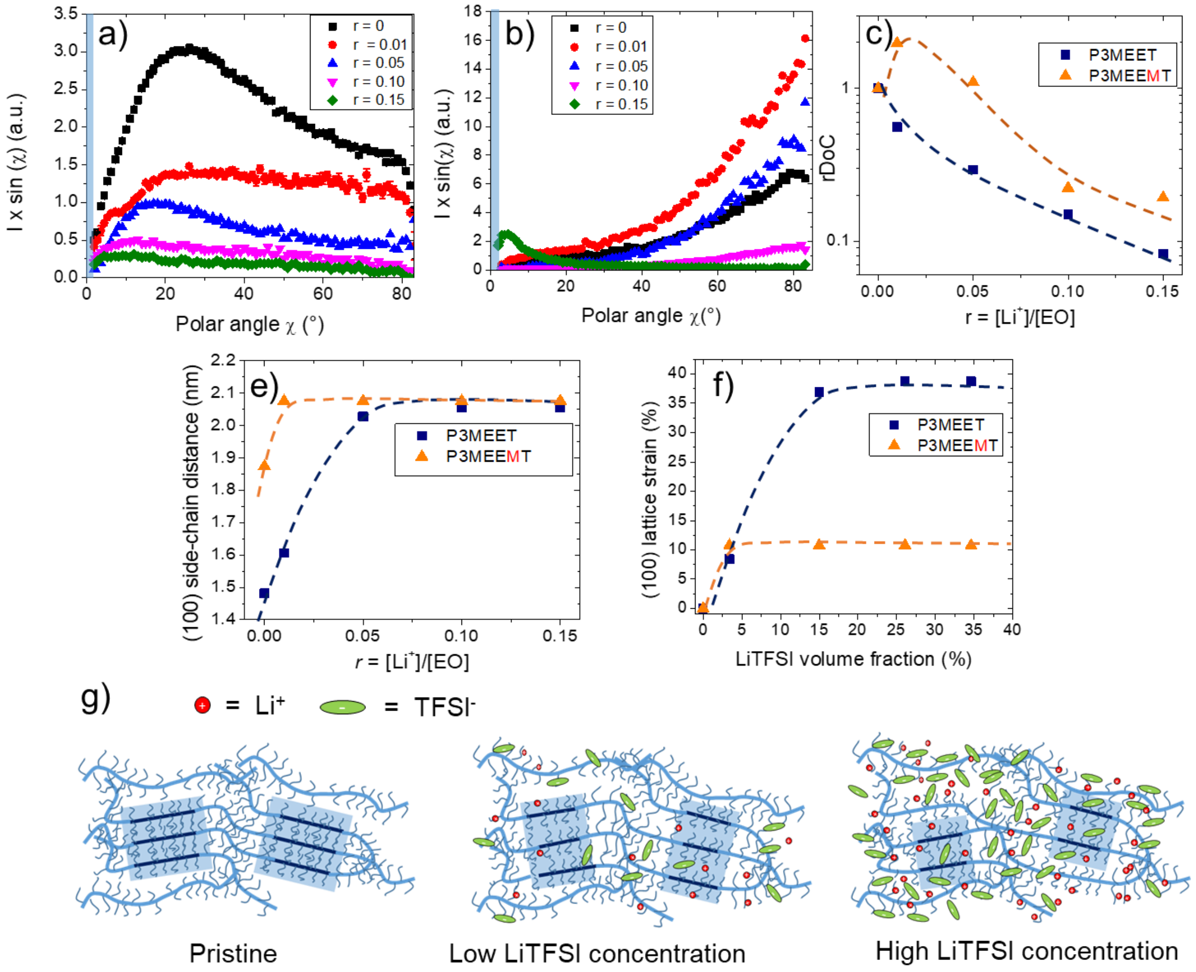

Figure 3.5: (a)(b) Partial pole figures of (100) reflection in P3MEET and P3MEEMT samples at different LiTFSI concentration. The shaded areas in figure (a) and (b) denote the non-measurable regime of our experiments. (c) Calculated relative degree of crystallinity (rDoC) of P3MEET and P3MEEMT as a function of LiTFSI concentration. (e) Side chain stacking distances and (f) Calculated lattice strain of P3MEET and P3MEEMT as a function of LiTFSI concentration and volume fraction. (g) Schematic representation of LiTFSI distribution within P3MEET/P3MEEMT semicrystalline structure. LiTFSI infiltrates both crystalline and amorphous domains at low concentration but preferably resides in the amorphous domain at high concentration.

Following previously described procedures,[185,186] the rDoC of each sample is calculated by integrating the partial pole figures and then normalized by the volume fraction of polymer in polymer-LiTFSI mixtures. To facilitate accurate rDoC comparison, all samples were made at approximately the same thickness (*ca.* 50 nm). In addition, X-ray beam footprint and exposure time were kept the same for all samples. For each polymer, we further normalize the rDoC by the rDoC of the neat sample (r = 0) to emphasize the effect of LiTFSI addition on rDoC. Shown in Figure 3.5c is the normalized rDoC of P3MEET and P3MEEMT as a function of LiTFSI concentration r. For P3MEET, the rDoC is found to quickly diminish by the addition of LiTFSI (note the log scale of y axis). Interestingly, the rDoC of P3MEEMT is found to initially increase, r = 0.01, before starting to decrease with further increasing LiTFSI concentration. This behavior is in fact similar to recent work by Guardado and Salleo where they reported a slight increase and then decrease in rDoC of P3HT upon injecting TFSI$^-$ ions.[187] Here, it is worth noting that for the same LiTFSI concentration, the estimated rDoC of P3MEEMT sample is always higher than P3MEET. For example, at the highest LiTFSI concentration, r = 0.15, the rDoC of P3MEET is *ca.* 7% compared to the pristine sample whereas rDoC of P3MEEMT is *ca.* 20%. In other words, adding LiTFSI into P3MEET has a stronger impact on the polymer crystallinity as compared to P3MEEMT.

To further study the influence of LiTFSI addition on the polymer structure, we calculate the side chain distance $l = 2\pi/q_{100}$ and the corresponding lattice strain = $(l - l_0)/l_0 \times 100\%$, the results of which are plotted in Figure 3.5e and f. In this equation, l_0 is the side chain distance in the neat r = 0 sample. For both polymers, the side chain distance and lattice strain do not linearly scale with LiTFSI concentration/volume fraction. For P3MEET, the side chain distance increases initially from 1.48 nm to 2.03 nm but plateaus for salt concentration r higher than 0.05. The side chain distance of neat P3MEEMT is 1.87 nm which is larger than P3MEET, as expected. Upon introducing LiTFSI, P3MEEMT side chain distance increases and saturates at 2.07 nm for r higher than 0.01. A similar trend is observed for (100) lattice strain in Figure 3.5f, where the strain in the side chain direction is found to saturate around ~10% and ~35% in P3MEEMT and P3MEET, respectively. Here it is important to note that the strain induced by ion uptake in both P3MEEMT and P3MEET is much larger than polythiophene derivatives bearing aliphatic side chains, which only strain by a maximum amount of *ca.* 10% upon introducing ions *via* electrochemical doping, a more intensely driven process than chemical mixing.[187–189] The high level of ion uptake along the side chain directions of P3MEET and P3MEEMT crystallites could be attributed to the high polarity of their EG side chains, and the relative openness of the EG side chain structure. Additionally, the higher lattice strain of P3MEET indicates that P3MEET crystals uptake more ions than P3MEEMT. This outcome is further supported by our previous observation of raw GIWAXS patterns and rDoC where P3MEEMT crystalline structure appears to be more “resilient” to the addition of LiTFSI than is P3MEET.

The influence of LiTFSI uptake on rDoC and lattice strain has significant implication on the distribution of LiTFSI within the semicrystalline morphology of both polymers. Since GIWAXS is only sensitive to crystalline domains, any changes in the structure of the amorphous regimes caused by the presence of LiTFSI are not sensible by GIWAXS. At low LiTFSI concentration, because the crystalline lattice strain increases with *r*, we postulate that LiTFSI infiltrates both the crystalline and amorphous domains. However, at high salt concentration we see saturation of the lattice strain and likewise the amount of LiTFSI in the crystalline domain in addition to the reduction in the overall rDoC of both polymers. We thus conclude that in the high concentration regimes crystallites are “filled” with ions and the majority of additional LiTFSI preferably resides in the lower density amorphous regime. As a result, no increase in side chain distance is observed by GIWAXS. The LiTFSI distribution within the semicrystalline domains of P3MEET/P3MEEMT is illustrated in Figure 3.5g.

Since electronic charge transport depends heavily on the ability of carrier to hop via the π-stacking direction, it is important to study the influence of LiTFSI addition to the π-π interaction between polymer chains. Shown in Figure 3.6a and b are the horizontal line-cuts of P3MEET and vertical line-cuts of P3MEEMT at different LiTFSI concentrations. We study the π-π interaction using the horizontal line-cuts for P3MEET but vertical line-cuts for P3MEEMT since P3MEET crystallite adopts mostly edge-on orientation but P3MEEMT crystallite adopts mostly face-on orientation at all LiTFSI concentrations. As shown in Figure 3.6a, the horizontal line-cut of P3MEET show a strong π-π stacking peak (010) near q = 1.60 $Å^{-1}$ which correspond to a π-π stacking distance of *ca.* 0.39 nm. Upon adding LiTFSI, we observe the appearance of two extra diffraction peaks, denoted A and B, as indicated by the dashed arrows in Figure 3.6a. Since the position of peak A doubles the position of B ($q_A \sim 2 \times q_B$), it is likely that peak A is a higher order peak of peak B. We hypothesize that a small amount of Li^+ ions within the crystalline domain can intercalate between the π-stacks, increase the pi-stacking distance from 0.39 nm to *ca.* 0.88 nm. In stark contrast, the π-stacking distance of P3MEEMT only mildly increases from *ca.* 0.38 to 0.39 nm from $r = 0$ to $r = 0.15$, suggesting that the crystallite structure of P3MEEMT is less sensitive to addition of LiTFSI compared to P3MEET, consistent with the smaller uptake amount of LiTFSI in the side chain direction presented above. The slight broadening and shifting of the P3MEEMT π-stacking peak at high salt concentrations most likely originates from the presence of LiTFSI in the side chain and/or in the surrounding amorphous domain. The lack of the signature of the intercalation of Li^+ ions into the π-stacks of P3MEEMT could be due to the farther distance from the nearest oxygen atom to the thiophene backbone. Thus Li^+ ions coordinating with oxygen have lower probability of intercalating and disrupting the π-stacking efficiency in P3MEEMT. This finding again shows the strong influence of side chain chemistry on the morphological structure and the ion uptake ability of conjugated polymers.

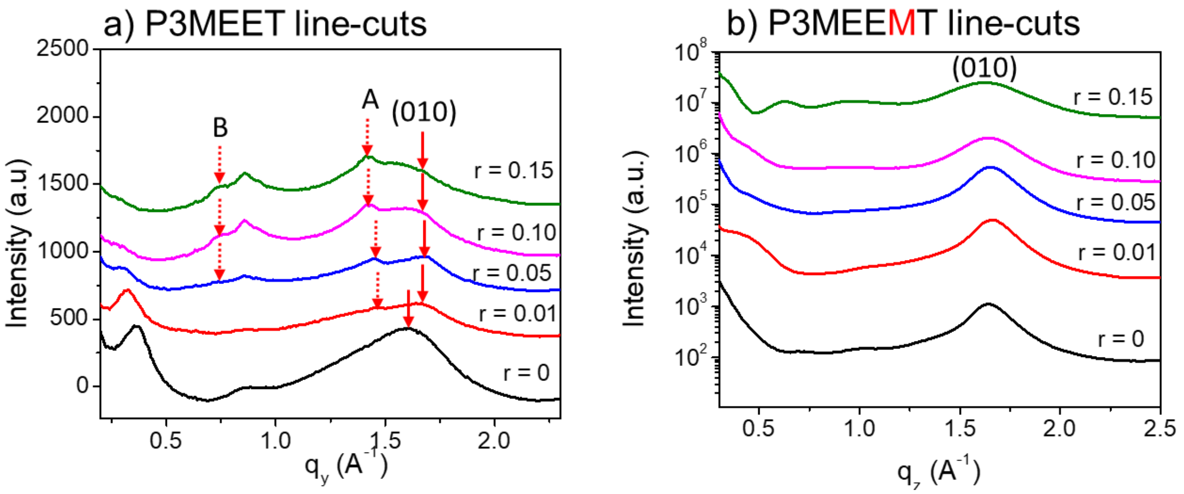

3.3.4 Ion Transport in LiTFSI-doped P3MEET and P3MEEMT Thin Films

Figure 3.6: (a) Horizontal line-cuts from GIWAXS patterns of P3MEET b) Vertical line-cuts from GIWAXS patterns of P3MEEMT at different LiTFSI concentrations. The intensity of the line-cuts was shifted vertically for clarity.

To preface our discussion on ion transport of P3MEET and P3MEEMT, we would like to note that up to date, measuring ion transport in conjugated polymers has remained a challenging task. This is due to the dominance of electronic transport over ionic transport, which obstructs the use of the common ion conductivity measurement techniques such as electrochemical impedance spectroscopy (EIS). Most ionic transport studies were performed using the moving-front experiment developed by Malliaras,[66] which only works on electrochromic polymers such as PEDOT:PSS. Here, by using high ionic conductivity polymers, carefully purifying our polymers to reduce the amount of electronic carriers and performing experiment in oxygen and water-free environment, we are able to measure ionic conductivity of both P3MEET and P3MEEMT using EIS. We perform EIS measurements on *ca.* 50 nm P3MEET-LiTFSI and P3MEEMT-LiTFSI thin film samples fabricated on top of interdigitated electrode devices (IDEs) whose design is shown in Figure 3.7a. IDEs were employed to increase the effective surface area and enhance signal-to-noise ratio in thin film conductivity measurement.[190–193]

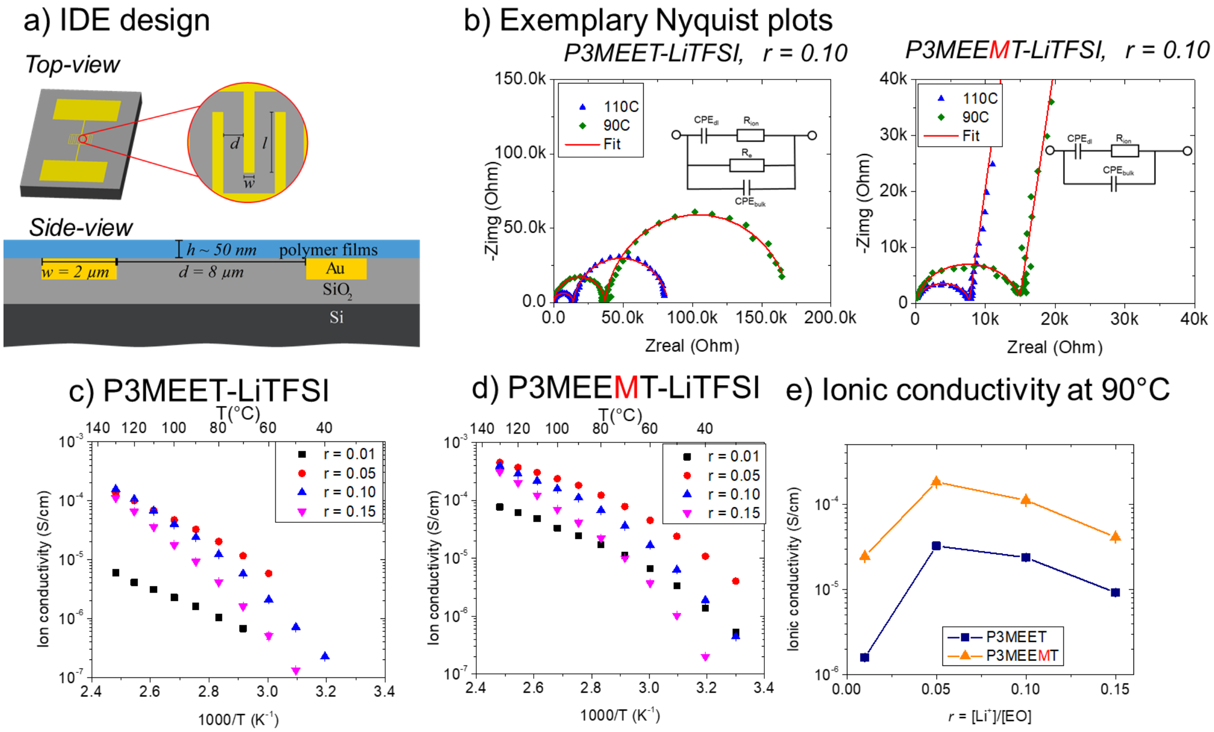

Figure 3.7: (a) Design of IDE devices used for our EIS measurement (b) Exemplary Nyquist plots of P3MEET-LiTFSI and P3MEEMT-LiTFSI samples at r = 0.10. The inset of each figures shows the simplified equivalent circuits used to fit the impedance data. (c), (d) LiTFSI concentration and temperature dependence ionic conductivity of P3MEET and P3MEEMT samples. (e) Comparison of P3MEET and P3MEEMT ionic conductivity at 90°C.

Shown in Figure 3.7b are exemplary Nyquist plots of both P3MEET-LiTFSI and P3MEEMT-LiTFSI samples at LiTFSI concentration $r = 0.10$ at two different temperature. The Nyquist plots of P3MEET-LiTFSI samples consist of 2 semicircles without the capacitive tails and low frequency, indicating the presence of both ion and electron conducting behavior.[15,16] The simplified equivalent circuit used to fit the EIS data is shown in the inset of the figure. Since gold is a blocking electrode for ions, the ionic conduction is represented by a constant phase element CPE_{dl} in series with an ion resistance R_{ion}. Additionally, because ionic and electronic carriers are expected to transport simultaneously within the sample, the equivalent circuit also consists of an electronic resistance R_e in parallel to the ionic resistance. With increasing temperature, the radii of both semicircles reduce due to the enhance in both ionic and electronic conductivity as expected. Fitting the EIS data using this equivalent circuit demonstrates excellent agreement to the raw data, suggesting that our model accurately represents ion and electron transport within the sample. The Nyquist plots of P3MEEMT-LiTFSI sample on the other hand consist of a semicircle whose radius also reduces which increasing temperature, and a capacitive tail at low frequency. This behavior is widely observed in polymer electrolyte-LiTFSI blends,[15,194] which is indicative of the domination of ionic transport in P3MEEMT-LiTFSI sample. The equivalent circuit used to fit P3MEEMT-LiTFSI impedance data thus does not include the electronic resistance R_e and also shows strong agreement to the raw EIS data.

Here it is interesting to note the differences in EIS data of P3MEET and P3MEEMT. The impedance data indicates that P3MEET processes some "intrinsic" electronic carrier conductivity, whereas P3MEEMT does not. This behavior is observed over several polymer batches that we made. Usually the "intrinsic" electronic conductivity of conjugated polymers originates from chemical defects such as fraction of oxidized segments along the polymer backbone, unexpected chemical species associated with the chain ends or leftover catalysts during the synthesis. In our work, P3MEET and P3MEEMT were synthesized, purified and handled in almost identical way thus we do not expect significant differences in the amount of defects/impurities presented in the materials. The differences between P3MEET and P3MEEMT therefore most likely originate from the difference in the chemistries of the two polymers. In P3MEET, the oxygen directly attached to the thiophene core can stabilize the electronic carriers (i.e. holes) which give rise to its electronic conducting states.[161] Therefore P3MEET-LiTFSI samples possessed dual conduction characteristics whereas P3MEEMT-LiTFSI samples only showed ion dominated transport behavior.

By fitting the EIS data to the equivalent circuit, we extract the ionic resistance R_{ion} and calculate ionic conductivity according to the following equation:[190]

$$\sigma = \frac{1}{R_{ion}} \frac{d}{l(N-1)h} \qquad (3)$$

In equation 3, $d = 8$ μm is the separation distance between electrode teeth, $l = 3000$ μm is the tooth length, $N = 480$ is the number of electrodes and h is the total thickness of the sample. The extracted ion conductivity as a function of temperature and LiTFSI concentrations of P3MEET and P3MEEMT is shown in Figure 3.7c and d, respectively. The ionic conductivity of both polymers rapidly increases at low LiTFSI concentration, from $r = 0.01$ to $r = 0.05$, but decrease from concentration $r = 0.05$ to $r = 0.15$. This behavior is expected and aligns with the current ion transport theories for polymer electrolytes. The increase in ion conductivity at low concentration is due to the increase in ionic carrier concentration, whereas the decrease of the conductivity at higher salt concentration originates from (i) the reduction in the dissociation rate of LiTFSI and (ii) increasing the effective glass transition temperature of the materials due to transient cross-linking between Li^+ ion and oxygen molecules of PEO side chains. This effect is particularly more pronounced at low temperature where the temperature approaches the glass transition temperature, as illustrated in both the ionic conductivity data of P3MEET and P3MEEMT. To emphasize the effect of side chain chemistry on ionic transport, we plot in Figure 3.7e the representative concentration dependence ion conductivity of both polymers at 90°C. At all LiTFSI concentration and temperature studied, the ionic conductivity is always higher in P3MEEMT compared to P3MEET. Our finding highlights the significant role of side chain chemistry on ionic transport of polymer electrolytes.

An important question to be addressed is whether ionic transport in conjugated polymers occurs in the crystalline or amorphous regions of the polymer. We postulate that in our samples, ionic

transport happens mainly in the amorphous regimes based on several key observations. First, our simulation results indicated that in P3MEEMT ion transport is better than P3MEET in amorphous region but poorer in crystalline region (see Table 3.1). Since the ion conductivity is higher in P3MEEMT at all conditions studied, it is highly likely that the majority of ion transport occurs in amorphous regime. Moreover, our DSC results clearly indicated several crystallite melting transitions in P3MEEMT (See Supporting Information), yet no obvious transition was observed in the ionic conductivity data. This suggests that most of the contribution for ionic conductivity came from the highly disordered amorphous regime. Finally, our GIWAXS data shows that at high LiTFSI concentration, the amount of LiTFSI within the crystalline regimes stays almost the same for both P3MEET and P3MEEMT, yet the ionic conductivity for both polymers followed the trend one would expect for concentration dependence behavior. This further corroborates our conclusion that in our P3MEET and P3MEEMT samples, ions mainly traverse through the amorphous domain. Interestingly, our simulation predicted better ionic conductivity in crystalline P3MEET yet ion transport is still showed to happen mostly in the amorphous. We suspect that our P3MEET and P3MEEMT samples have low degree of crystallinity due to the low boiling point of the casting solvents. This argument is supported by the lack of the "aggregate shoulder" in the absorption spectra of both polymers (
Figure 3.3b). Since most of the samples comprised of amorphous polymers, it is not surprising that ion transport is dominated by the amorphous domain. Therefore, the dominance of ion transport in the amorphous domain in our work may not be universal to all conjugated polymers. An accurate picture of ion transport mechanism thus requires a more rigorous study on polymer films with systematically varying degree of crystallinity and will be a subject of investigation in our future study.

3.4 Conclusions

In conclusion, we have performed a systematic study on the connection between morphological structure and ionic conduction characteristics of two polythiophene derivatives P3MEET and P3MEEMT upon blending with LiTFSI. MD simulations showed that oxygen atoms in P3MEEMT side chains possessed higher segmental mobility compared to those of P3MEET, resulting in better Li^+ ion conductivity in amorphous phase. However, ionic conductivity of crystalline P3MEEMT was found to be lower than P3MEET due to the formation of Li^+ ion cages, a feature not observed in P3MEET. Using GIWAXS measurement, we showed that blending P3MEET and P3MEEMT with LiTFSI disturbed their crystalline structure, resulting in lattice strains along the side chain stacking direction and significant drops in rDoC which stronger effect in P3MEET compared to P3MEEMT. Introducing LiTFSI also exerted stronger influence on π-π interaction in P3MEET than in P3MEEMT, which most likely originated from the proximity of oxygen atom in P3MEET to the thiophene rings. Additionally, LiTFSI was found to infiltrate both the amorphous and crystalline domains at low concentrations but preferably resided in the amorphous domain at high LiTFSI concentrations. Temperature dependence studies of ionic conductivity at different concentration r in both P3MEET and P3MEEMT showed ionic conductivity increased from $r = 0.01$ to 0.05 but reduced at higher concentration due to ion pairing and transient cross-linking of PEO side chains to Li^+ ions. Ionic transport was found to occur in amorphous regime, and always higher in P3MEEMT compared to P3MEET, consistent with our prediction using MD simulation. Our results have demonstrated that side chain modification can be a fruitful method to control morphology, ion uptake and ion transport in conjugated polymers. We also expect non-trivial effect of side chain chemistry on electronic transport upon blending with ionic species, as LiTFSI has a different influence on rDoC (Figure 3.5b) and π-π interactions (Figure 3.6) for P3MEET and

P3MEEMT. Side chain engineering is thus expected to be critical in the molecular design of mixed conduction materials. Finally, our approach using computational simulations to guide synthesis and characterization can be an elegant method towards studying the influence of chemistry on self-assembly, structure and ionic/electronic conduction of soft materials.

3.5 Supporting Information

3.5.1 Materials

Diethylene glycol monomethyl ether (DGME) was purchased from Sigma-Aldrich, then distilled and placed over activated molecular sieves before use. Dimethylformamide (DMF) and dichloromethane (DCM) were dried using an SP-1 Stand Alone Solvent Purification System. Tetrahydrofuran (THF) was dried using a PureSolv solvent purification system. N-bromosuccinimide (NBS) was purified by recrystallization from water before use. All other materials used were purchased from Sigma-Aldrich and used as-received.

3.5.2 Synthesis of Monomers

The synthesis scheme of both polymers is shown in the main manuscript. All synthesis was performed under an inert, N_2 atmosphere using standard Schlenk line techniques, and all glassware was dried overnight at 120 °C prior to use. Synthetic methods for 2,5-dibromo-3-(methoxyethoxyethoxy)thiophene and 2,5-dibromo-3-(methoxyethoxyethoxymethyl)thiophene were adapted from literature.[136,195] NMR Spectroscopy was performed using a Bruker AV 300 instrument for small molecule studies, and a Bruker AV 500 for polymer studies. All experiments were performed at 25 °C in $CDCl_3$.

3.5.2.1 Synthesis of 3-(methoxyethoxyethoxy)thiophene

This synthesis was adapted from literature. To a dried 3-neck flask with an addition funnel, NaH (3.60 g, 90 mmol, 1.5 equiv.) and DMF (15 mL) are added. DGME (34 mL, 288 mmol, 4.8 equiv.) was added to the addition funnel, and the flask placed on ice. DGME was added dropwise over 15 min, allowing for the evolution of H_2, then stirred on ice for 1 h. The flask was warmed to room temperature, then CuBr (0.860 g, 6 mmol, 0.1 equiv.) and 3-bromothiophene (5.68 mL, 60 mmol, 1 equiv.) added. The flask was placed in an oil bath and heated to 110 °C, then stirred for 30 min. The reaction progression was monitored *via* thin-layer chromatography (TLC). If residual 3-bromothiophene was observed on TLC, an additional equimolar portion of CuBr was added, and the reaction stirred for another 30 min. Following the reaction, the reaction mixture was poured into a 10% NH_4Cl aqueous solution and extracted three times with hexanes. The organic layer was dried with Na_2SO_4, then filtered. The solvent was removed through rotary evaporation, and then eluted over silica using a 3:2 hexanes:ethyl acetate mixture. Product is recovered in an 80% yield as a pale yellow oil. ^1H NMR (300 MHz, $CDCl_3$) δ 7.13 (dd, 1H), 6.75 (dd, 1H), 6.22 (dd, 1H), 4.10 (t, 2H), 3.81 (t, 2H), 3.68 (t, 2H), 3.55 (t, 2H), 3.36 (s, 3H).

3.5.2.2 Synthesis of 2,5-dibromo-3-(methoxyethoxyethoxy)thiophene

To a round bottom flask, 3-(methoxyethoxyethoxy)thiophene (9.76 g, 48 mmol, 1 equiv.) and anhydrous THF (165 mL) were added. The flask was then covered with foil. The flask was placed in a dry ice/acetone bath, and cooled for 5 minutes, then NBS (18.8 g, 105.6 mmol, 2.2 equiv.) was added quickly, and in one portion. The flask was kept at -78 °C for 30 min, then allowed to warm to room temperature and stirred for 1.5 h. Following reaction completion, solvent is removed from the covered flask. The flask was then washed with hexanes and filtered over Celite to remove succinimide and autopolymerized monomer. The hexanes was removed and a column run on the residual liquid using a 4:1 hexanes to ethyl acetate mixture. After collecting the product, it is treated with a small amount of activated carbon to removal residual radicals and improve the stability of the product. Following treatment, a pale yellow oil is recovered in 80 % yield, which is stored protected from light at -20 °C. ^{1}H NMR (300 MHz, $CDCl_3$) δ 6.80 (s, 1H), 4.15 (t, 2H), 3.78 (t, 2H), 3.69 (t, 2H), 3.54 (t, 2H), 3.38 (s, 3H).

3.5.2.3 Synthesis of 2,5-dibromo-3-thiophenemethanol

To a 3-neck flask, THF (36.4 mL) and 3-thiophenemethanol (3.77 mL, 40 mmol) were added, then degassed by bubbling nitrogen through the solution for 15 min. Following degassing, recrystallized NBS (total: 14.15 g, 79.5 mmol) was quickly added to the reaction over 5 equal portions, stirring briefly between each addition. The reaction was allowed to stir overnight at room temperature. The reaction was filtered to remove the precipitated succinimide, and the solvent was removed using rotary evaporation. The residue was purified using column chromatography using a 4:1 hexanes to ethyl acetate eluent, resulting in a white solid in 90% yield. ^{1}H NMR (300 MHz, $CDCl_3$): δ 7.03 (s, 1H), 4.60 (s, 2H), and 1.95 (br, 1H).

3.5.2.4 Synthesis of 2,5-dibromo-3-thiophenemethylbromide

2,5-dibromo-3-thiophenemethanol (9.0 g, 33.5 mmol) and DCM (165 mL) was added to a round bottom flask, then cooled for 20 min on ice. After cooling, PBr_3 (3.20 mL, 34.25 mmol) was added dropwise over 15 min, and the reaction was allowed to stir at room temperature for 5 h. 100 mL of 10% $NaHCO_3$ solution was added to quench the reaction. The product was extracted with DCM, washed with brine, dried with $MgSO_4$, filtered, and the solvent removed. After incubating at -20

°C overnight, the product was collected as a white solid in 93% yield. ^{1}H NMR (300 MHz, $CDCl_3$): δ 7.00 (s, 1H), 4.36 (s, 2H).

3.5.2.5 Synthesis of 2,5-dibromo-3-methoxyethoxyethoxymethylthiophene

To a 3-neck flask equipped with an addition funnel, THF (100 mL) and diethylene glycol monomethyl ether (3.5 mL, 30 mmol) were added. NaH (1.32 g, 33 mmol) was added in one portion, and the flask was quickly recapped. The NaH was allowed to react for 10 min, until H_2 gas evolution had ceased. 2,5-dibromo-3-thiophenemethylbromide was dissolved in 25 mL of THF, then added to the addition funnel. It was then added dropwise over 15 min, after which the reaction was allowed to stir overnight. The product was filtered over Celite to remove precipitated salts, rinsing through with THF to ensure complete product elution. The solvent was removed using rotary evaporation, and the product purified using column chromatography with a 3:2 mixture of hexanes and ethyl acetate, resulting in a pale yellow oil in 87% yield. ^{1}H NMR (300 MHz, $CDCl_3$) δ 7.0 (s, 1H), 4.43 (s, 2H), 3.65 (m, 6H), 3.57 (m, 2H), 3.39 (s, 3H).

3.5.3 Synthesis of Polymers

3.5.3.1 P3MEET

2,5-dibromo-3-methoxyethoxyethoxythiophene (360 mg, 1.0 mmol) was added to a Schlenk flask, then degassed under high-vacuum for 30 min. 10 mL of THF was added, then the flask cooled to 0 °C and *i*-PrMgCl (0.5 mL, 1.0 mmol, 2.0 M) was added dropwise over 10 min. The reaction was allowed to proceed for 1 h at room temperature. The flask was then heated to 45 °C, and Ni(dppp)Cl_2 (4.336 mg, 0.008 mmol) was added in one portion, and the polymerization was allowed to continue for 2 h at 45 °C. To quench the polymerization, HCl (1 mL, 5.0 M) was added to the reaction, and the polymer was precipitated into 400 mL of MeOH. The polymer was purified using successive Soxhlet extractions using hexanes, MeOH, and then collected with $CHCl_3$. The polymer was again precipitated into MeOH, then filtered to be collected as a powder, and dried overnight in a vacuum oven. ^{1}H NMR (500 MHz, $CDCl_3$) δ 6.90 (s, 1H), 4.27 (s, 2H), 3.82 (s, 2H), 3.70 (s, 2H), 3.50 (s, 2H), 3.27 (s, 3H). *Đ* = 1.40, M_n = 9.2 kg/mol.

3.5.3.2 P3MEEMT

Following the same procedure outline for P3MEET, 2,5-dibromo-3-methoxyethoxyethoxymethylthiopene (374 mg, 1.0 mmol) was polymerized using *i*-PrMgCl (0.5 mL, 1.0 mmol, 2.0 M) and Ni(dppp)Cl_2 (4.71 mg, 0.0087 mmol). 4.67 (s, 2H), 3.75 (s, 4H), 3.67 (m, 2H), 3.57 (m, 2H), 3.37 (s, 3H). *Đ* = 1.46, M_n = 11.2 kg/mol.

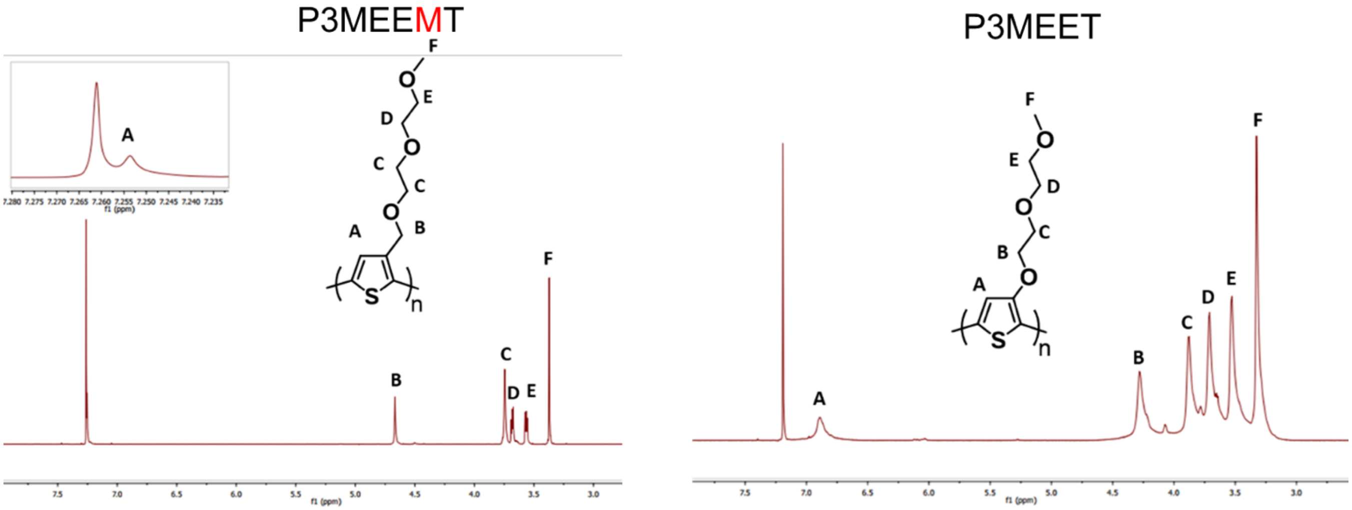

Figure S3.1: ^{1}H NMR of P3MEEMT and P3MEET with polymer backbone peak labels. The inset shows the aromatic proton, labelled "A", which overlaps with the residual $CHCl_3$ peak.

3.5.4 Differential Scanning Calorimetry (DSC)

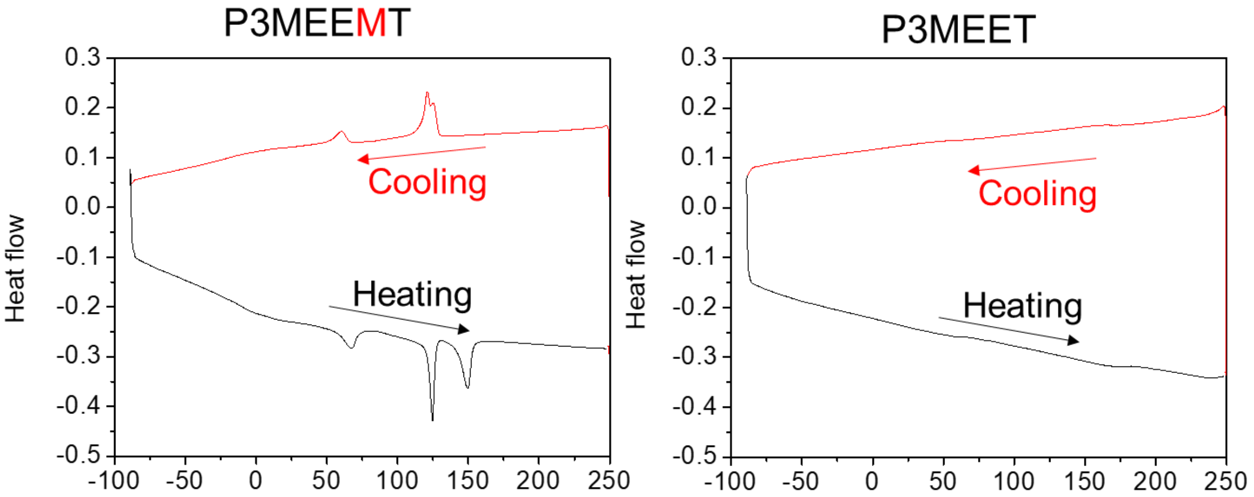

Figure S3.2: DSC scanning curves of P3MEEMT and P3MEET during the heating and cooling cycles. Scanning speed was 5 °C/min.

3.5.5 UV-vis Absorption Spectroscopy

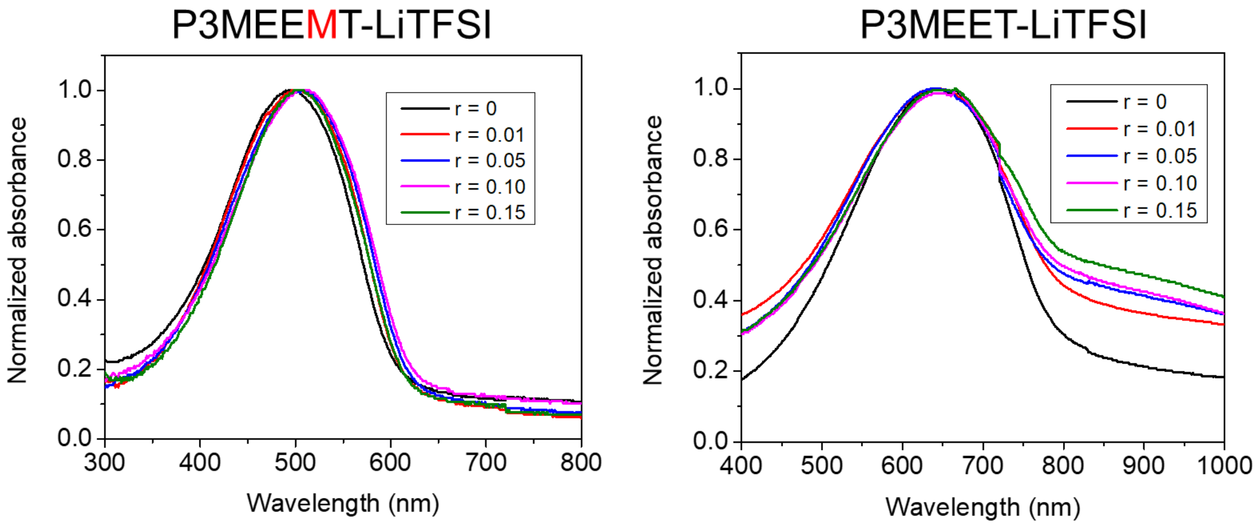

Figure S3.3: UV-vis absorption spectroscopy of P3MEEMT and P3MEET at different LiTFSI blending concentration.

3.5.6 Atomic Force Microscopy

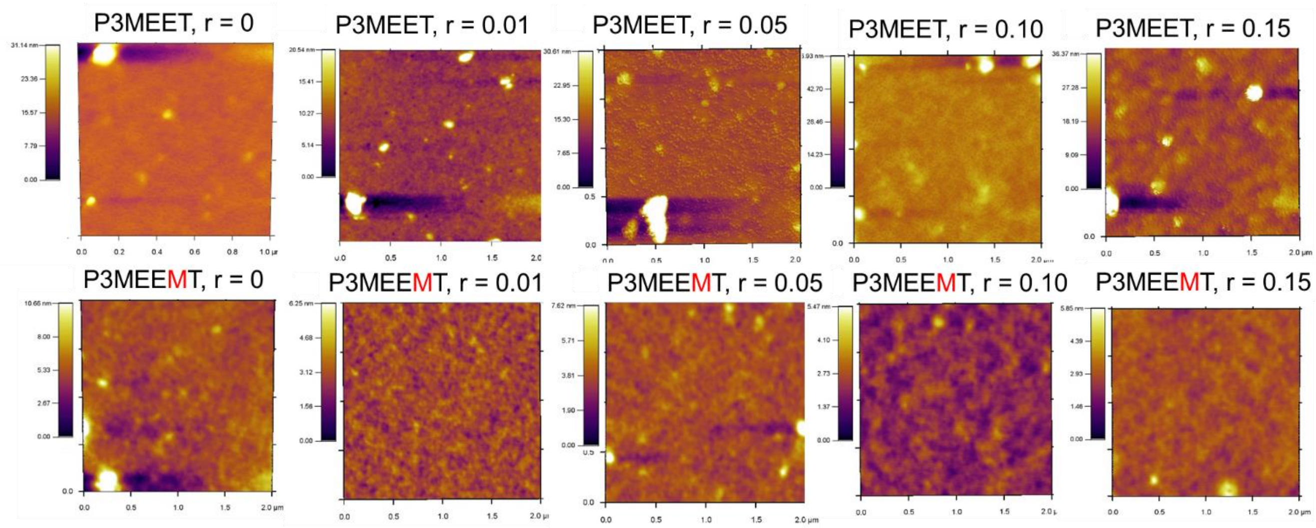

Figure S3.4: AFM images of P3MEEMT and P3MEET at different LiTFSI blending concentration.

3.5.7 Size Exclusion Chromatography (SEC)

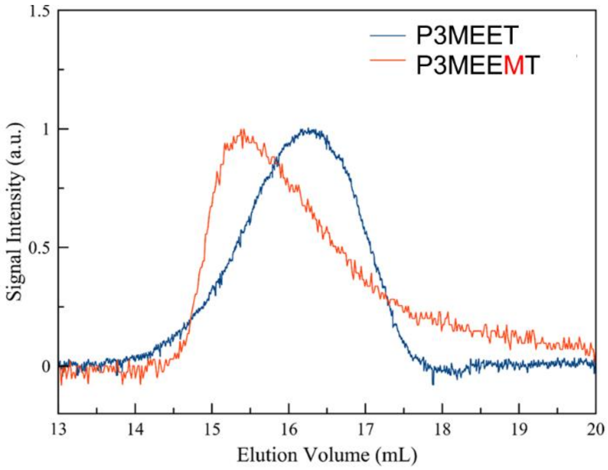

Figure S3.5: SEC elution traces for P3MEET and P3MEEMT.

Size Exclusion Chromatography (SEC) was performed using a Malvern Viscotek TDA 305 GPC with a UV detector. Chloroform was used as an eluent at a flow rate of 1.0 mL/min, and the detector temperature was set to 30 °C. Molecular weight data was determined relative to polystyrene standards. P3MEEMT shows a number average molecular weight, M_n, of 11.2 kg/mol, and a dispersity, $Đ$, of 1.46. For P3MEET, M_n = 9.2 kg/mol and $Đ$ = 1.40.

3.5.8 Additional Molecular Model Information

For atomistic simulations, we use the all-atom (AA) force field potential developed by Cheung, *et. al* (based on the OPLS-AA forcefield[4]) to simulate the thiophene rings. Leveraging its similarity to the OPLS-AA model, we use the OPLS-UA forcefield[4] to model the side chains to decrease computational load. A depiction of our model is given in Figure S3.6. The non-bonded interactions are defined by a combination of Lennard-Jones (LJ) and Coulombic potential energy functions truncated at a cut-off of 10 Å. The parameters for homonuclear non-bonded interactions are given in Table S3.1. We adopted the OPLS-AA forcefield prescription for the mixing rules for heteronuclear non-bonded interactions and scaling of non-bonded interaction for bonded atoms. Parameters for the bond and angle potentials are given in Table S3.2, and S3.3, respectively. For dihedral angle potentials, we used the standard OPLS potential adopted by the Cheung model with the parameters listed in Table S3.4. For the ring-ring and ring-side chain dihedrals we adopted the model and parameters of Poelking and Andrienko[5] given in Table S3.5. To account for the change in partial charges due to the change in chemistry, we altered the charges of the thiophene atoms and the first atom bonded to the ring to maintain charge neutrality and respect the relative values of Muliken charges calculated using BLYP 6-31G*. The remaining atoms in the side chains are assigned charges according to the OPLS-UA forcefield. Figure S3.6 displays all the atomic charges whose values are assumed fixed (i.e., polarization effects are neglected based on the values of their dipole moments[6,7]).

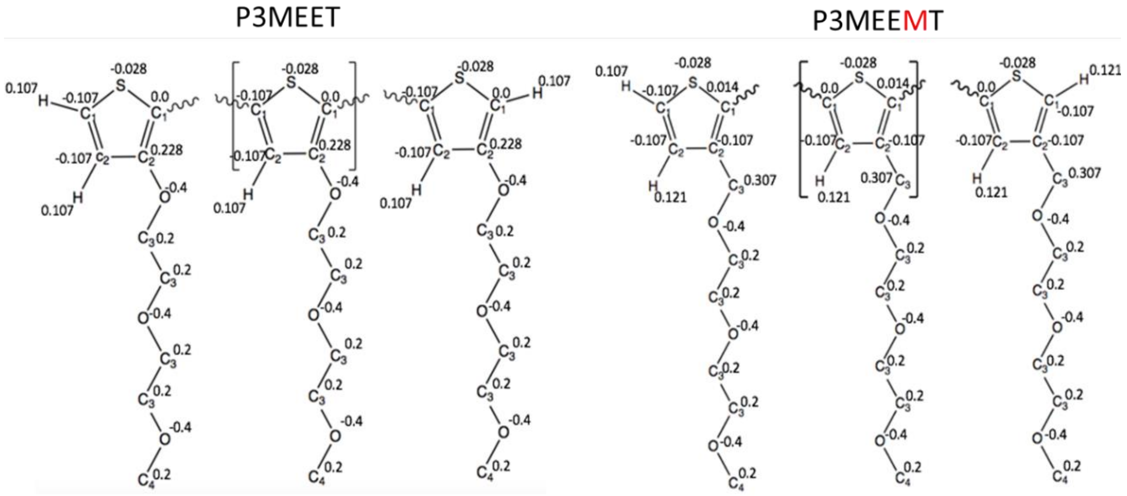

Figure S3.6: Depiction of the end, and inner monomers of P3MEET and P3MEEMT. Charges of the atoms are given.

Table S3.1: Non-bonded parameters used in the AA model. The atom types are defined in Fig S3.6.

Atom type	ε / (Kcal/mol)	σ / Å
C_1[a]	0.07	3.55
C_2[a]	0.07	3.55
C_3[b]	0.118	3.8
C_4[b]	0.17	3.8
H[a]	0.03	2.5
O[b]	0.17	3.0
S[a]	0.25	3.55

[a] Adapted from Ref. [196]
[b] Adapted from Ref. [197]

Table S3.2 Harmonic bond parameters, where the potential is defined by harmonic potential; $U_{bond} = k_b(r - r_0)^2$

Type	k_b / (Kcal / (mol·Å^2))	r_0 / Å
C_1-C_2[a]	514.27	1.364
C_2-C_2[a]	453.1	1.428

C_1-C_1[a]	392.29	1.43
S-C_1[a]	291.25	1.732
C_1-H[a]	370.63	1.08
C_2-H[a]	370.63	1.08
C_2-C_3[b]	317.	1.51
C_2-O[b]	450.0	1.364
C_3-C_3[b]	260.0	1.526
C_3-O[b]	320.0	1.425
O-C_4[b]	320.0	1.425

[a]Adapted from Ref. [198]
[b]Adapted from Ref. [199]

Table S3.3 Harmonic angle parameters, where the potential is defined by harmonic potential; $U_{angle} = k_{\theta}(\theta - \theta_0)^2$

Type	k_θ / (Kcal / (mol·radian^2))	θ_0 / degree
C_1-S-C_1	86.36	92.774
S-C_1-C_2	86.36	110.292
C_1-C_2-C_2	39.582	113.322
S-C_1-C_1	41.74	119.569
C_1-C_1-C_2	35.263	130.14
S-C_1-H	28.787	124.609
C_2-C_1-H	35.263	125.1
C_1-C_2-H	35.263	122.979
C_2-C_2-H	35.263	123.7
C_2-C_2-C_3	70.0	123.7

C_1-C_2-C_3	70.0	122.98
C_2-C_2-O	70.0	123.7
C_1-C_2-O	70.0	122.979
C_2-C_3-O	50.0	109.5
C_2-O-C_3	75.0	111.0
C_3-O-C_3	100.0	111.8
O-C_3-C_3	80.0	109.5
C_3-O-C_4	100.0	111.8

[a]Adapted from Ref. [196]
[b]Adapted from Ref. [197]

Table S3.4: OPLS torsional parameters, where the potential is defined as; $U_{dihedral} = \sum_{n=1}^{4} \frac{1}{2} V_n [1 + (-1)^{n+1} \cos n\phi]$

Type	$V_1 \left(\frac{1\text{Kcal}}{\text{mol}}\right)$	$V_2 \left(\frac{\text{Kcal}}{\text{mol}}\right)$	$V_3 \left(\frac{\text{Kcal}}{\text{mol}}\right)$	$V_4 \left(\frac{\text{Kcal}}{\text{mol}}\right)$
C_1-S-C_1-C_2[a]	0	9.51	0	0
S-C_1-C_2-C_2[a]	0	9.51	0	0
C_1-C_2-C_2-C_1[a]	0	9.51	0	0
C_2-C_3-O-C_3[b]	0.65	-0.25	0.67	0
C_3-O-C_3-C_3[b]	0.65	-0.25	0.67	0
O-C_3-C_3-O[b]	-.55	0	0	0
C_3-C_3-O-C_4[b]	0.65	-.25	0.67	0
C_2-O-C_3-C_3[b]	0.65	-.25	0.67	0

[a]Adapted from Ref. [198]
[b]Adapted from Ref. [199]

Table S3.5 Multi-Harmonic torsional parameters, where the potential is defined by harmonic potential; $U_{dihedral} = \sum_{n=1}^{6} V_n cos^{n-1}\phi$

Type	$V_1\left(\frac{\text{Kcal}}{\text{mol}}\right)$	$V_2\left(\frac{\text{Kcal}}{\text{mol}}\right)$	$V_3\left(\frac{\text{Kcal}}{\text{mol}}\right)$	$V_4\left(\frac{\text{Kcal}}{\text{mol}}\right)$	$V_5\left(\frac{\text{Kcal}}{\text{mol}}\right)$	$V_6\left(\frac{\text{Kcal}}{\text{mol}}\right)$
S-C_1-C_1-S^c	5.2132	-0.0502	-3.4139	0.1124	-1.5909	0.1268
C_1-C_2-C_3-O^c	0.1866	-0.9069	0.0550	1.2440	-0.0359	0.2321
C_1-C_2-O-C_3^c	0.1866	-0.9069	0.0550	1.2440	-0.0359	0.2321

[c]Adapted from Ref. [183]

3.5.8.1 Calculation of Ionic Mobility

The ion mobility from equilibrium MD simulations can be found from the diffusion constant based on the Einstein mobility relation, $\mu = Dq/kT$. Here, μ is the charge mobility, q is the charge, k is the Boltzmann constant, T is the temperature, and D is the diffusion constant calculated through the mean-square displacement (MSD) using

$$D = \frac{1}{6} \lim_{t\to\infty} \frac{\delta}{\delta t} \langle X_0^2(t) \rangle \qquad \text{Equation S3.1}$$

However, this relationship is not valid in the presence of an external electric field as it will induce a directional drift of the ions. Hence, in the presence of a uniform (and unidirectional) electric field the total displacement is given by

$$\langle X_E^2(t) - X_0^2(t) \rangle = (vt)^2 \qquad \text{Equation S3.2}$$

Where v is the drift velocity in the direction of the applied field. The ionic mobility can be calculated from:

$$\mu = \frac{vt}{E} \qquad \text{Equation S3.3}$$

where E is the applied electric field. We hence used the above equation as the basis for our mobility calculations. Since the calculated self-diffusion of Li^+ ions in the system with no applied field is insignificant (~10^{-8}cm^2/s) compared to the calculated drift velocities, the expression for calculating the drift velocity then reduces to:

$$\langle X_E^2(t)\rangle = (vt)^2 \qquad \text{Equation S3.4}$$

which simplifies the calculation. Fig. S3.7 shows how the MSD of each ion is fitted to Equation S3.4. Ions showing a good fit to that expression are considered "mobile", i.e., moving in a way that can be described as under the influence of an electric field. For each mobile ion the fit is used to extract v and the average mobility is calculated from those values. Using MSD for calculating μ, and $\hat{\sigma}$ is based on convenience where the data for ion positions is easier to handle than using Green-Kubo relations. Previous studies which look at ionic conductivity use both methods.[6,7]

Ions that do not fit the form of Equation S3.4 indicate that they have likely encountered a kinetic trap and hence are no longer experiencing continuous drift. In principle, the effect of those trapping events on the average ion mobility could be accounted for (and modelled) if simulations could span long enough periods to collect suitable statistics of trapping-untrapping ("hopping") events. Since that is not the case, we leverage the fact that such events are rare to assume that a hopping mechanism has a small (slowing down) effect in our estimated mobilities. Additionally, if a curve is fit to all ions and the value of conductivity is calculated, the variance between replicas is increased compared to the variance of conductivity values calculated when omitting ions which do not fit the curve well. Thus, we use the omission method to reduce variability in the data.

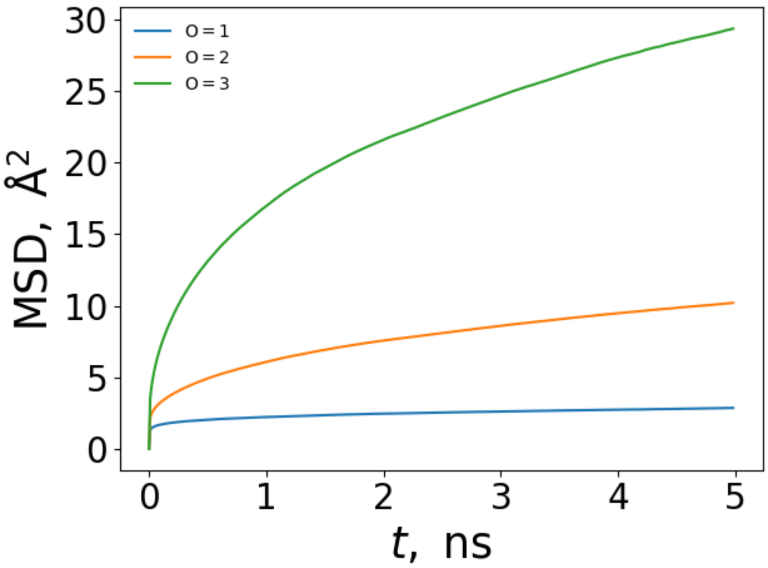

Figure S3.7: Average MSD plots for side chain oxygens in amorphous P3MEEMT (1 is closest to backbone, 3 is furthest from backbone).

3.5.8.2 Quantifying mobility of side chain oxygens

The data from Figure 3.1d is derived from the average plateau value of MSD for the each of the three oxygens in the side chains of P3MEET and P3MEEMT. Figures S3.7, S3.8, S3.9, and S3.10, show the average MSD vs. time plots for amorphous P3MEET, amorphous P3MEEMT, crystalline P3MEET, and crystalline P3MEEMT, respectively. These plots are used to derive the plateau values (reached at long times).

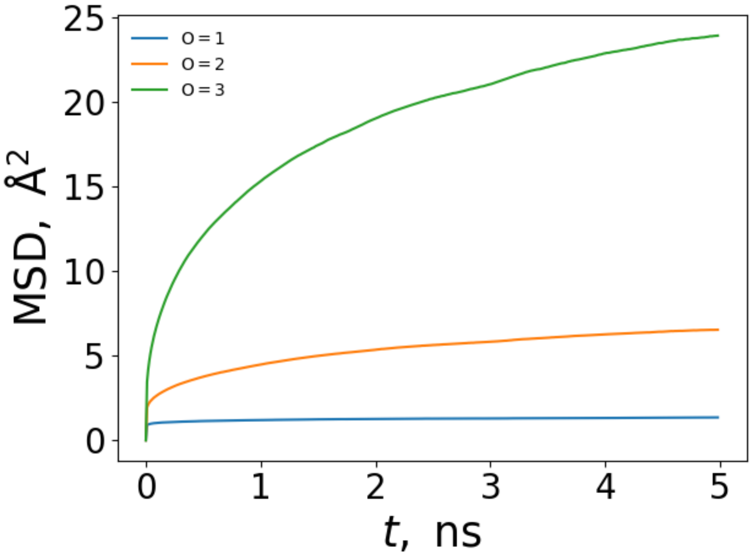

Figure S3.8: Average MSD plots for side chain oxygens in amorphous P3MEET (1 is closest to backbone, 3 is furthest from backbone).

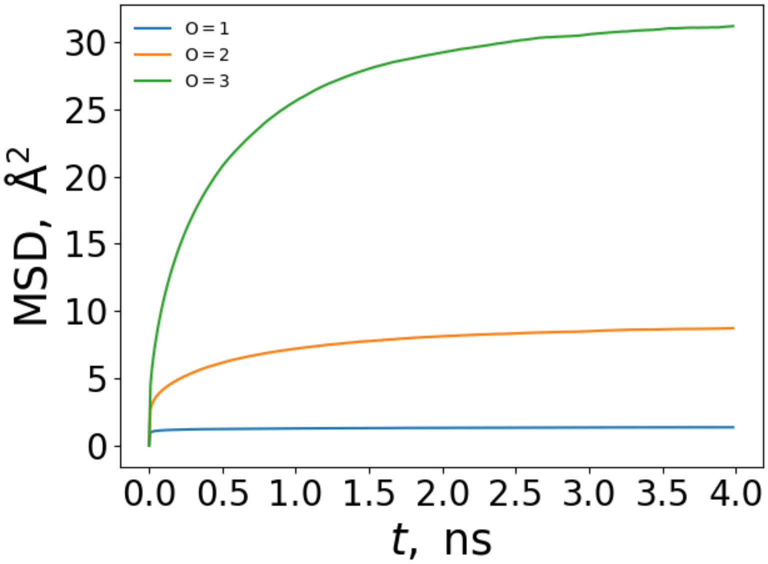

Figure S3.9: Average MSD plots for side chain oxygens in crystalline P3MEEMT (1 is closest to backbone, 3 is furthest from backbone).

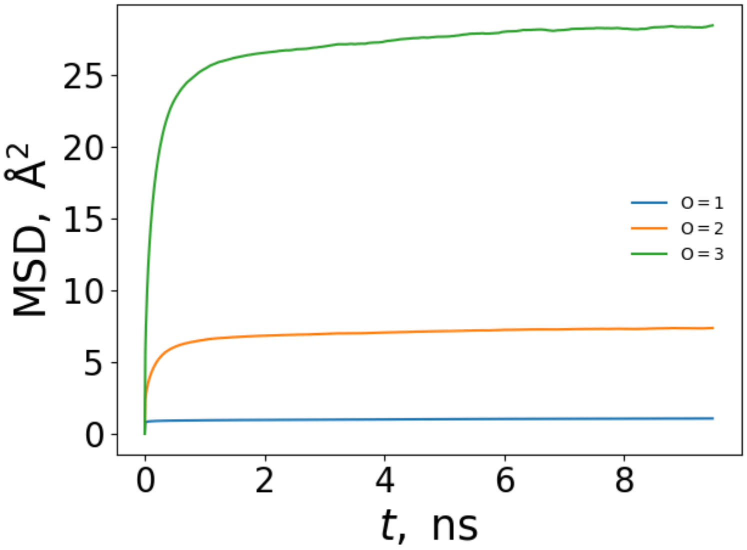

Figure S3.10: Average MSD plots for side chain oxygens in crystalline P3MEET (1 is closest to backbone, 3 is furthest from backbone).

3.5.9 Nyquist Plot at Low Frequencies

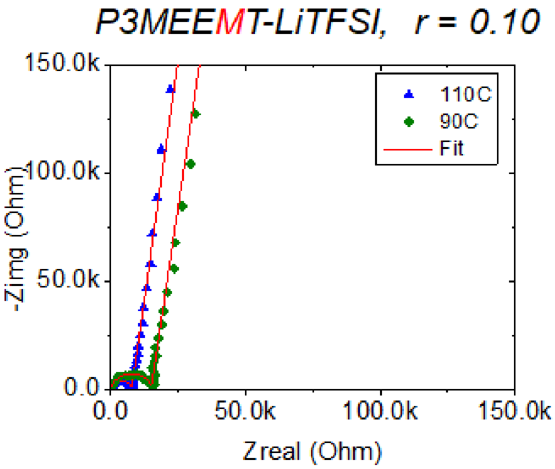

Figure S3.11: Nyquist plot of P3MEEMT-LiTFSI, r = 0.10 showing straight line behavior at low frequencies.

Ch. 4: Variation of Side Chain Composition on Ionic Conduction in Mixed Ionic/Electronic Conducting Polymers

Statement on Distribution of Work: The work described herein was a combination of the efforts of myself and Christian Nowak, who contributed the molecular dynamics simulations described in Section 4.3.1. The analysis of the implications and writeup for that section were my own work. All else presented in this chapter represents my own work.

Abstract:

With this work, we investigate how variations in both the oxygen content, as well as the oxygen atom placement along the side chain, influence the morphology and ionic conductivity of a series of oligoethylene glycol-substituted polythiophenes. While recent work has recently been done exploring changing substitution patterns or attachment variations for these oligoethylene glycol-substituted polymers, no studies into the effects of modifying the oligoethylene glycol chain have yet been performed. We first explored a permutation set of oxygen content and positioning through the use of molecular dynamics in a 9-atom-length side chain, finding an overall trend that with changing oxygen content we see a trade-off between ion concentration and ion mobility. A subset of those polymers was chosen for synthesis. The neat polymers were first analyzed, to investigate baseline morphology for these polymers. Based on UV-Vis spectroscopy, it was determined that introducing oxygen atoms too close to the polymer backbone, as in P3PAAT, significantly hinders planarization of the polymer backbone. We also see significant variation in the (100) d-spacing, with P3AAPT and P3PAAT being quite similar with 2.10 nm and 2.07 nm respectively, and P3APPT being slightly smaller, at 1.98 nm. The interactions between the polymers and LiTFSI, and the overall effect on the morphology was then investigated. We saw a decrease in LiTFSI solubility for these polymers as compared to P3MEEMT, but we also saw that introduction of LiTFSI results in significant backbone planarization of both P3AAPT and P3APPT. From XRD,

P3APPT's crystal structure showed a higher uptake of LiTFSI, swelling up to 13.8% at r = 0.15, whereas P3AAPT reached 11.7%, and P3PAAT only 3.4%. These results demonstrate the sensitivity that these MIEC systems have to variations in side chain architecture and highlight the need for careful consideration of not only side chain placement, but also chemical structure, in producing high-performing MIEC materials.

4.1 Introduction

Polymer-based mixed ionic/electronic conductors (MIECs) have recently begun receiving increased attention, due in part to their utility across a wide-range of applications. As the name suggests, MIECs are polymers that can conduct both ions and electrons. These materials show interesting properties, including volumetric transconductance changes, transduction of ionic and electronic signals, and biocompatibility.[69,200–203] These properties result in a number of useful features, enabling their use in things like batteries and ultracapacitors, (bio)sensors, actuators, and organic electrochemical transistors (OECTs).[204–206]

MIECs as a category are quite broad, as there are many strategies to bring together both ionically conductive electronically conductive components into a single material. The most common methodology is to blend two polymers; one polymer provides electronic conduction, while the other provides ionic conduction.[71,207] A prime example of this class of materials is poly(ethylenedioxythiophene):poly(styrenesulfonate) [PEDOT:PSS], which has long been one of the preeminent MIECs.[8,81,88,98] Another strategy involves block copolymers, with one block providing ionic conduction, and the other providing electronic conduction.[15,16,205] Both of these strategies result in MIECs with performance that is difficult to optimize.[52,71] This difficulty stems from complicated phase behavior that is often complex, and thus challenging to characterize, making determining and eventually predicting what morphological structures are beneficial for performance.[60,80,84] A further problem with this space lies in the apparent compromise between ionic conduction and electronic conduction; improving one tends to reduce the other.[52] Due to this, attention has recently shifted to developing novel MIEC homopolymers.[70,208,209] Typically, this relies on modifying the side chains of commonly-used electronically conducting polymers, introducing polar groups to enable ion coordination. Pure homopolymer systems are more tractable, as they have less complicated phase behavior.

Initial efforts in producing homopolymer MIECs focused on systems such as polyaniline and polyacetylene.[131,139] These early systems suffered from poor ionic conductivity due to their high hydrophobicity, and thus low ability to dissolve ionic salt. Modifying side chain structures has resulted in significant improvements for electronic motion in conjugated polymer systems. Similarly, recent efforts to introduce and improve ion conduction in homopolymer MIECs focused on introducing ion-coordinating groups into side chains.[9,168] It was shown that using oligoethylene glycol side chains to a polythiophene-based backbone enables bulk transport of ions.[69] This strategy of introducing oligoethylene glycol has seen great success and wide application across a number of conjugated polymer backbones.[69,70,141,210]

Side chains are known to have a significant influence on the morphology of conjugated polymers. Side chains have a two-fold effect for MIECs, as they not only influence morphology and thus electronic conductivity, but also because their side chains contain ion-conducting groups the structure of which significantly impacts ionic conductivity. For example, by varying the ratio of oligoethylene glycol and alkyl side chains in a polymer, the structure of which is shown in Figure 4.1A, the polymer can fully switch from volumetric to interfacial doping (*ie*, from an MIEC to just an electronic conductor).[210] Beyond just the ion-coordinating atoms present and length of the side chain, the manner of attachment of these side chains makes a significant difference in MIEC performance. Previous work from our group shows that even relatively small changes like adding a methylene bridge between the oligoethylene glycol side chain and thiophene backbone (going from P3MEET to P3MEEMT, Figure 4.1B) can result in an order of magnitude increase in ionic conductivity, and significant variations in crystallinity on LiTFSI introduction.[141] Recent work has extended this further, demonstrating an increase in both ionic conductivity and crystallinity by adding an ethylene bridge instead of a methylene, as shown in Figure 4.1, B.[211]

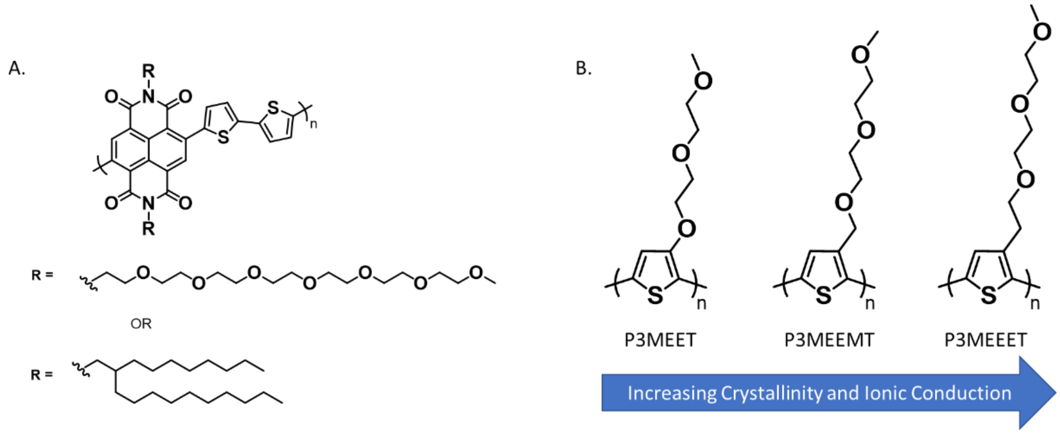

Figure 4.1: A: A recent random copolymer synthesized with a changing ratio of oligoethylene glycol side chains and purely alkyl side chains. B: Increasing the number of carbon atom spacers between a diethylene glycol side chain and the polymer backbone increases ionic conductivity and polymer crystallinity.

It’s clear that there is significant variation in the performance of MIEC systems based on the manner of attachment of these oligoethylene glycol side chains, but it’s currently not understood how modifying the oligoethylene glycol side chain itself influences the resultant ionic conduction. To that end, herein we investigate a series of polymers with reduced oxygen content as compared to the typical diethylene glycol chain, seeking to understand the influence of oxygen content and position on the polymer morphology, as well as its ionic conductivity. We first explored 6 permutations of a substituted polythiophene with a 9-atom side chain using molecular dynamics, simulating both crystalline and amorphous phases, and determined the ionic conductivity of each polymer for both phases. Based on those results, we synthesized a subset of those polymers, and characterized their solid-state structure across a range of LiTFSI concentrations. By studying this range of polymers across a range of LiTFSI doping concentrations, we are able to elucidate how variations in the side chain architecture influence the evolution of morphology with increasing levels of LiTFSI doping, highlighting the importance of the architecture of oligoethylene glycol side chains in determining the doped material's morphology.

4.2 Experimental

4.2.1 Synthesis

The detailed monomer and polymer synthesis and characterization are described in the Supplemental Information.

4.2.2 Substrate Preparation

Substrates were prepared by cutting to 1.5 cm × 1.5 cm, then cleaning by mechanically scrubbing with Merisuds soap, then rinsing with DI water. The substrates were then sonicated in first DI water, then acetone, then IPA. Finally, the substrates were plasma cleaned for 10 minutes with air-plasma, after which they were immediately used for film-preparation.

4.2.3 Blended Sample Preparation

Mixtures of polymers with LiTFSI was done through a solution blending process. Each polymer sample was prepared at a concentration of 10 mg/mL in $CHCl_3$ and stirred overnight under nitrogen. These solutions were filtered with a 0.45 µm syringe filter prior to further use. Solutions of LiTFSI were also prepared at a concentration of 10 mg/mL by overnight stirring, but were prepared in acetonitrile (ACN). Blended samples were prepared at a range of concentrations normalized against the number of ethylene oxide (EO) units in each polymer side chains, targeting concentrations of $r = [Li^+]/[EO] = 0$ (neat polymer), 0.01, 0.05, 0.10, 0.15. These blends were prepared by taking the filtered polymer solutions and adding LiTFSI/ACN solution to achieve the desired ratio. Following addition, the solutions were allowed to stir for several hours prior to use, to ensure equilibrium mixing.

4.2.4 ^{1}H NMR

NMR spectra for small molecules was taken using a 300 MHz Bruker AV-300 spectrometer, and spectra for polymers was taken using a 500 MHz Bruker AV-500 spectrometer. All spectra were taken in $CDCl_3$ at room temperature.

4.2.5 Size Exclusion Chromatography (SEC)

SEC was performed using a Malvern Viscotek TDA 305 with an attached UV detector using polystyrene molecular weight references. THF at a temperature of 40 °C at a flow rate of 1 mL/min was used as an eluent.

4.2.6 UV-Vis Spectroscopy

UV-Vis spectra were taken using a Perkin Elmer Lambda 950 UV-Vis-NIR spectrometer. Samples were prepared as thin films on cleaned glass substrates (see Section 4.2.2). The neat polymer thin film samples were prepared by spin coating from chloroform at a concentration of 10 mg/mL, at a volume of 120 µL per substrate and a spin speed of 2,000 RPM for 1 min. The samples were not annealed following spin coating. Optical band-gaps were calculated using the axis-intercept method, drawing collinear lines and determining their 0-value intercept.

4.2.7 Atomic Force Microscopy (AFM)

AFM was performed using a Bruker Dimension Icon, in quantitative nanomechanical mapping mode using ScanAssyst tips. Scans were performed with dimensions of 2 µm unless otherwise noted. Samples were prepared on cleaned silicon substrates with a thermal SiO_2 layer (300 nm)

(Section 4.2.2) by spin coating a 10 mg/mL solution of the desired polymer at a 2000 RPM for 1 min. All data was processed through Gwyddion.[212]

4.2.8 Thermogravimetric Analysis (TGA)

TGA was performed using a TA Instruments Q50 with a heating rate of 10 °C/min.

4.2.9 Differential Scanning Calorimetry (DSC)

DSC was performed using a Mettler Toledo DSC 3+ with aluminum pans. Samples were taken through a heat/cool/heat cycle, with the cooling and second heating cycles being presented herein. Samples were heated and cooled at a rate of 10 °C/min across a window selected based on degradation temperatures determined from TGA (-90 – 225 °C).

4.2.10 X-Ray Diffraction (XRD)

XRD was performed using a Bruker D8 Discover with a Cu anode x-ray source. The system is combined with a Pilatus 100K large-area 2D detector, and was equipped with a 0.5 mm beam collimator. The incident angle was fixed at 0.5 degrees. All samples were imaged using the same exposure time.

Samples were prepared on cut Si wafers that were cleaned as described in Section 4.2.2. Samples were prepared as described in Section 4.2.3 and drop-cast onto the Si substrates at room temperature and allowed to evaporate.

4.3 Results and Discussion

4.3.1 Molecular Dynamics Investigations

A significant problem in exploring novel material chemistries is the time-intensive nature of polymer synthesis. As such, to explore the performance across the full spread of possible side chain oxygen permutations, we first turned to simulations. The full range of polymers investigated are shown in Figure 4.2.

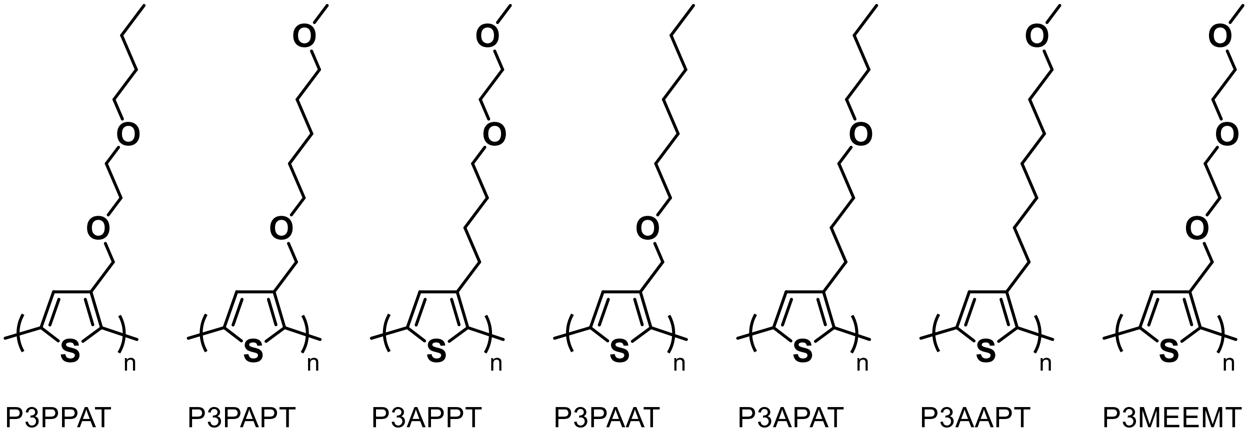

Figure 4.2: Full list of possible oligoethylene glycol permutations with a 9 atom-length side chains.

Two distinct morphologies were targeted for each polymer investigated, crystalline and amorphous. The procedure for generating both systems are described briefly here and are described in greater detail in Chapter 3. For generating crystalline structures, the crystal structure for poly(3-hexylthiophene) [P3HT] was used as a template, expanded to accommodate the slightly larger polymer side chain. Atoms were arranged to match the typical structure of P3HT's polymorph I, then allowed to equilibrate at 300 K. Amorphous structures were generated by taking a P3HT system, expanding it to accommodate the larger polymer side chain, and then raising the temperature of the system to 600 K to allow the system to become disorganized (*ie* effectively melting the crystals). The temperature was then immediately quenched to 300 K, to lock-in the predominantly amorphous morphology. This resulted in a significantly more disordered structure, though some stacking behavior was still observed.

After generating each structure, the conductivity of each polymer system for Li^+ ions in both structures was calculated using molecular dynamics. In this section, because we are exploring polymeric systems with variations in oxygen concentration and positions, we needed a method to measure the relative concentration of dissociated ions in each system to account for differences in the ability of a polymer structure to dissolve ions. To do this, we calculated an energy of dissociation for LiCl salt in each polymer environment, and used it to normalize the measured conductivity values, as shown in Equation 4.1, where σ is the normalized conductivity, q is the ion valence (1 in this case), v is the drift velocity, n is the number density of dissociated ions, and E_d is the dissociation energy:

$$\sigma = \frac{qvn}{E_d} \qquad \text{Equation 4.1}$$

The process by which E_d is calculated is described in greater detail in the SI. The resultant σ for these calculations is shown in Figure 4.3. An overall trend observed is that with increasing oxygen content, we see a reduction in the mobility of the ions (due to increases in attraction between ions and side chain oxygens), but we also see a concomitant decrease in the E_d, resulting in relatively balanced effects.

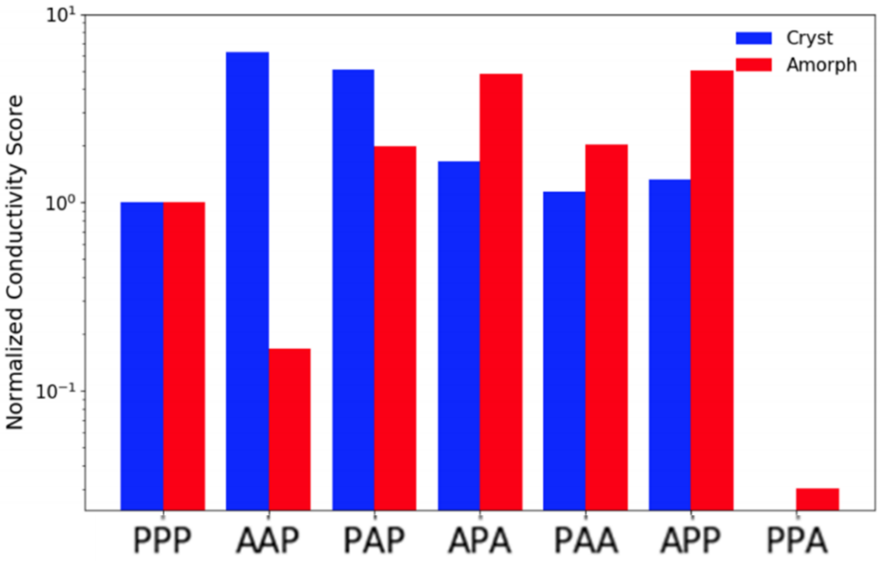

Figure 4.3: Calculated normalized conductivity of all P3MEEMT derivatives.

Looking at the progression of crystalline conductivities for AAP, APA, and PAA, we can see that the conductivity decreases as the oxygen atom is moved closer to the thiophene backbone. This represents a continuation of our previously observed trend (Ch. 3) where, as the oxygen atom is moved farther out along the side chain, we see an increase in the observed mobility of ions.

An illustrative case of ion solvation issues is highlighted well by the observed differences between the crystalline and amorphous structures of AAP. Due to the lone oxygen atom's position at the end of the long side chain, the oxygen atom has a high range-of-motion, which, as shown in the previous chapter, results in an increased ion mobility. The structural differences that lead to changes in performance are attributed to the organization of the oxygen atoms in the solid. When the oxygen atoms are highly ordered and regularly spaced (*ie*, have a high density), as is the case in the crystalline domain, the ion solubility is not significantly reduced, resulting in a high-performance material. However, when the oxygen atoms are disordered and irregularly spaced, as in the amorphous material, we see that the E_d increases significantly, as does the average hopping distance required for each Li^+ atom, and so the overall performance plummets. This issue is further illustrated by considering the performance of the APP structure. Though the crystalline conductivity is significantly reduced by comparison to the AAP, it's notable that the APP amorphous conductivity is significantly improved, almost matching the crystalline conductivity of the AAP. This shows the significance of the number of coordinating oxygen atoms on the ionic conductivity.

There are two outlier cases to note. The PPA system is quite surprising in how poorly it performs, but it highlights the extreme sensitivity of side chain engineering on ionic conductivity. It performs so poorly as it draws all of the ionic density in towards the polymer backbone, limiting the ease of hoping events between adjacent side chains. The simulated performance of the PAA system is surprising, but in the opposite direction. Previous publications looking into alkoxy-substituted chains of similar structure (*ie*, an oxygen directly attached to the backbone, with the remainder of the side chain being alkyl), have shown no mixed-conduction performance. It remains to be seen if this change is due to the shorter nature of our alkyl chain than these literature examples or represents an opportunity for improving the accuracy of our models.

Because of the observed performances and trends, the AAP, PAA, and APP systems were selected for further experimental characterization.

4.3.2 Polymer Synthesis

P3AAPT, P3PAAT, and P3APPT are synthesized following a Kumada Catalyst Transfer Polymerization (KCTP) mechanism from their respective dibrominated monomers. The specific details of the monomer and polymer syntheses are described in the SI. The polymer molecular weights are shown in Table 4.1.

*Table 4.1: Polymer molecular weight for all polymer samples. * P3MEEMT molecular weight shown for reference.*

	P3AAPT	P3APPT	P3PAAT	P3MEEMT*
M_n (kg/mol)	12.4	10.5	9.1	11.2
Đ	1.38	1.51	1.91	1.46

4.3.3 Neat Polymer Analysis

Once prepared, the polymers were characterized using UV-Vis spectroscopy, to clarify differences in their solid-state packing behavior, focusing on the influence of both oxygen content and position. The observed spectra are shown in Figure 4.4. Though these films were cast from chloroform and were unannealed, both P3AAPT and P3APPT have very similar spectra, which both possess a high degree of backbone planarization. This is demonstrated by the appearance of a vibronic progression, and the overall basochromic shift in optical band-gap as compared to both

P3PAAT and P3MEEMT, which do not exhibit a vibronic progression.[213,214] This variation is likely due to the presence of the oxygen atom adjacent to the thiophene backbone which hinders the chain's ability to planarize. These observed differences in polymer planarization also remain in the solution state, though to a lesser magnitude, where P3AAPT and P3APPT demonstrate higher wavelength peak maxima as compared to P3PAAT and P3MEEMT (Figure S4.15). It appears as though even in solution the proximal oxygen atom causes a greater amount of backbone twist. The shift between P3MEEMT and P3PAAT absorption peak maxima is approximately 25 nm. This shift combined with the 18 nm shift in solution absorption peaks (Figure S4.15) implies that P3MEEMT has a greater amount of electron density being donated to the polymer backbone from the side chain than P3PAAT. We note also that there is an increase in breadth of the absorption peak of P3MEEMT compared to P3PAAT, which indicates a greater distribution of planarization states. This result highlights that it is not simply the oxygen content that influences planarization and ordering, but rather the positioning and placement of those oxygen atoms.

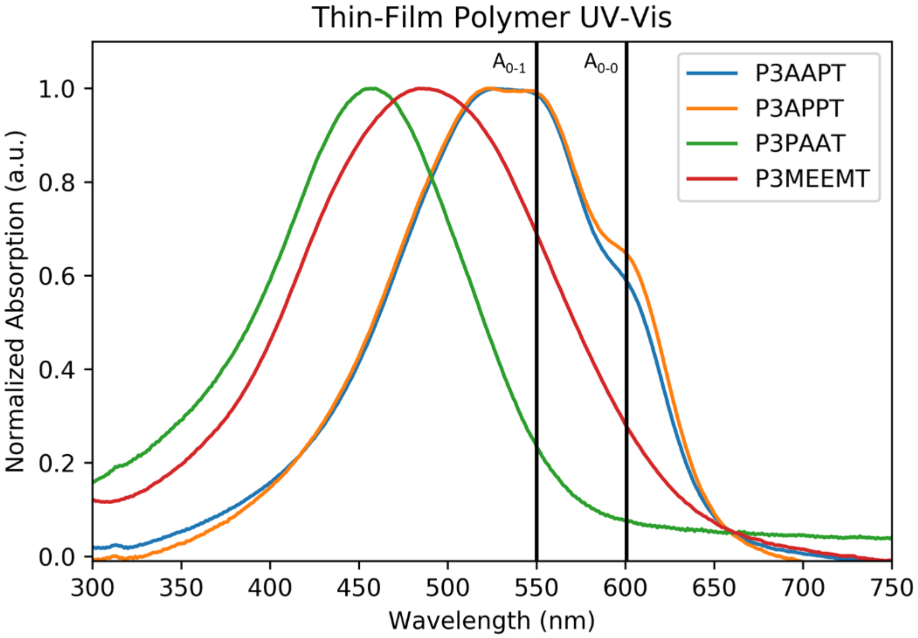

Figure 4.4: Spectra for all polymers, as spin cast from $CHCl_3$ on cleaned glass substrates.

Table 4.2: Calculated optical properties from the UV-vis spectra of neat polymers.

Polymer	P3AAPT	P3APPT	P3PAAT	P3MEEMT
$E_{g,\ opt}$ (eV)	1.89	1.88	2.18	1.95
Solution Peak Maximum (nm)	448	447	422	440
Thin-Film Peak Maximum (nm)	526	525	459	484

Drop cast polymer films were used for diffraction studies, to probe the structure of crystallites within the neat polymers, the results of which are shown in Figure 4.5, left. There are notable qualitative differences between the samples; P3AAPT and P3APPT show strong relative (200) and (300) peaks, whereas P3PAAT's (200) is faint, and (300) is not determinable. The peak positions are also quite different, with 2θ values increasing from P3AAPT to P3PAAT to P3APPT, as highlighted in Figure 4.5, right. This varying peak position corresponds to a variation in (100) d-spacing which also follows the same order of P3AAPT (2.10 nm), P3PAAT (2.07 nm), and P3APPT (1.98 nm). All three polymers have a significantly larger (100) d-spacing than P3MEEMT (1.87 nm). In spite of these side chain direction differences, all three polymers display similar (010) d-spacing, with 0.379 nm for P3AAPT and P3PAAT, and 0.378 nm for P3APPT, values which align well with P3MEEMT's 0.380 nm (010) d-spacing.[141]

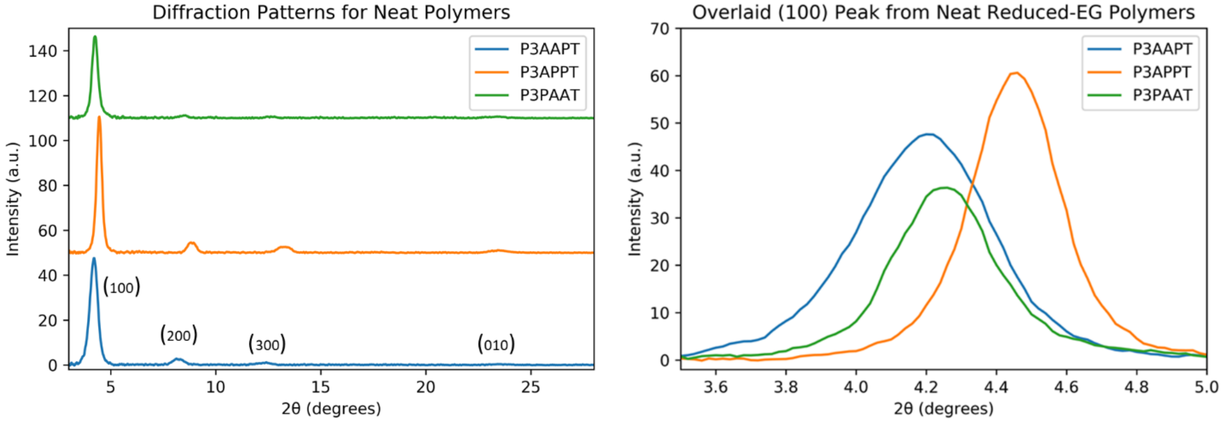

Figure 4.5, Left: XRD diffraction patterns for the neat polymer samples. The observed (100), (200), (300), and (010) planes are labeled. Right: Focused overlay of the (100) peaks from the polymers.

To provide more information on the morphology of these three polymers, and investigate the chemical structure effects on crystal quality, the polymers were investigated through a mix of thermal characterization methods. The polymers all displayed comparable decomposition temperatures to P3MEEMT through thermogravimetric analysis (TGA), as shown in Figure S4.12. The crystalline and amorphous domains of the neat polymers were investigated using differential scanning calorimetry (DSC). The overlaid traces of these polymers are shown in Figure S4.13. The thermal transitions in these samples can be broken apart into two segments, the side chain stacking region, at lower temperatures (0-70 °C in these samples), and the π-stacking region, at higher temperatures (125-175 °C in these samples). The π-stacking region is important to consider, as electronic charge transport depends significantly on hopping events in the π-stacking direction. This region shows marked difference across the samples. P3PAAT shows no discernible melting transition, whereas P3AAPT and P3APPT each have a strong multimodal melting transition. This indicates the P3PAAT has at most very small π-stacking crystallites, whereas both P3AAPT and P3APPT have a higher degree of crystallinity. It's notable that though the melting shape looks similar, the T_m for P3AAPT is ~35 °C higher. Both P3AAPT and P3APPT show similar, unimodal, crystallization peaks on the cooling cycle, again shifted by approximately 35 °C. Overall, we see that oxygen atoms too close to the backbone are hindering π-stacking, and thus crystallization, and that introducing a second oxygen atom in the side chain results in a significant crystal melting point depression. The lack of a π-stacking melt implies that P3PAAT will have poorer electronic conductivity than either P3AAPT or P3APPT, as typically strong π-stacking behavior is needed. Both P3AAPT and P3APPT demonstrate notable π-stacking signals which is promising for electronic charge transport.

Investigating the side chain region is important, as ion transport is occurring exclusively in the side chain region. These traces highlight significant differences between the polymers. P3PAAT does demonstrate a side chain melting peak; however, it occurs at a much higher temperature (75 °C), than either of P3AAPT (35 °C) or P3APPT (10 °C). This will have implications on its ion-conduction potential, as crystalline side chains will not conduct ions as readily as fully melted side chains. It is notable to see that the side chain melt for P3APPT is just below room temperature, and P3AAPT is just above. It is thus reasonable to expect that P3APPT will have significantly higher room temperature ionic conductivity, due to the higher mobility of atoms in its side chain than P3AAPT at room temperature, but that the differences due to side chain crystallinity will be mitigated at temperatures above 50 °C, as the P3AAPT side chain will be fully melted. These values are liable to evolve as LiTFSI is introduced; however, their initial low temperatures are promising indicators for the polymers' low-temperature ionic conductivity. The influence of this observed difference in side chain melting temperature on ionic conductivity could be in part mitigated by the lower concentration of side chain crystals in P3AAPT, as evidenced by the significantly smaller signal intensity of the P3AAPT side chain melt as compared to P3APPT. Though P3PAAT showed no π-stacking melt, the side chain melting peak is comparable in embodied energy to P3AAPT. This data shows that both P3AAPT and P3APPT have similar and significant amounts of crystallinity, whereas P3PAAT has only very minimal crystallinity. There is notable side chain crystallinity for all samples, though P3APPT shows slightly more crystallinity.

4.3.4 Influence of LiTFSI Introduction on Polymer Morphology

After gaining an understanding of the baseline morphology of the polymers with varying oxygen position and content, the influence of LiTFSI on polymer morphology was investigated. In addition to morphological evolution, variations in LiTFSI solubility are of interest, as these changes will have a direct effect on the maximum ionic conductivity achievable for each polymer. LiTFSI was introduced into each polymer samples at a ratio, *r*, as defined by Equation 4.2:

$$r = \frac{Li^{+}\ atoms}{\#\ of\ ethylene\ oxide\ repeat\ units} \qquad \text{Equation 4.2}$$

For example, P3AAPT and P3PAAT would have 1/3 and P3APPT would have 2/3 the content of LiTFSI as P3MEEMT for the same *r* value. *r* values of 0.01, 0.05, 0.10, and 0.15 were investigated. To garner insight into how the introduction of LiTFSI influences the organization of these polymers in the solid-state, UV-Vis spectroscopy was performed on all polymers across a range of *r* values, the spectra of which are shown in Figure 4.6. Samples were prepared by spin coating polymer films on cleaned glass substrates.

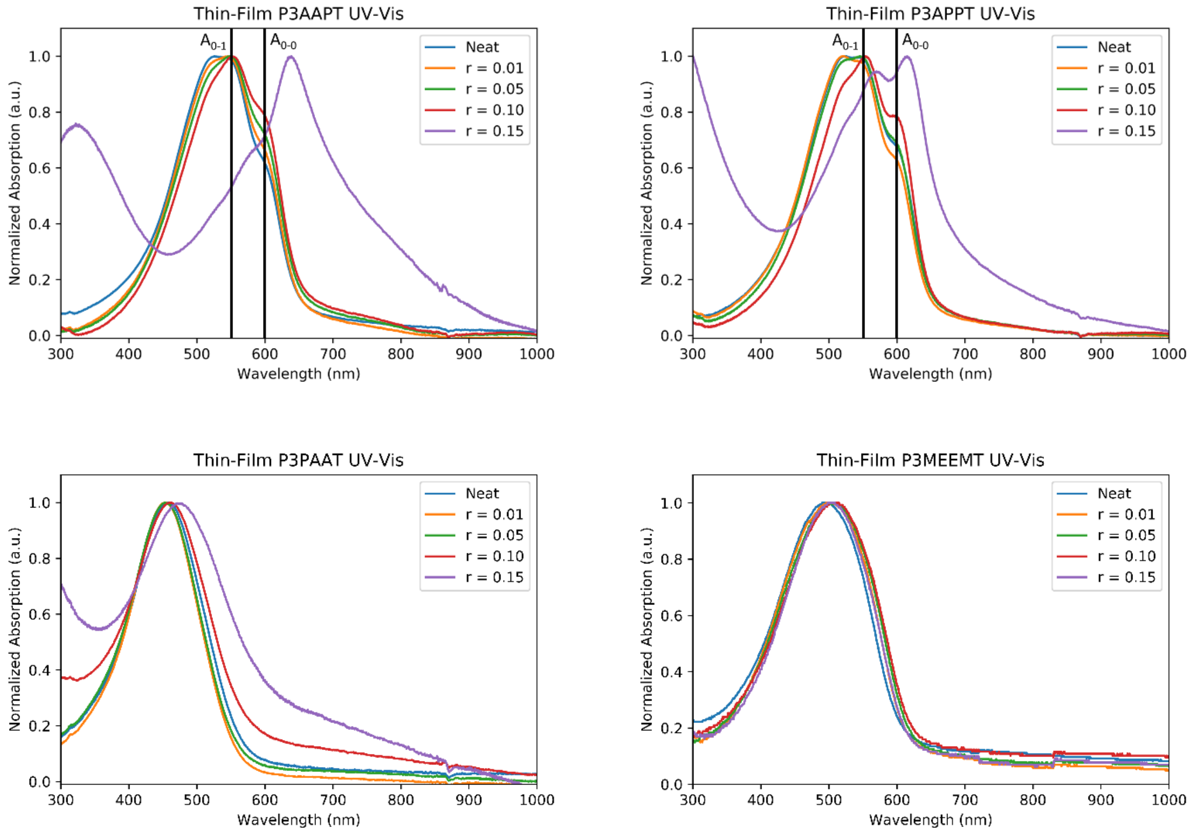

Figure 4.6: UV-Vis spectra for all four polymer samples with increasing r *values.*A_{0-0} *and* A_{0-1} *transitions labeled for clarity for P3AAPT and P3APPT.*

These samples show significant differences when compared to P3MEEMT's behavior with increasing LiTFSI; all polymers show notable spectral changes when LiTFSI is introduced. We see increasing planarization for both P3AAPT and P3APPT as the LiTFSI concentration increases. This is signified by an increase in both the 0-1 and 0-0 absorption peaks. The increased planarization of the P3AAPT and P3APPT comes along with a decrease in the absorption from the amorphous region of the polymer; this implies both an increase in the planarization and a reduction in the amorphous polymer content of the film. The origin of this planarization is unclear but could be due to either pre-aggregation and ordering of the polymer in solution prior to spin coating, or self-assembly upon drying due to the presence of LiTFSI in solution. Conversely, P3PAAT only shows an increase in scattering behavior, as shown in the longer-wavelength absorption tailing, with minimal changes in overall ordering. This observed scattering could be indicative of significant precipitation of LiTFSI out of the polymer matrix.

There is also a significant change in the spectral features for both P3APPT and P3AAPT at r = 0.15. For P3APPT and P3AAPT, the 0-0 peak shifts approximately 18 nm (597 to 615 nm 0-0 peak max) and 34 nm (605 to 639 nm 0-0 peak max), respectively. It is suggested that this spectral shift represents a significant transition into a structure with a highly planarized backbone. Single crystals of P3HT show a significant redshift in the 0-0 transition on the order of 70 nm, as compared to ordered P3HT samples.[215] Optical microscopy and AFM were taken of each polymer blend, to explore nanoscale structural changes with increasing r, the results of which are summarized in Table 3.3. Though P3APPT has a higher solubility of LiTFSI than either P3AAPT or P3PAAT, all polymers demonstrate significant precipitation and phase segregation of LiTFSI-rich phases at r = 0.15. Representative images of homogeneous and phase-segregated films are shown in the SI. It is seen that all polymers demonstrate lower solubility of LiTFSI than P3MEEMT, even when accounting for the reduction in each polymer's oxygen content. This implies that the ability of each polymer repeat unit to stably solvate a single Li^+ ion results in a significantly improved LiTFSI solubility, regardless of the side chain ordering.

Table 4.3: Summary of optical micrographs and AFM, highlighting observed phase-segregation and precipitation in LiTFSI doped polymers.

	Precipitation Observed?			
Polymer	r = 0.01	r = 0.05	r = 0.10	r = 0.15
P3AAPT	No	No	Yes	Yes
P3APPT	No	No	No	Yes
P3PAAT	No	Maybe	Yes	Yes
P3MEEMT	No	No	No	No

We propose that the structural change and planarization observed in the UV-Vis at r = 0.15 for P3AAPT and P3APPT is driven by precipitation and phase segregation of a LiTFSI-rich phase from a P3AAPT or P3APPT matrix. Given the earlier onset of precipitation for P3AAPT, it is suggested that the extent of phase segregation, and thus the driving force for planarization is larger for P3AAPT, corresponding to a larger redshift magnitude. Overall, LiTFSI introduction results in significant planarization of the polymer backbone for each of P3AAPT and P3APPT, though it does not result in significant changes for P3PAAT.

To investigate the evolving crystal structure with increasing r, XRD was performed on dropcast samples of the polymers on cleaned Si substates. Though all samples had the same exposure time, the relative crystallinity of samples cannot be determined due to variable sample thickness. The diffraction patterns for P3AAPT across all r are shown in Figure 4.7. Clearly present across all doping concentrations are the (100), (200), and even (300) peaks, and the (010) peak is present in the neat, as well as at $r = 0.01$ and 0.10. It's unclear why the (010) peak would be absent at $r = 0.05$, but present at 0.10, but it's possible this variation is due to sample thickness. It should be noted that the lack or presence of the (010) peak is more indicative of the limitations of the XRD system used, rather than as an indicator of a lack of π-stacking order. The blend shows a continually increasing (100) d-spacing for LiTFSI concentrations where $r \geq 0.05$, implying that at higher LiTFSi doping levels, the side chain direction is expanding to accommodate LiTFSI in the crystal structure. The (100) peak also broadens with increasing r, indicating decreasing orientation. The (200) peak at $r = 0.10$ has a notable shape, appearing as two distinct peaks, which, by $r = 0.15$ has fully resolved into the second peak. It's possible that this shows a LiTFSI concentration where two crystal structures coexist for the P3AAPT. It's also possible that the incorporation of the LiTFSI into the crystal structure follows an all-or-nothing type behavior, where once some LiTFSI is incorporated into the crystal, the full crystal transitions to a LiTFSI swelled crystal. It's possible that this transition is connected to the significant planarization seen in the UV-Vis, but given that this planarization is also seen in P3APPT, and no such XRD transition is seen, it is suspected that this is not the case.

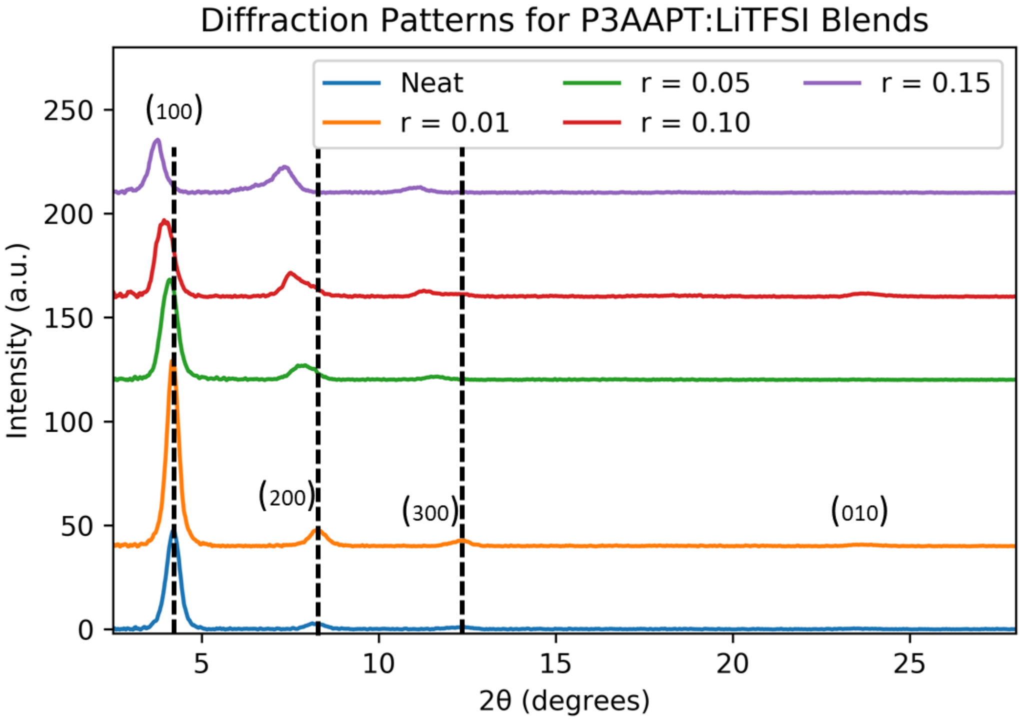

Figure 4.7: Diffraction patterns for P3AAPT across all values of r.

P3APPT (Figure 4.8) demonstrates a qualitatively similar diffraction pattern to P3AAPT, with (100), (200), and (300) peaks present in all samples, and a low intensity signal for the (010) peak. As can be seen by the vertical lines, the (*h*00) d-spacing consistently increases with increasing LiTFSI concentration. The diffraction pattern also does not show significant changes between the 0.10 and 0.15 samples, in spite of the significant planarization that was seen in the UV-Vis samples. It is apparent that though the backbone significantly planarizes, it does not improve the polymer's ability to crystallize, or result in significant changes to the crystal structure. Though P3APPT and P3AAPT show qualitatively similar diffraction patterns, P3PAAT's is notably different. As seen in Figure 4.9, only the (100) peak is consistently present, and the (200) fades above $r = 0.05$. Before $r = 0.15$, increasing LiTFSI content does not significantly change the d-spacing, and the overall magnitude of the shift at $r = 0.15$ is small.

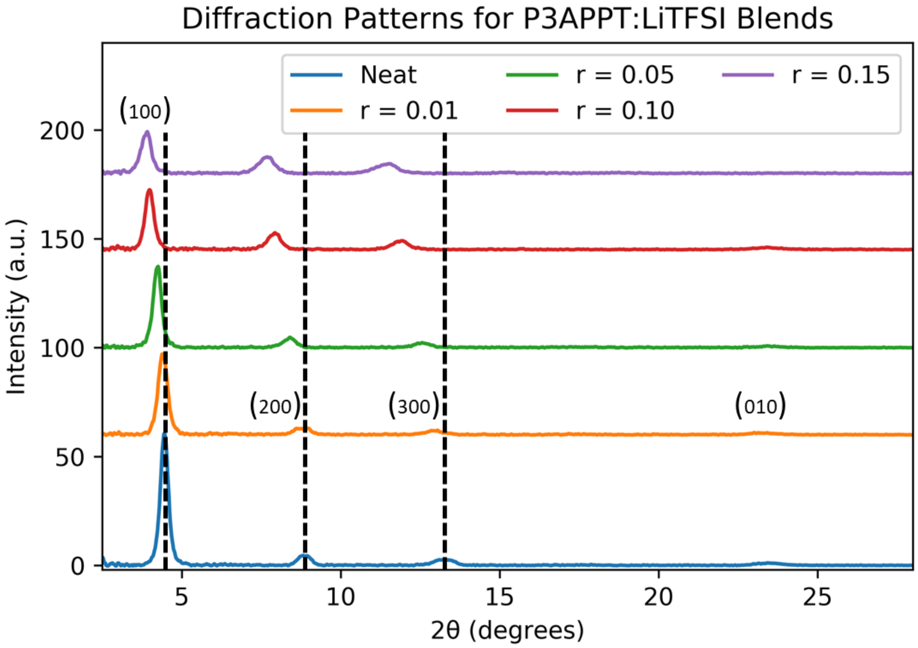

Figure 4.8: Diffraction patterns for P3APPT across all values of r.

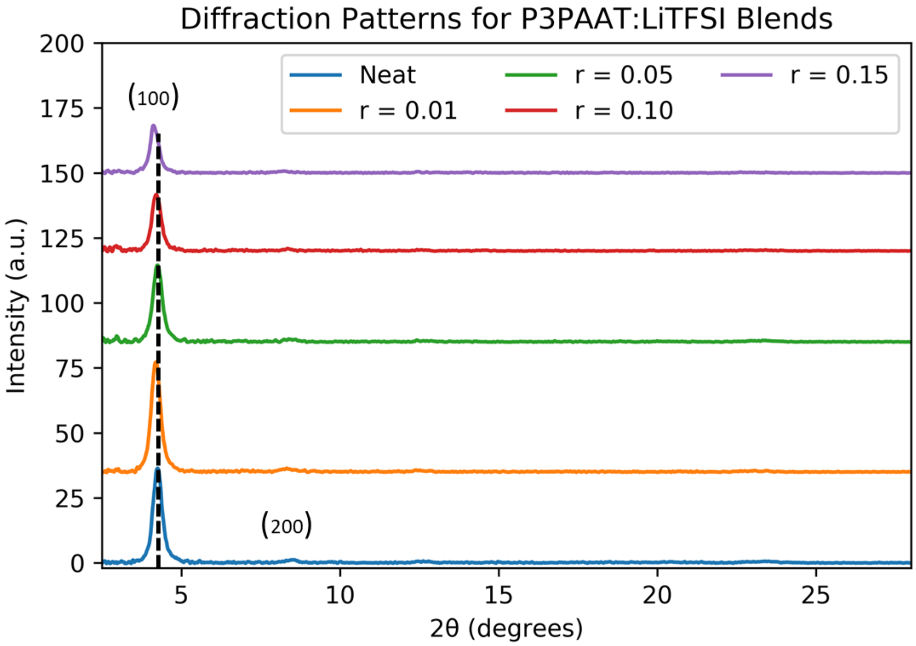

Figure 4.9: Diffraction patterns for P3PAAT across all values of r.

To quantify the effects of increasing LiTFSI content, the (100) d-spacing, as well as the (100) lattice strain was calculated and plotted in Figure 4.10. The [100] direction is important, as it represent the side chain direction, and represents the location for LiTFSI incorporation into the polymer crystal structure. To quantify variations in crystal structure with LiTFSI introduction, lattice strain is calculated for the d-spacing of the (100) plane. Lattice strain is calculated for a specific plane following Equation 4.3, where d_0 is the plane's d-spacing for the neat polymer, and d_r is the plane's d-spacing at a specific r.

$$Lattice\ Strain = \frac{d_r - d_0}{d_0} * 100\% \quad \text{Equation 4.3}$$

P3PAAT demonstrates very little (100) lattice strain, even at $r = 0.15$. This is in marked contrast to the $r = 0.15$ strain for both P3AAPT and P3APPT, which both show values larger than 10%. This is a significant amount of lattice strain; alkylated polythiophenes typically show lattice strains of less than 10% even under electrochemical ion injection.[187] The maximal lattice strain for both P3AAPT (11.7%) and P3APPT (13.8%) is comparable to P3MEEMT (10.5%).[141] The uptake profile for both polymers are slightly different, with P3APPT demonstrating an approximately linear uptake, whereas P3AAPT's uptake appears to be slightly superlinear, though it has an initially lower slope; however, both uptake profiles are unlike that of P3MEEMT. P3MEEMT rapidly swells to 10.5% at $r = 0.01$, then plateaus and does not swell further. It is interesting to see that, even though LiTFSI is clearly precipitating from the polymer structure at some values of r, additional ions are still being incorporated into the polymer crystal structure, as evidenced by the continued swelling of the (100) d-spacing. Overall, we see significant structural differences in our diffraction patterns with LiTFSI, with all samples showing some amount of swelling, though P3AAPT and P3APPT show significantly greater (100) lattice strain than P3PAAT. This implies greater uptake of LiTFSI into the polymer crystal structure for P3AAPT and P3APPT than P3PAAT.

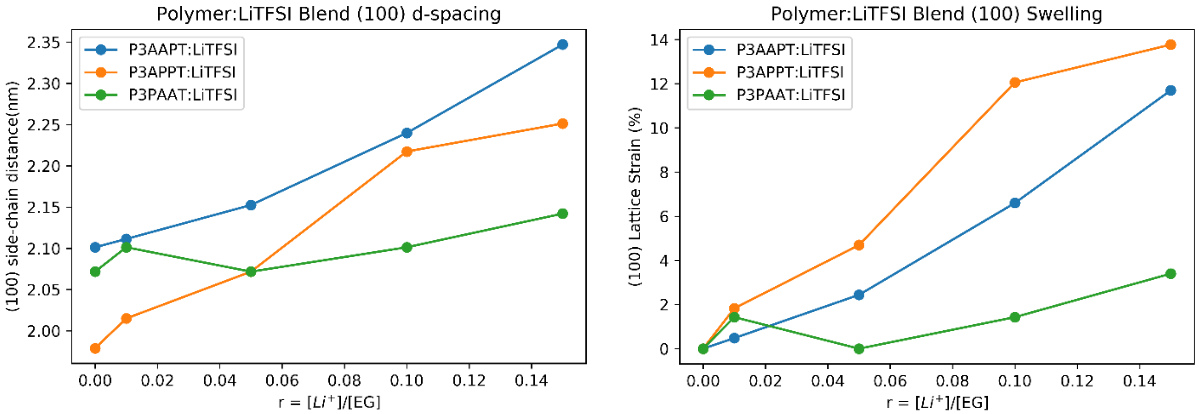

Figure 4.10: Polymer (100) plane d-spacing and lattice strain with increasing LiTFSI content.

4.4 Conclusions

A series of polymers with side chains containing varying oxygen contents and positions were investigated both computationally and experimentally. Molecular dynamics simulations were used to calculate ion mobility, as well as the energy of dissociation for a lithium salt for all possible polymer permutations. From these simulations, it was seen that there is a trade-off between the ion mobility and ion dissociation. A selection of these polymers were synthesized using KCTP, all with comparable molecular weights. The neat polymers were characterized, showing that there is increased backbone planarization that results from moving the oxygen atoms farther away from the polymer backbone. There are significant variations in crystal populations, with percent crystallinity again clearly suffering from the oxygen atom being adjacent to the polymer backbone. We also see that as the side chain identity changes, the T_m and side chain melting intensity changes. The influence of LiTFSI on the polymer morphology was investigated across a range of LiTFSI doping concentrations. It was noted that all polymers demonstrate a reduced solubility of LiTFSI compared to P3MEEMT, even when accounting for their reduced oxygen content. The neat backbone planarization differences were exacerbated by LiTFSI introduction; both P3AAPT and

P3APPT showed significant increases in planarization with increasing LiTFSI concentration. Both P3AAPT and P3APPT demonstrate greater (100) lattice strain when compared to P3PAAT across all LiTFSI concentrations, implying a greater uptake of LiTFSI into the polymer crystal structure. These variations highlight the significant influence on structure and performance that seemingly minor changes in side chain architecture create. From its better LiTFSI solubility and more stable crystal structure on LiTFSI addition, it is expected that P3APPT would be a higher performing MIEC material than either of P3AAPT or P3PAAT.

4.5 Supplemental Information

4.5.1 Monomer Synthesis and Characterization

4.5.1.1 Materials

3-thiophenemethanol was purchased from TCI. NBS was purchased from Sigma-Aldrich and recrystallized using a ratio of 100 mL of H_2O to 10 g of NBS. THF was dried and deoxygenated using a PureSolv solvent purification system. DCM was dried and deoxygenated on a SP-1 Stand Alone Solvent Purification System solvent purification system. All other chemicals were purchased from Sigma-Aldrich and used as received. All reactions are performed under air-free conditions, with glassware that was dried overnight in a 120 °C air oven.

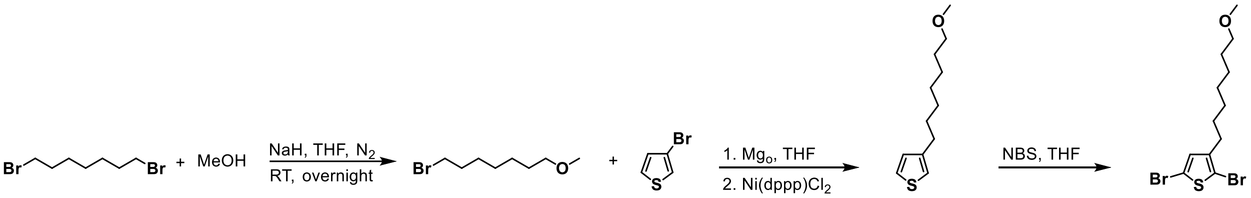

Scheme S4.1: Full synthesis scheme of 2,5-dibromo-3-(7'-methoxyheptyl)thiophene.

4.5.1.2 Synthesis of 7-bromoheptyl methyl ether

1,7-dibromoheptane (6.84 mL, 40 mmol) was added to a round bottom flask, then degassed under high vacuum for approximately 5 minutes. To a separate flask, anhydrous MeOH (0.54 mL, 13.3 mmol) and anhydrous THF (40 mL) were added. NaH (60% dispersion in mineral oil, 0.68 g, 17 mmol) was added in one portion, and the flask was quickly recapped. The NaH was allowed to react over 1 h, then the contents were transferred dropwise to the flask containing the 1,7-dibromoheptane. The reaction was then allowed to stir overnight. The reaction mixture was filtered through a fine frit to remove salt from the mixture. The product was washed through the frit with additional THF, then concentrated using rotary evaporation. The product was purified through silica column chromatography, using an eluent of hexanes/ethyl acetate at a ratio of 90/10, yielding 1.103 g of a clear viscous oil in 40.6 % yield.

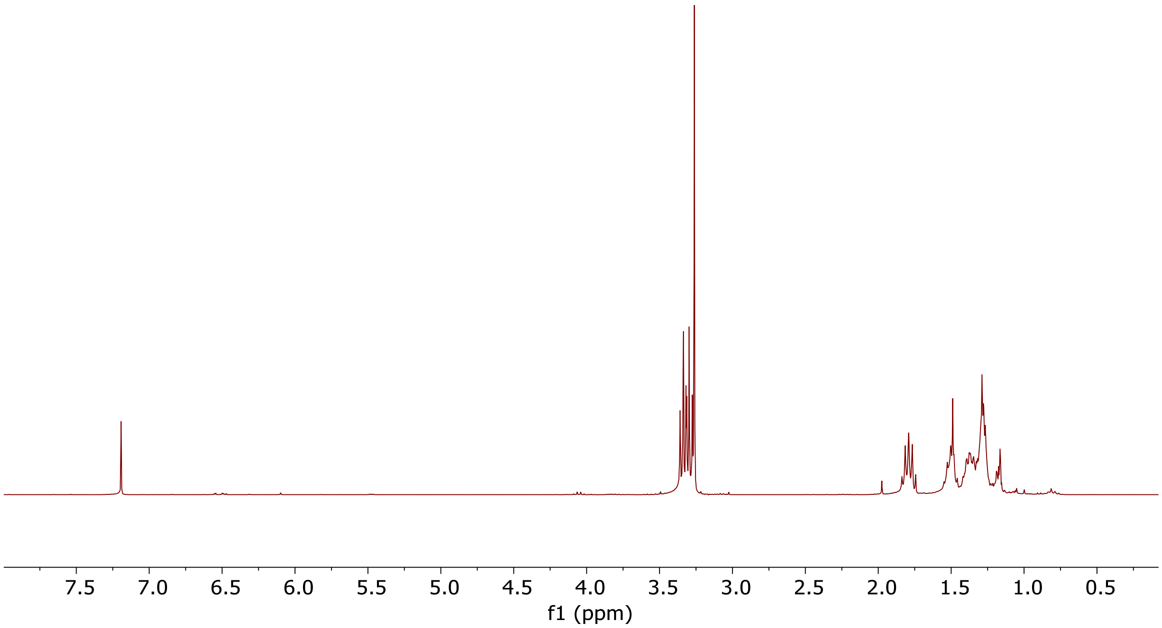

Figure S4.1: ^{1}H NMR of 7-bromoheptyl methyl ether

4.5.1.3 Synthesis of 3-(7'-methoxyheptyl)thiophene

Magnesium turnings (1.02 g, 42.4 mmol) were added to a 3-neck flask, and a condenser was added. The magnesium was flame-activated under high vacuum (additional entrainment agents could be used as well to improve yields). Following activation, THF (80 mL) and then 7-bromoheptyl methyl ether (8.390 g, 40.4 mmol) was added to the flask, then refluxed for 2 h. In a separate flask, 3-bromothiophene (3.212 mL, 34.30 mmol), and Ni(dppp)Cl_2 (437.3 mg, 0.807 mmol) were mixed under nitrogen with a small amount of THF (30 mL). The magnesium mixture was cooled to room temperature, and then the nickel mixture was added dropwise to the 7-magnesioheptyl methyl ether over a period of 15 min. After full addition of the 7-magnesioheptyl methyl ether, the reaction was heated, and refluxed overnight. The reaction was quenched with 150 mL 0.33 M HCl, then extracted 3 times with diethyl ether. The ether was dried over Na_2SO_4, and then concentrated under rotary evaporation. The crude product was purified using silica column chromatography using hexanes as an eluent, resulting in 5.96 g of a pale yellow oil as a product in an 82.0 % yield.

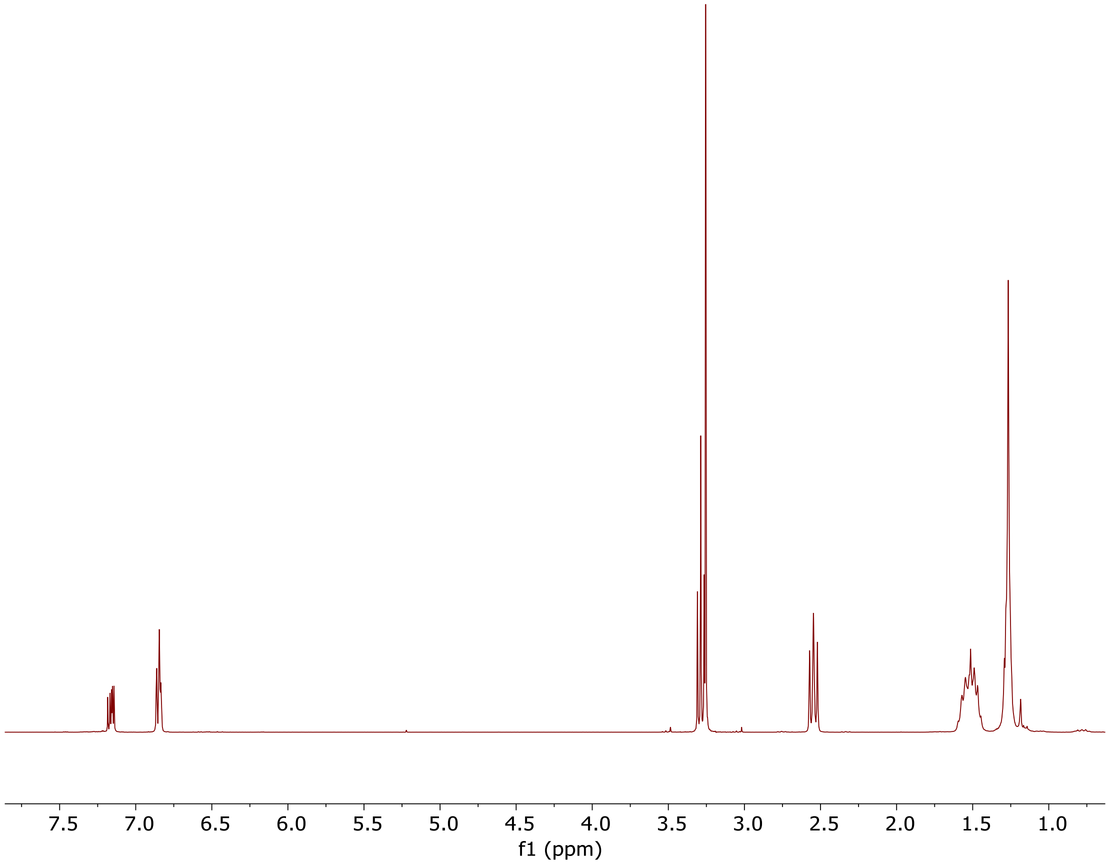

Figure S4.2: ^{1}H NMR of 3-(7'-methoxyheptyl)thiophene

4.5.1.4 Synthesis of 2,5-dibromo-3-(7'-methoxyheptyl)thiophene

To a round bottom flask, 3-(7'-methoxyheptyl)thiophene (5.95 g, 28.1 mmol) and anhydrous THF (26 mL) were added, and nitrogen was bubbled through for 15 min. Following bubbling, NBS (9.942 g, 55.9 mmol) was added in 5 equal portions, capping the reaction in-between each addition. The reaction was stirred overnight covered in foil at room temperature. The reaction was rotovapped to remove all THF, then the solids were filtered over a frit. The product was washed through the frit using hexanes. The hexanes was removed through rotary evaporation, then the crude product was purified using silica column chromatography with hexanes/ethyl acetate in a 95/5 ratio as an eluent, resulting in 5.441 g of a pale yellow oil as a product in a 52.4 % yield.

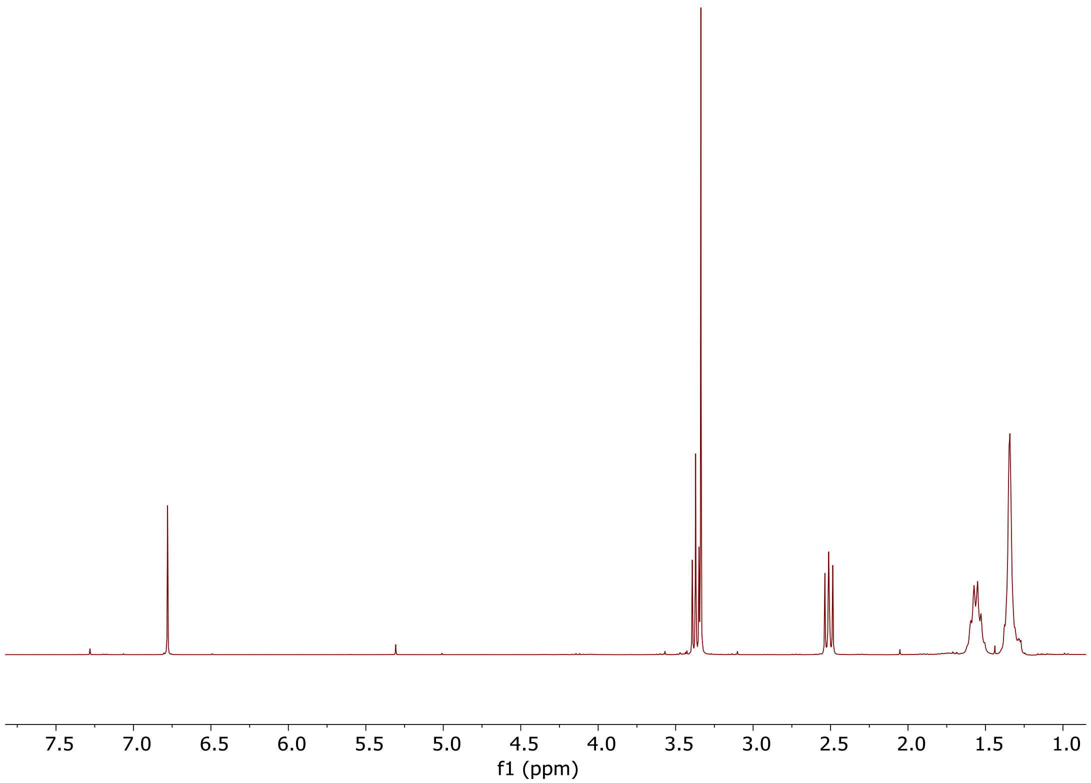

Figure S4.3: ^{1}H NMR of 2,5-dibromo-3-(7'-methoxyheptyl)thiophene

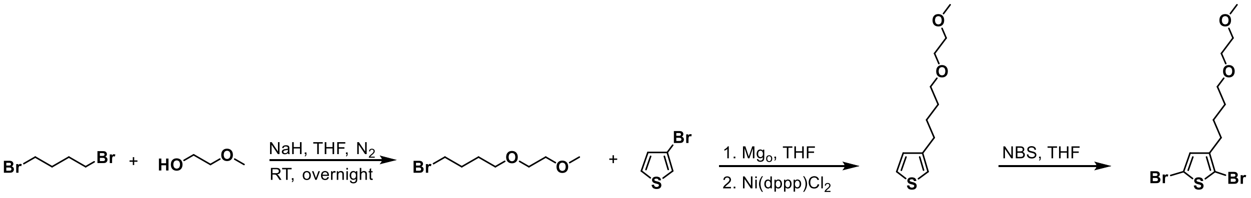

Scheme S4.2: Full synthetic scheme for 2,5-dibromo-3-(4'-(methoxyethoxy)butyl)thiophene.

4.5.1.5 Synthesis of 4-bromobutyl 2-methoxyethyl ether

1,4-dibromobutane (29.85 mL, 250 mmol) was added to a round bottom flask, then degassed under high vacuum for approximately 5 minutes. Then, 125 mL of THF was added to the 1,4-dibromobutane. To a separate flask, anhydrous 2-methoxyethanol (3.94 mL, 50 mmol) and anhydrous THF (75 mL) were added. NaH (60% dispersion in mineral oil, 2.5 g, 62.5 mmol) was added in one portion, and the flask was quickly recapped. The NaH was allowed to react over 10 min, then the contents were transferred dropwise to the flask containing the 1,4-dibromobutane. The reaction was then allowed to stir overnight. The reaction mixture was filtered through a fine frit to remove salt from the mixture. The product was washed through the frit with additional THF, then concentrated under rotary evaporation. The product was purified through silica column chromatography, using an eluent of hexanes/ethyl acetate at a ratio of 60/40, yielding 10.650 g of a clear viscous oil in 32.7 % yield.

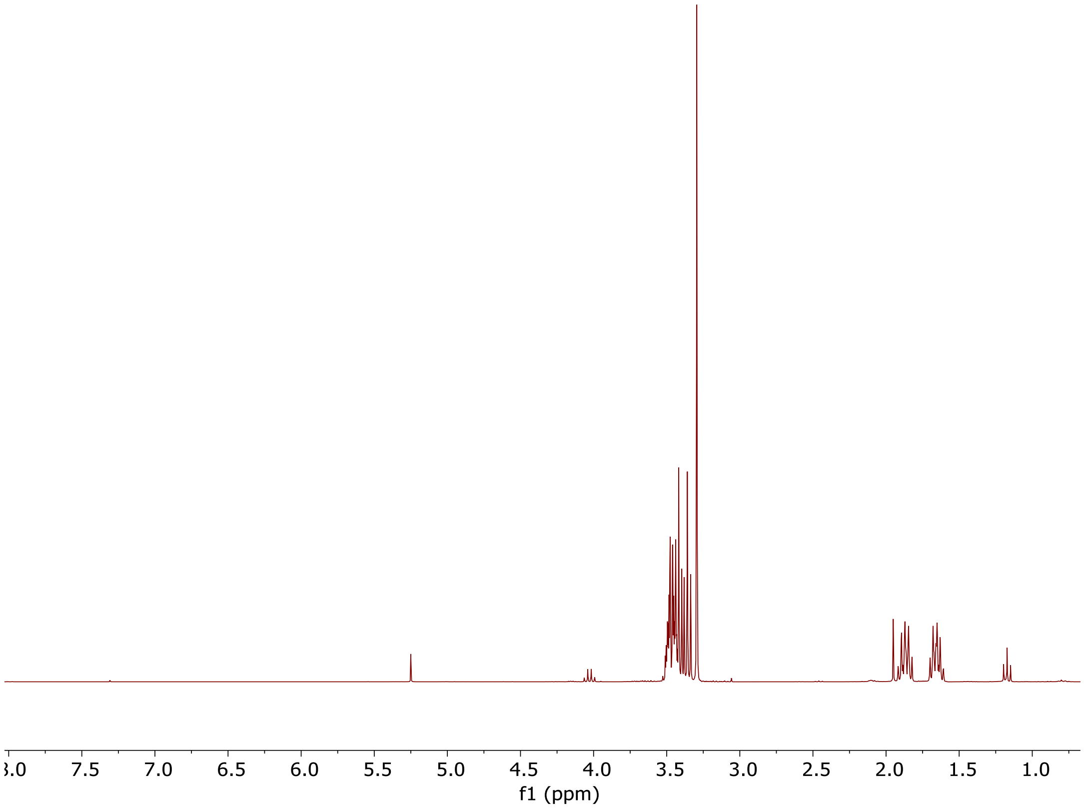

Figure S4.4: ^{1}H NMR of 4-bromobutyl 2-methoxyethyl ether

4.5.1.6 Synthesis of 3-(4'-(methoxyethoxy)butyl)thiophene

Magnesium turnings (1.97 g, 82.2 mmol) were added to a 3-neck flask, and a condenser was added. The magnesium was flame-activated under high vacuum (additional entrainment agents could be used as well to improve yields). Following activation, THF (80 mL) and then 4-bromobutyl 2-methoxyethyl ether (16.684 g, 78.33 mmol) was added to the flask, then refluxed for 2 h. In a separate flask, 3-bromothiophene (6.24 mL, 66.58 mmol), and Ni(dppp)Cl_2 (850 mg, 1.57 mmol) were mixed under nitrogen with a small amount of THF (40 mL). The magnesium mixture was cooled to room temperature, and then the nickel mixture was added dropwise to the 4-magnesiobutyl-2'-methoxyethyl ether over a period of 15 min. After full addition of the 4-magnesiobutyl 2-methoxyethyl ether, the reaction was heated, and refluxed overnight. The reaction was quenched with 150 mL 0.33 M HCl, then extracted 3 times with diethyl ether. The ether was dried over Na_2SO_4, and then concentrated under rotary evaporation. The crude product was purified using silica column chromatography using hexanes/ethyl acetate at a 70/30 ratio as an eluent, resulting in 7.468 g of a pale yellow oil as a product in a 51.5 % yield.

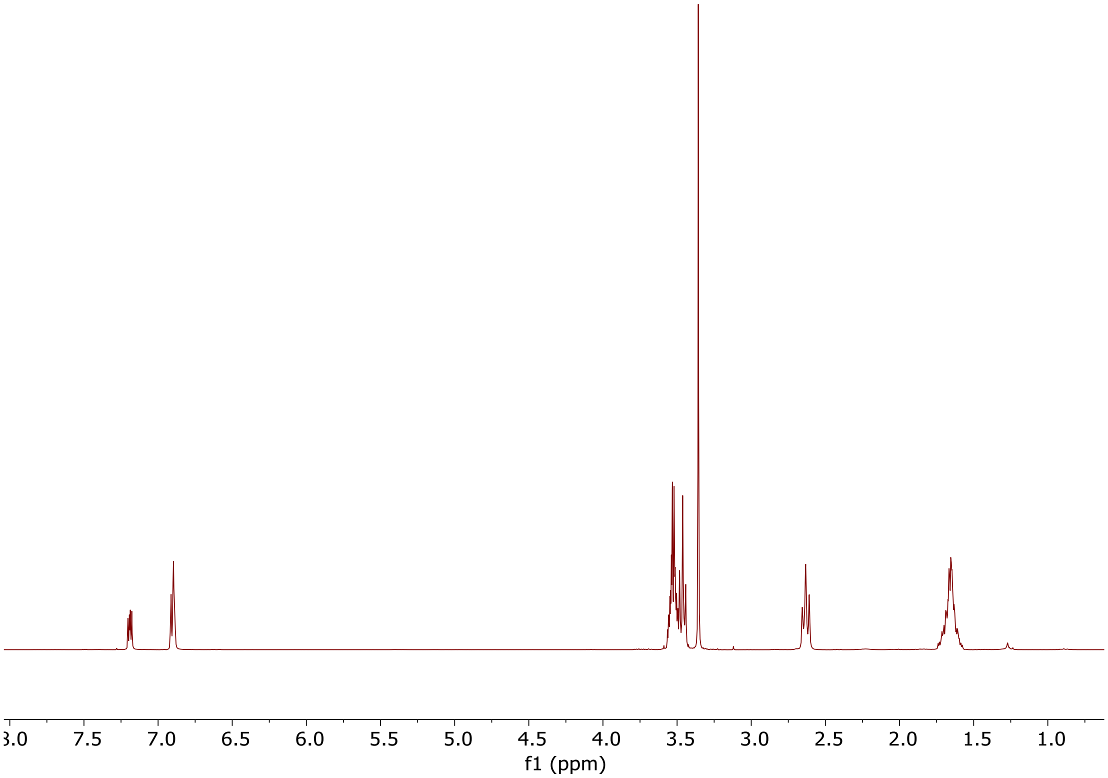

Figure S4.5: ^{1}H NMR of 3-(4'-(methoxyethoxy)butyl)thiophene

4.5.1.7 Synthesis of 2,5-dibromo-3-(4'-(methoxyethoxy)butyl)thiophene

To a round bottom flask, 3-(4'-(methoxyethoxy)butyl)thiophene (7.468 g, 35.4 mmol) and anhydrous THF (32.2 mL) were added, and nitrogen was bubbled through for 15 min. Following bubbling, NBS (12.58 g, 70.4 mmol) was added in 5 equal portions, capping the reaction in-between each addition. The reaction was stirred overnight covered in foil at room temperature. The reaction was rotovapped to remove all THF, then the solids were filtered over a frit. The product was washed through the frit using hexanes. The hexanes was removed through rotary evaporation, then the crude product was purified using silica column chromatography with hexanes/ethyl acetate in a 90/10 ratio as an eluent, resulting in 10.2314 g of a pale yellow oil as a product in a 78.5 % yield.

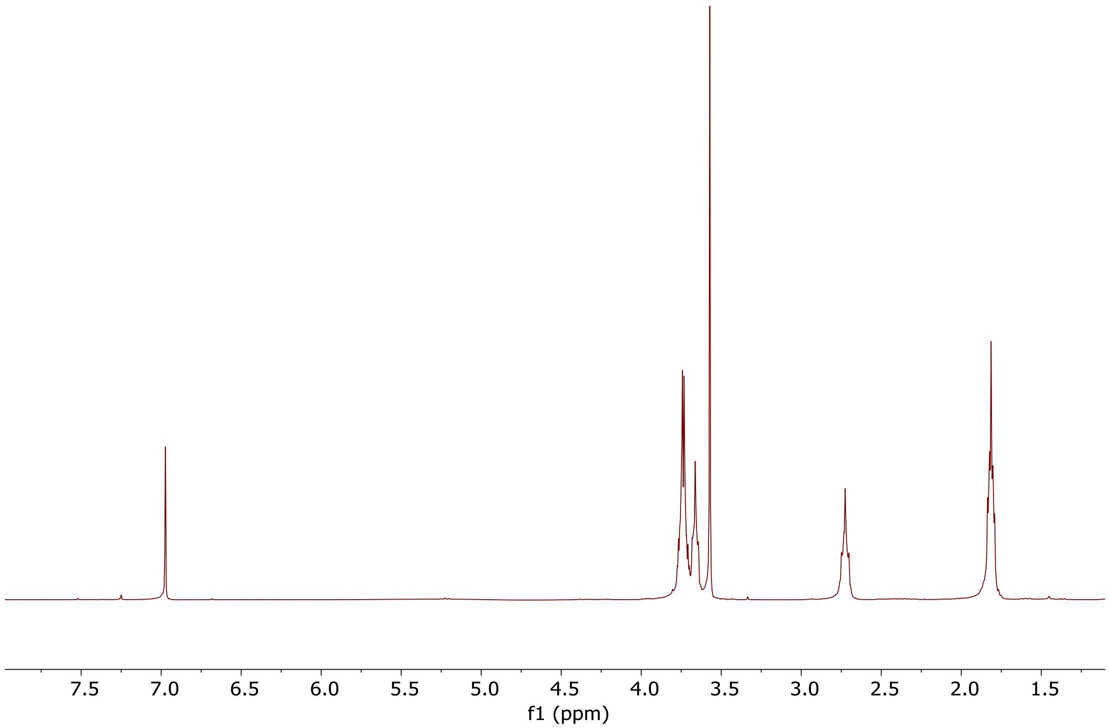

Figure S4.6: ^{1}H NMR of 2,5-dibromo-3-(4'-(methoxyethoxy)butyl)thiophene

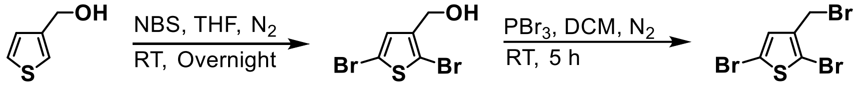

Scheme S4.3: Synthetic scheme for the synthesis of 2,5-dibromo-3-thiophene methyl bromide.

The next monomer starts from this core synthesis. This synthesis has been described previously but will be reported herein for clarity.[141,195]

4.5.1.8 Synthesis of 2,5-dibromo-3-thiophenemethanol

To a 3-neck flask, 3-thiophenemethanol (4.13 mL, 43.8 mmol) and anhydrous THF (40 mL) are added. The solution is degassed by bubbling nitrogen for 15 min, then NBS (15.5 g, 87 mmol) is added in 5 equal portions, allowing time to stir in between additions. The mixture is then stirred overnight at room temperature. After reacting, the solvent is removed by rotary evaporation. The residue is washed with hexanes and filtered, rinsing until the rinsate is no longer UV-active. The product was purified by eluting over silica gel with a 4:1 mixture of hexanes to ethyl acetate. The product was collected as 10.745 g of a white solid in 90.9 % yield.

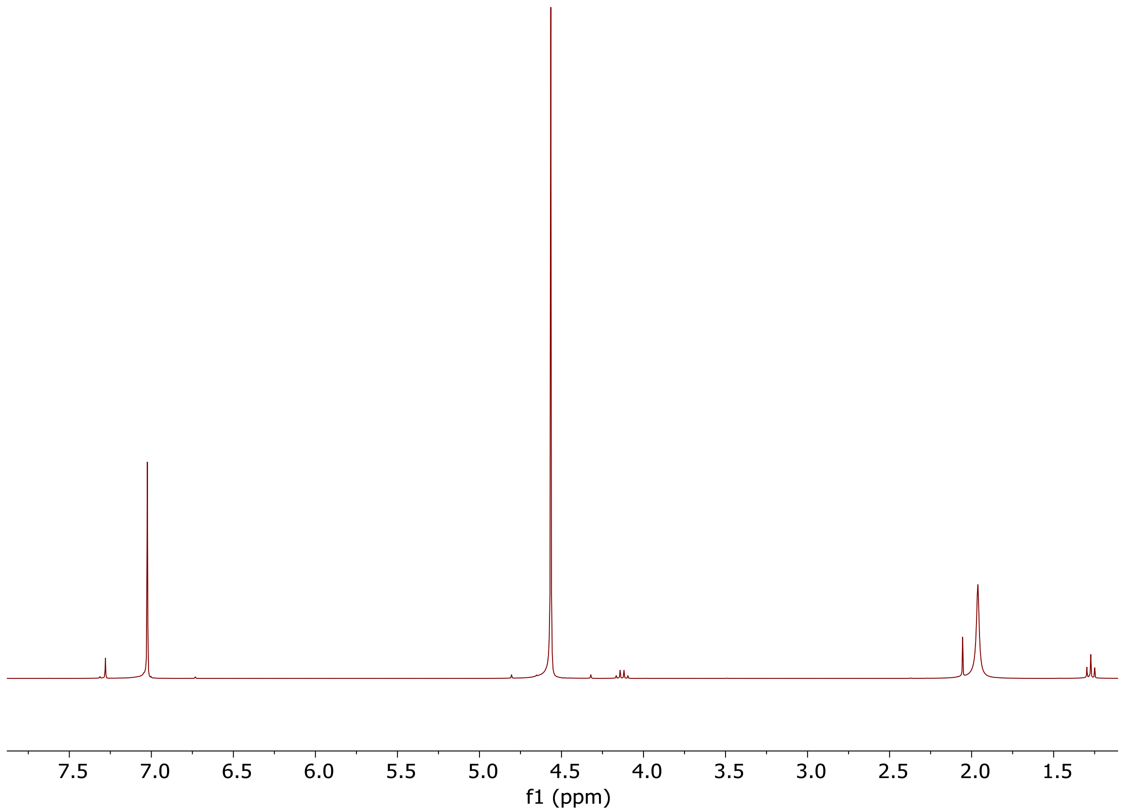

Figure S4.7: ^{1}H NMR of 2,5-dibromo-3-thiophenemethanol

4.5.1.9 Synthesis of 2,5-dibromo-3-thiophenemethylbromide

To a round bottom flask, 2,5-dibromo-3-thiophenemethanol (4.204 g, 15.6 mmol) and anhydrous DCM (80 mL) were added. The flask was placed on ice for 20 min, then PBr_3 (1.50 mL, 15.9 mmol) was added dropwise over 15 min. The reaction was allowed to stir at room temperature for 5 h. The reaction was quenched by addition of a 10% aqueous $NaHCO_3$ solution. The product was extracted with dichloromethane, washed with brine, then dried with $MgSO_4$ and filtered. The solvent was removed, and the product was stored at -20 °C overnight, after which a white solid was collected in 92.5 % yield.

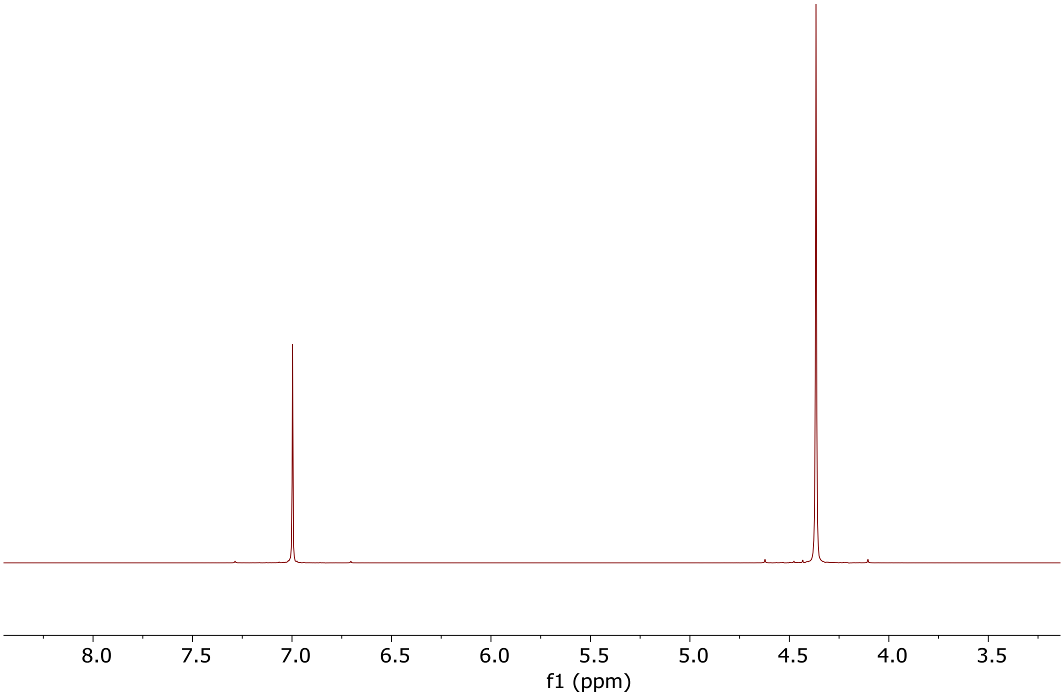

Figure S4.8: ^{1}H NMR of 2,5-dibromo-3-thiophenemethylbromide

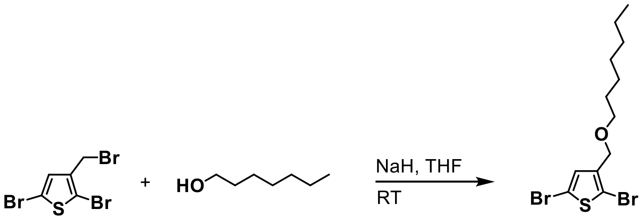

Scheme S4.4: Synthetic scheme of 2,5-dibromo-3-(1'-heptoxymethyl)thiophene.

4.5.1.10 Synthesis of 2,5-dibromo-3-(1'-heptoxymethyl)thiophene

Anhydrous 1-heptanol (6.285 mL, 44.5 mmol) and THF (120 mL) were added to a 3-neck flask with an attached addition funnel. Then, NaH (60% dispersion in mineral oil, 2.027 g, 50.7 mmol) was quickly added in one portion, and the NaH was allowed to react for 2 h (note that this time is significantly longer than is needed for the synthesis of 2,5-dibromo-3-(methoxyethoxyethoxymethyl)thiophene; it appears that the 1-heptanol reacts at a significantly slower rate than diethylene glycol monomethyl ether). 2,5-dibromo-3-thiophenemethylbromide (14.270 g, 40.4 mmol) was dissolved in THF (60 mL), then added to the addition funnel. The 2,5-dibromo-3-thiophenemethylbromide was added dropwise over a period of 15 minutes, then stirred at room temperature overnight. The reaction mixture was filtered over a thin pad of Celite, then the product was washed through with THF. The solvent was removed using rotary evaporation, and the product was purified through column chromatography in pure hexanes. Note that initial TLC shows un-representative values due to the influence of residual 1-heptanol on the R_f of the product. The product was collected as 13.777 g in an 91.6 % yield as a pale yellow oil, and stored at -20 °C.

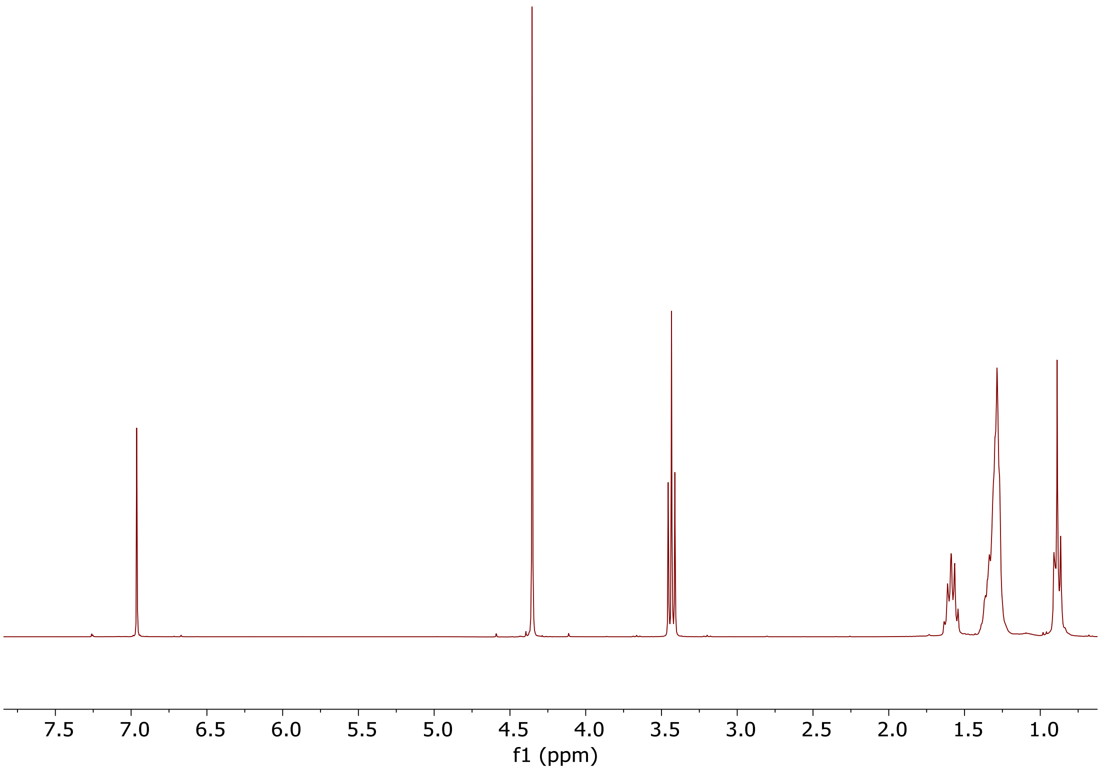

Figure S4.9: ^{1}H NMR of 2,5-dibromo-3-(1'-heptoxymethyl)thiophene

4.5.2 Polymer Synthesis

4.5.2.1 General Procedure for the Synthesis of Polymers

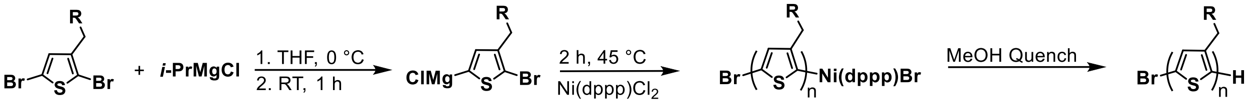

Scheme S4.5: Generalized reaction scheme for polymerization of modified side chain polymers.

A generalized procedure for the polymerization of all monomers is shown in Scheme S4.5. All polymers made herein follow this procedure. To a dried Schlenk flask, dibrominated monomer (5 mmol) was added, and then degassed under high vacuum for 30 min. Following degassing, the flask was returned to a nitrogen atmosphere, and the monomer was diluted with 50 mL of anhydrous THF. The monomer was stirred rapidly, and then was cooled to 0 °C, and *i*-PrMgCl (2.475 mL, 4.95 mmol, 2.0 M) was added dropwise over 10 min. The flask was then warmed to RT and allowed to stir for 1 h. When the Grignardization is complete, the flask is placed in an oil bath at 45 °C. Then, Ni(dppp)Cl_2 (23.331 mg, 0.0430 mmol) is added quickly and in one portion with rapid stirring, and the flask is quickly recapped. The polymerization was allowed to continue for 2 h, and then was quenched with 5 mL of 5M HCl, then precipitated into MeOH. The polymer was collected by filtration. The solid polymer powder was purified by Soxhlet extraction, using first MeOH, and then the purified polymer was extracted with $CHCl_3$. The purified polymer was again precipitated into MeOH and collected by filtration.

4.5.2.2 P3APPT Synthesis

Following the above general procedure, 250.5 mg of P3APPT was synthesized with M_n = 10.5 kg/mol, $Đ$ = 1.51.

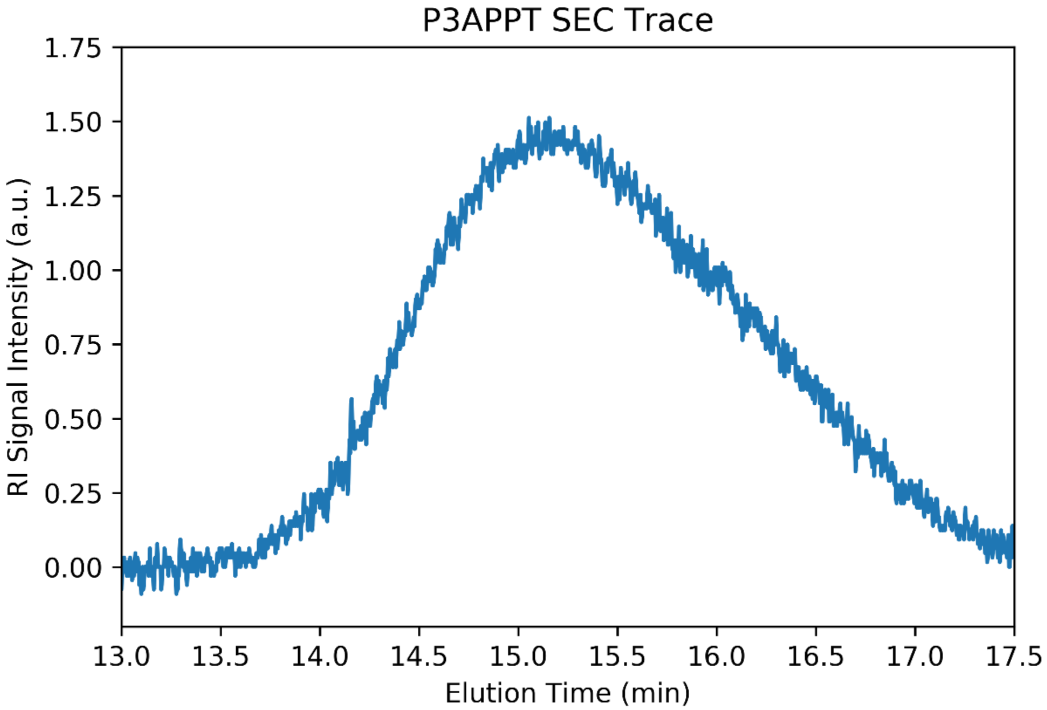

Figure S4.10: SEC Trace for P3APPT.

4.5.2.3 P3AAPT Synthesis

Following the above general procedure, 272.3 mg of P3AAPT was synthesized with M_n = 12.4 kg/mol, *Đ* = 1.38.

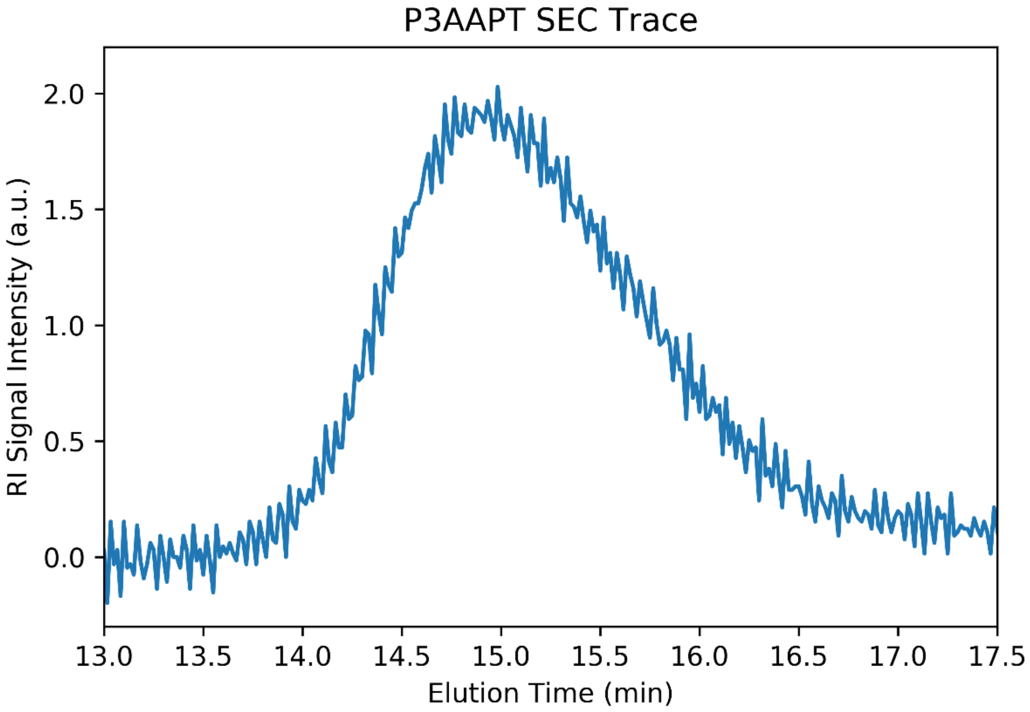

Figure S4.11: SEC trace for P3AAPT.

4.5.2.4 P3PAAT Synthesis

Following the above general procedure, 258.9 mg of P3PAAT was synthesized with M_n = 9.1 kg/mol, $Đ$ = 1.91.

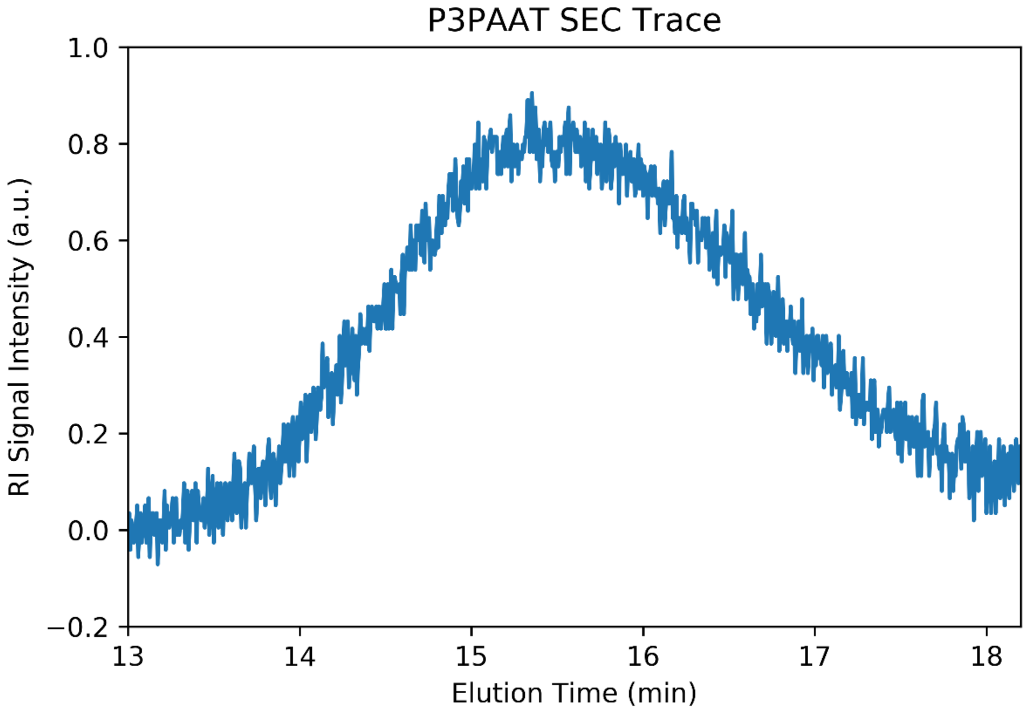

Figure S4.12: SEC Trace for P3PAAT.

4.5.3 Thermogravimetric Analysis (TGA)

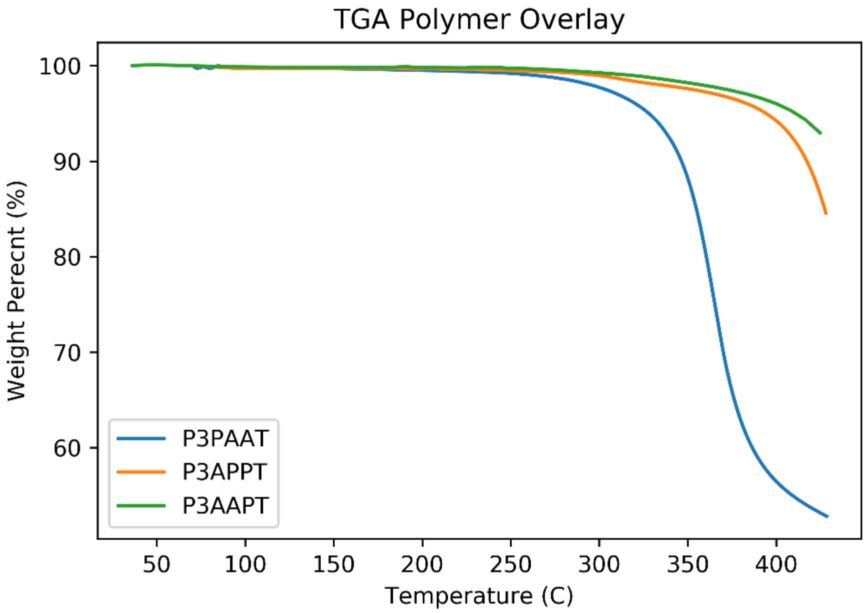

Figure S4.13: TGA data for all polymers, performed under a N_2 atmosphere.

4.5.4 Differential Scanning Calorimetry (DSC)

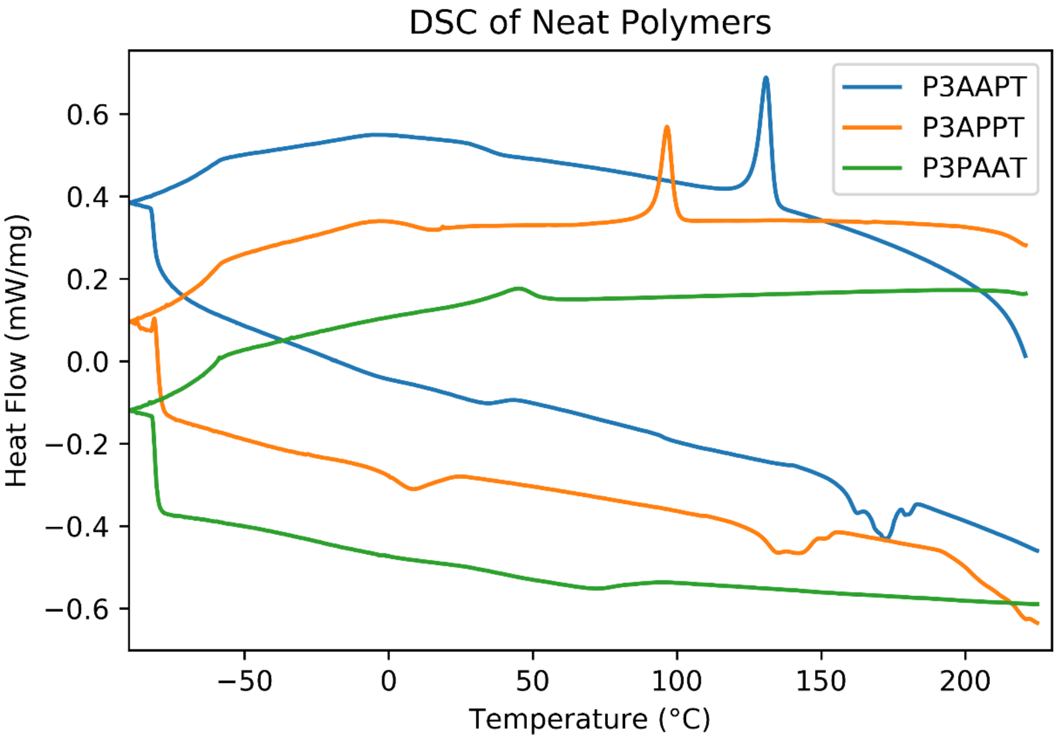

Figure S4.14: Overlaid DSC traces of neat polymers. Note that polymer traces were shifted vertically for clarity. Plotted traces show the cooling cycle and the second heat cycle, taken at 10 °C/min.

4.5.5 Solution UV-Vis Spectra

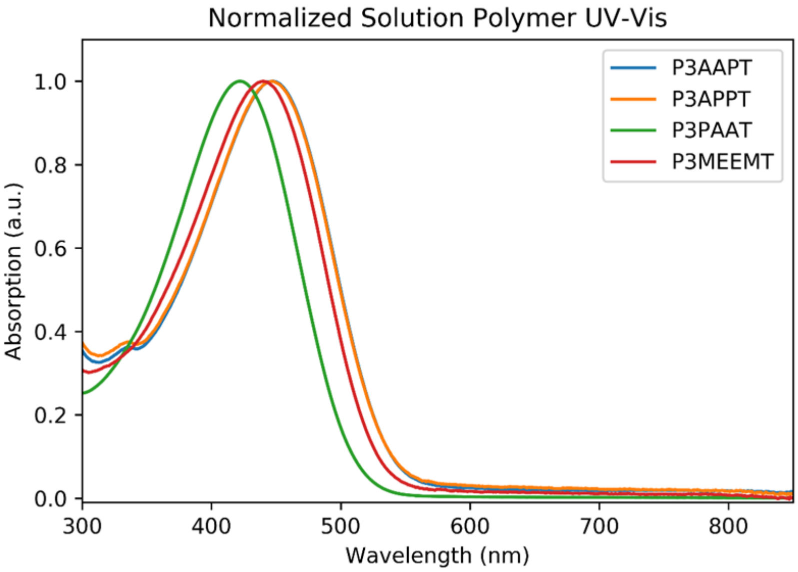

Figure S4.15: Solution UV-Vis spectra for all polymers, normalized to a maximum absorbance of 1.

4.5.6 Atomic Force Microscopy (AFM) and Optical Microscopy

AFM images and optical images highlighting polymer blend samples that both did and did not display phase segregation behavior.

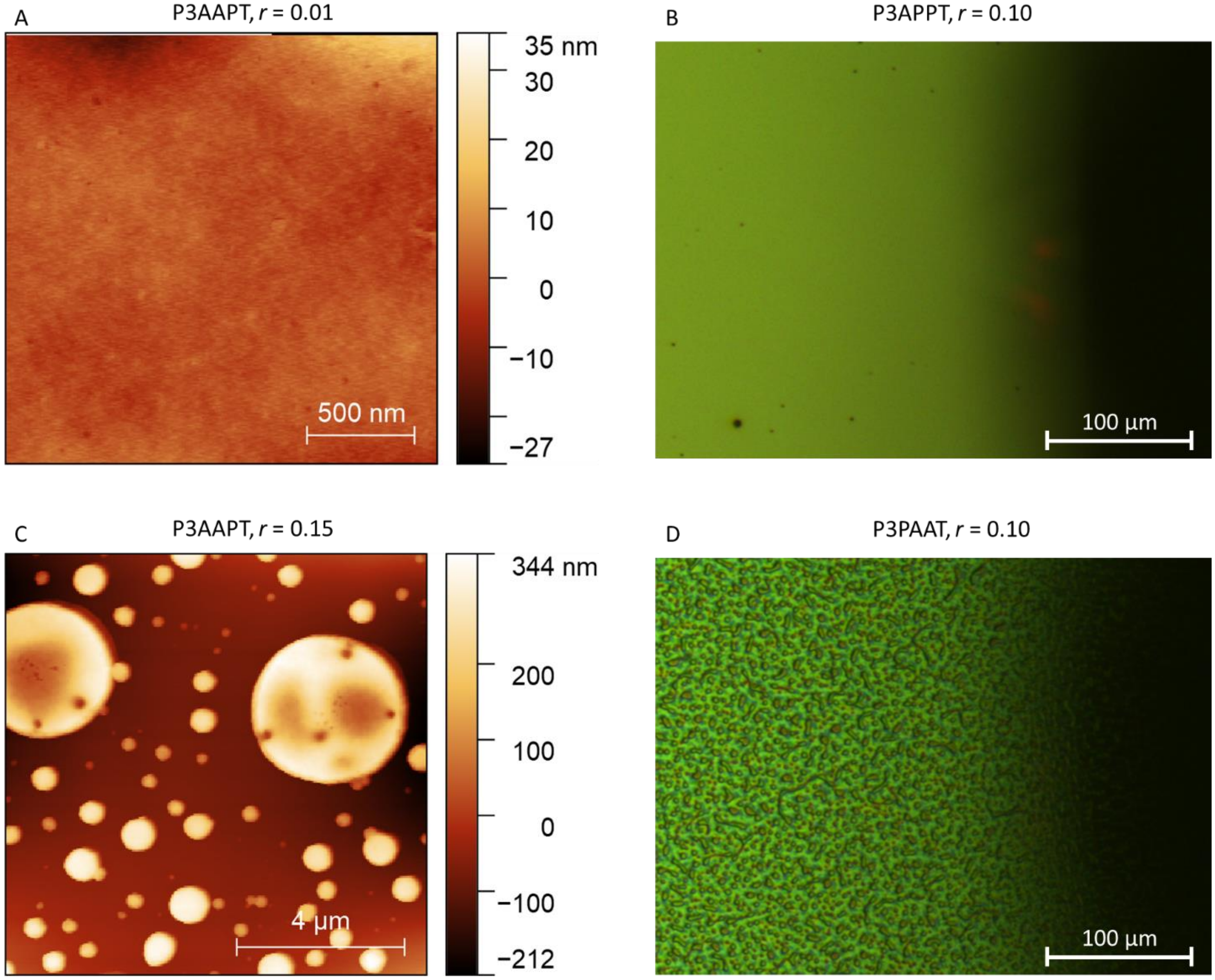

Figure S4.16: A: AFM data for P3AAPT showing homogeneous mixing. B: Optical micrograph showing homogeneous distribution for P3APPT with r *= 0.10. C: P3AAPT at* r *= 0.15 showing significant phase segregation. D: P3PAAT at* r *= 0.10 optical microscopy showing widespread phase segregation.*

4.5.7 Molecular Dynamics Calculations

4.5.7.1 Lithium Ion Mobility Measurements

In order to simulate the mobility of ions in each polymer, Li^+ ions were introduced at a ratio of $r = 0.02$ into each of the equilibrated structures and an electric field is applied. The motion of the ion under this applied electric field are then tracked, and the mobility of the ions was extracted following Equation S4.1. MSD is mean-squared-displacement and represents the squared positional change of an ion over a fixed amount of time, t. v represents the drift velocity of the observed ion. Drift velocity is a product of the applied electric field, E, and the ionic mobility, μ; this substitution enables the direct comparison of MSD with mobility.

$$MSD \approx (vt)^2 = (E\mu)^2 t^2 \qquad \text{Equation. S4.1}$$

In order to remove the effect of ions that were trapped, and thus not representative of truly mobile ions, only ions that followed a parabolic dependence of their location with time were used for calculating mobility. A representative trace of this type of parabolic behavior is shown in Fig. S4.17. To facilitate extraction of the material mobility, the raw MSD data for each ion was fit with a parabolic curve, and this fit was used to extract the mobility using Equation S4.1.

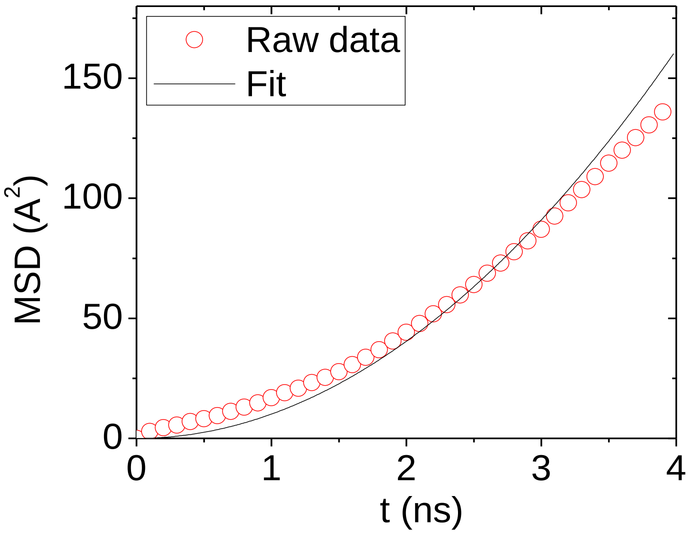

Figure 4.17: Representative trace of the dependence of MSD with time for an ion in P3MEEMT.

4.5.7.2 Methodology for Determination of E_d

In order to control for variations in the oxygen concentration, the influence of oxygen concentration on dissociation of lithium salts must be handled. To model the dissolution of salts, we can use an Arrhenius expression which is dependent on the dielectric constant, ε, and the activation energy of dissociation, E_a, as well as the Boltzmann constant, k_b, and temperature, T, as shown in Equation S4.2.[216]

$$rate \propto e^{\frac{-E_a}{\varepsilon k_b T}} \qquad \text{Equation S4.2}$$

The same salt pairing will have the same E_a across all polymers; the varying component will be ε. As such, we can create a modified energy term, E_d, which represents the ratio of E_a and ε, and insert it into a more standard conductivity equation to create an environment-specific consideration for ion-dissolution processes.

In order to calculate the E_d for all polymers, an approximation based on the force of interaction (Potential Mean Force, PMF) between a salt pair is used. For computational simplicity, LiCl is used as our salt pair. To calculate the approximate force, the ions are held at a specific separation distance, r_{sep}, and the force on the ions determined. For an isotropic environment, such as bulk water, the relative orientation of the salt to the environment is not important due to symmetry; however, for the crystalline and amorphous environments of our systems, there is significant heterogeneity. As such, the ions must be allowed to freely self-adjust at the given r_{sep} before measuring the forces that they are experiencing, to mitigate non-equilibrium forces. To implement this, the ions are placed into the system, and then given time to self-adjust while maintaining the distance between the two ions. After allowing the ions to equilibrate, the mean force, *MF*, on the ions are calculated, following:

$$MF(r_{sep}) = \langle (\overrightarrow{F_{Li^+}} - \overrightarrow{F_{Cl^-}}) \cdot \vec{r} \rangle \qquad \text{Equation S4.3}$$

Where $\overrightarrow{F_i}$ represents the force on ion i, and $\vec{r}$ represents the instantaneous unit vector between the ions. To calculate the potential mean force (PMF) from this, the ions are placed at an initial r_{sep} of 2 Å, and r_{sep} is increased to 15 Å in increments of 0.2 Å. The ions are held at each r_{sep} for 0.5 ns to get an average value of MF at each point. To determine the energy required to take an ion from a given value of r_{sep} to an infinite separation (*ie*, dissociation), the PMF can be calculated using:

$$PMF(r_{sep}) = \int_{r_{sep}}^{r_{max}} MF(r)dr \qquad \text{Equation S4.4}$$

Where r_{max} is the maximum separation calculated (15 Å, in this case). Example images showing force directions, ion positions within a crystal lattice, and the calculated PMF for r_{sep} over a full range of dissociation can be seen in Figure S4.18. For the purposes of clarity, the value of PMF(r_{max}) has been shifted to 0. The r_{max} should be taken to be large enough to see a plateau in the PMF, as is highlighted in the bottom right of Figure S4.18. To determine the value for E_d, the difference in PMF is taken between the largest and smallest observed values.

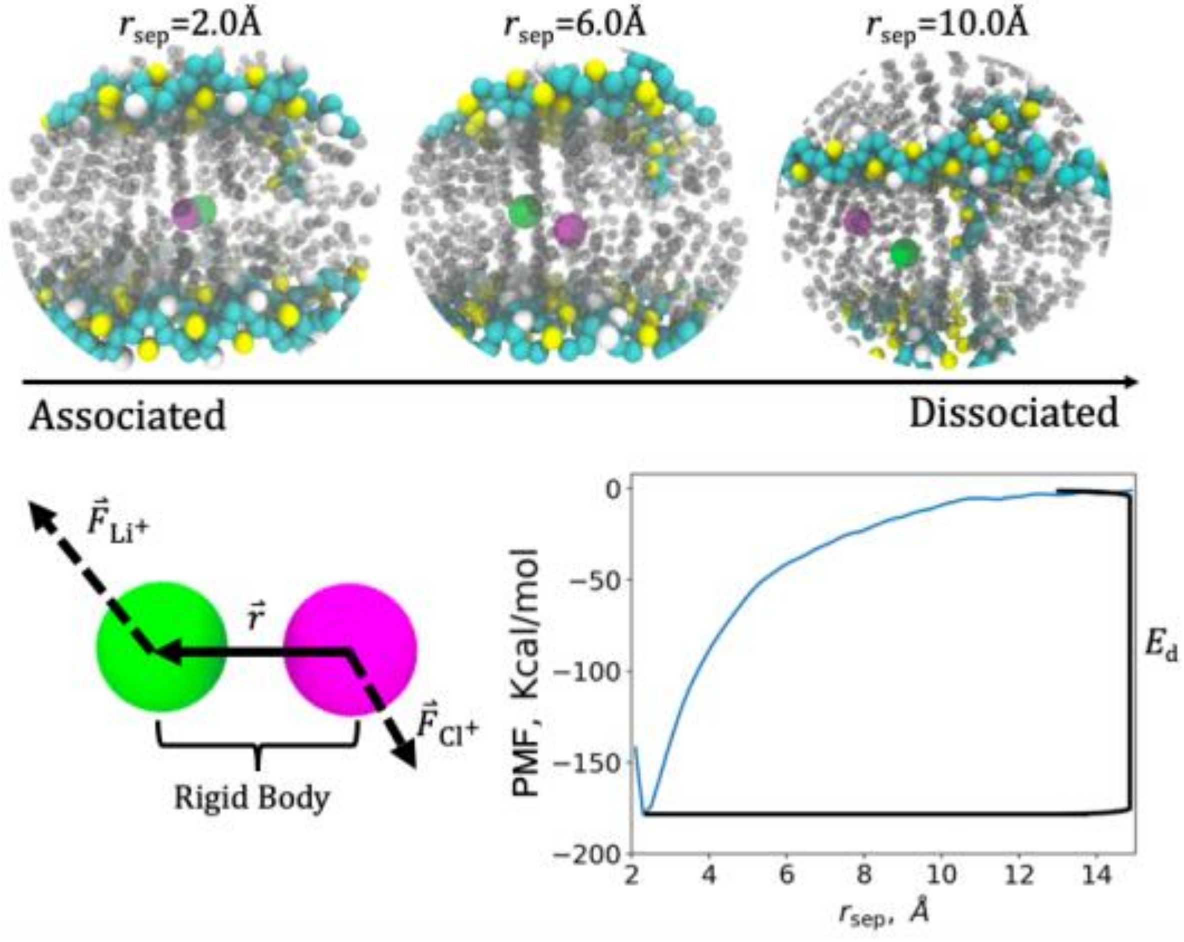

Figure S4.18: Top: A schematic of how the distance between Li+ and Cl- is increased, ranging from an associated state to a dissociated state. Bottom: a schematic of the variables used in equation 3.4 to calculate the PMF, and an example plot of PMF integrated over r_{sep} *to give the change in energy, ΔE, for an ion pair going from the dissociated state to a given* r_{sep}*. Carbon, Sulfur, Hydrogen, Lithium, and Chlorine are colored as cyan, yellow, white, green, and purple. The side chains are colored transparent grey for clarity.*

Ch. 5: Conclusions and Future Recommendations

5.1 Ionic Conductivity and GIWAXS for Reduced-Oxygen Content Polymers

Continuing the investigations into the influence of variation of oxygen concentration and position along the side chain would be highly valuable. In particular, measurements of the ionic conductivity of the polymer would enable the connection of morphological changes with LiTFSI introduction to resultant ionic conductivity, deepening understanding of their connection, and helping to sort important from extraneous morphological features. GIWAXS information would further supplement this understanding by enabling more specific information to be extracted from diffraction studies, including things like crystal texturing and crystallite orientation, as well as relative crystallinities with different LiTFSI concentrations. Further supporting the understanding of crystallite changes with LiTFSI, DSC data for samples with LiTFSI introduced would be quite valuable, as it would enable discussions of crystal melting temperature suppression, crystal quality, and percent crystallinity of our samples.

5.2 Molecular Weight Dependence of MIEC Performance

A critical research thrust for moving the MIEC field forward in developing predictive models for MIEC performance revolves on investigating the molecular weight dependence of ionic conduction in P3MEET and P3MEEMT. It is well-established in conjugated polymer literature that there is a strong connection between molecular weight and charge conduction. The ionic conduction of non-conjugated samples has been studied in relation to polymer molecular weight. Linear, non-conjugated PEO-based polymer samples demonstrate a significant decrease in ionic conduction with increasing molecular weight.[42] As molecular weight increases, T_g and percent crystallinity also increase, significantly reducing the chain segmental mobility.[39,41] By introducing

PEO as a side chain, rather than as a main chain, crystallinity is suppressed. This can allow for the polythiophene backbone to be made at various molecular weights without resulting in a highly crystalline sample. It has been seen in block copolymers that increasing molecular weight of the PEO block increases ionic conductivity significantly, as shown in Figure 5.1.[217] Similar effects from the introduction of high-molecular weight, non-conjugated brush polymers have also been observed; however, no such studies have been performed in conjugated systems.[218]

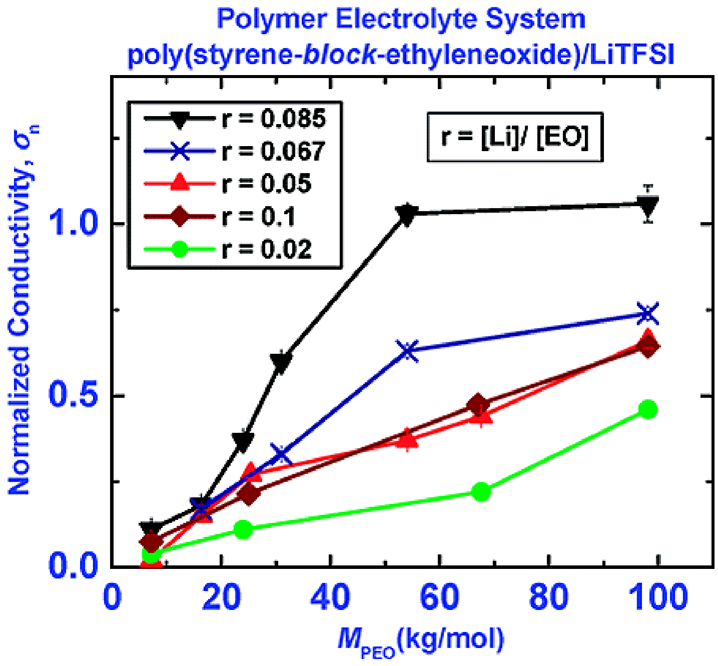

*Figure 5.1: Evolution of conductivity of PEO-*b*-PS with increasing molecular weight. Reprinted with permission from reference 217. Copyright (2009) American Chemical Society.*

A valuable aspect of the KCTP reaction is its quasi-living nature. By varying the feed ratio of the catalyst to the monomer, the molecular weight of the produced polymer can be precisely controlled. By taking advantage of this property, polymers with a broad spread of molecular weight can be synthesized. It would be possible to use KCTP to synthesize samples of P3MEEMT with a spread of molecular weights from 5 kg/mol to 40 kg/mol. This large spread should allow access to a wide range of morphologies, especially when considering the potential variations in morphology that can be observed by thermally annealing polymer samples. At low molecular weights, poly(3-

alkylthiophenes) tend to form highly crystalline structures with extremely poor intercrystalline connectivity, a fact which reduces electronic conduction significantly. It seems as though this trend of reducing electronic mobility is exacerbated in OECT device operation due to the swelling of the polymer under aqueous operation, based on recent work that focused on lower molecular weight P3MEEMT OECTs.[219] At higher molecular weights, a significant number of intercrystalline tie-chains should exist, maintaining the electronic connections during device operation. This would also have the effect of improving electronic conductivity in dry operating conditions. Understanding the connection between molecular weight and ionic conduction in conjugated polymers requires additional exploration to achieve similar levels of understanding. It is well known that for conjugated polymers we see a significant increase in electronic mobility with increasing molecular weight up to a certain molecular weight, above which the value for electronic mobility plateaus; It is anticipated that there will be a similar behavior in both electronic mobility as well as ionic conductivity for MIEC polymers, but no such study has yet been produced. An advantage of this study is that it also provides a lens from which to study the effect of crystallinity on ionic conductivity. For example, it is expected that the 5 kg/mol sample will have too high a concentration of crystallites which will impede ionic motion. It is currently unknown if significant ionic conduction can occur in crystallites, even though ion uptake in crystallites has been observed. Exploring the evolution of ionic conductivity with increasing crystallinity will bring clarity to this issue. By testing ionic and electronic conduction while increasing the polymer molecular weight, a better understanding of the co-evolution of the two properties will be established, and better design rules for MIECs generated.

5.3 Higher Planarity Polymer Backbones for MIECs

A long-term goal is to expand the knowledge we've gained from these initial studies to other conjugated polymer backbones. For electronic conduction, when we moved from polythiophene as a base system to more rigid polymers, like donor/acceptor copolymers, we gained a broader and deeper understanding of the electronic conduction behavior in polymers. This has revolutionized our understanding of the processes occurring at the molecular level, helping to identify true underlying properties that are necessary for charge conduction in all conjugated polymers, rather than just those specific to polythiophene-based systems. By broadening the range of backbones from which we produce MIECs, we can also broaden our knowledge of the fundamental properties underpinning MIEC performance. These types of highly rigid polymers also have another fundamental advantage: planarity. Polymers with high molecular weights and high degrees of planarity have demonstrated extremely high charge mobility. Some examples of these highly planar polymers can have these high charge mobilities while also maintaining low degrees of crystallinity, which seems to offer the ideal set of conditions for high transconductance MIECs.[36] To access a high planarity polymer with ionically conducting groups, we propose targeting a diketopyrrolopyrrole-based polymer, as shown in Figure 5.2.[134]

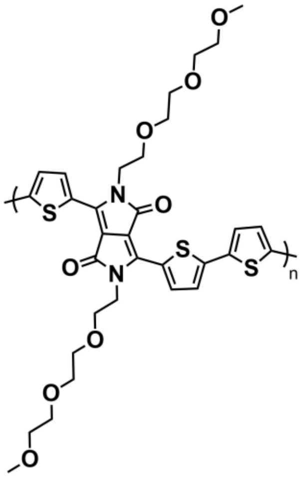

Figure 5.2: Suggested oligoethylene glycol substituted DPP polymer.

5.4 Polythiophene-based MIECs with Non-Oligoethylene Glycol Side Chains

Currently, our group's research work has focused exclusively on investigating variations on using an oligoethylene glycol side chain to introduce ionic conductivity to polythiophenes. Introducing other atoms into the side chain, such as nitrogen or sulfur, could introduce significant improvements to device performance by changing the energy of interaction between the side chain and an individual atom, potentially reducing ion-trapping behavior. Further, it could be possible to introduce ion-specific responses to improve selectivity of MIEC devices by changing these heteroatoms.

Several novel different side chain architectures that are compatible with Grignard formation and allow KCTP polymerization methods to be used are suggested in Figure 5.3. These architectures focus on nitrogen and sulfur incorporation into the side chain, as both heteroatoms characteristically demonstrate a weaker association with lithium ions as compared to oxygen, potentially reducing the kinetic traps for ion transport.[220] Some potential monomer structures are shown in Figure 5.3, all of which could be synthesized from commercially available reagents in 1 or 2 step reactions from 2,5-dibromo-3-thiophene methyl bromide. All targeted structures maintain a 9-atom length side chain, as our previous results show that reducing the number of coordinating groups along the side chain to less than 3 atoms results in a significant reduction in LiTFSI solubility.

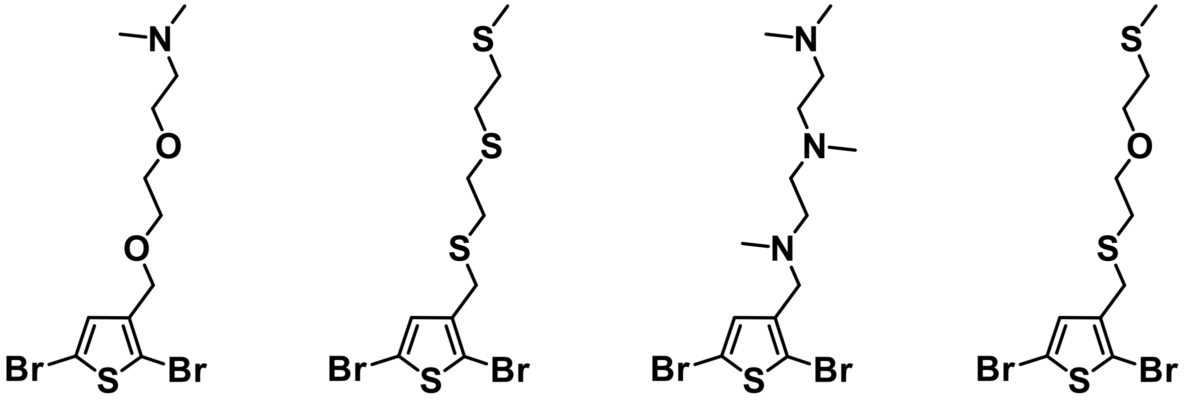

Figure 5.3: Proposed structures for variable heteroatom incorporation for polythiophene-based MIECs.

The first structure represents just a small change from P3MEEMT, exchanging the terminal methoxy group for a terminal dimethylamine group. This exchange will allow us to lean on some of the understanding garnered from studies of P3MEEMT, but also to begin to study the influence of exchanging heteroatoms. The second and third structures represent outright substitutions of oxygen atoms from the P3MEEMT structure for sulfur and nitrogen, respectively. The effects caused by the need for methyl substitution on the ability of the nitrogen atoms to adequately coordinate the highly polar ions could result in a significant reduction in the ion-coordination strength, and thus solubility of ions in the third structure. To investigate the effects of the presence of tertiary as compared to secondary amines, it would be possible to instead protect the nitrogen centers during the polymerization step, removing the protecting groups post-polymerization to produce secondary amines. The fourth structure represents a blending of the P3MEEMT architecture with the second structure, exploring the mixed substitution like the first proposed structure. Overall, these would expand the generality of side chains available for use in homopolymer MIECs, and represent an initial exploration into side chain substitutions that have a structure other than fully oxygenated side chains.

Appendix A: References

1. Zachara, J. E. *et al.* Miniaturised all-solid-state potentiometric ion sensors based on PVC-membranes containing conducting polymers. *Sens. Actuators B Chem.* **101**, 207–212 (2004).
2. Michalska, A. J., Appaih-Kusi, C., Heng, L. Y., Walkiewicz, S. & Hall, E. A. H. An Experimental Study of Membrane Materials and Inner Contacting Layers for Ion-Selective K+ Electrodes with a Stable Response and Good Dynamic Range. *Anal. Chem.* **76**, 2031–2039 (2004).
3. Bay, L., West, K., Sommer-Larsen, P., Skaarup, S. & Benslimane, M. A Conducting Polymer Artificial Muscle with 12 % Linear Strain. *Adv. Mater.* **15**, 310–313 (2003).
4. Stoyanov, H., Kollosche, M., Risse, S., Waché, R. & Kofod, G. Soft Conductive Elastomer Materials for Stretchable Electronics and Voltage Controlled Artificial Muscles. *Adv. Mater.* **25**, 578–583 (2013).
5. Fu, Y. & Manthiram, A. Enhanced Cyclability of Lithium–Sulfur Batteries by a Polymer Acid-Doped Polypyrrole Mixed Ionic–Electronic Conductor. *Chem. Mater.* **24**, 3081–3087 (2012).
6. Wu, H. *et al.* Stable Li-ion battery anodes by *in-situ* polymerization of conducting hydrogel to conformally coat silicon nanoparticles. *Nat. Commun.* **4**, 1943 (2013).
7. Murthy, A. & Manthiram, A. Highly water-dispersible, mixed ionic–electronic conducting, polymer acid-doped polyanilines as ionomers for direct methanol fuel cells. *Chem. Commun.* **47**, 6882–6884 (2011).
8. Khodagholy, D. *et al.* High transconductance organic electrochemical transistors. *Nat. Commun.* **4**, 2133 (2013).

9. Inal, S. *et al.* A High Transconductance Accumulation Mode Electrochemical Transistor. *Adv. Mater.* **26**, 7450–7455.

10. Wang, S., Yan, M., Li, Y., Vinado, C. & Yang, J. Separating electronic and ionic conductivity in mix-conducting layered lithium transition-metal oxides. *J. Power Sources* **393**, 75–82 (2018).

11. Wang, S. *et al.* Electrochemical performance of mixed ionic–electronic conducting oxides as anodes for solid oxide fuel cell. *Solid State Ion.* **120**, 75–84 (1999).

12. Zeglio, E. *et al.* Conjugated Polyelectrolyte Blends for Highly Stable Accumulation-Mode Electrochemical Transistors. *Chem. Mater.* **29**, 4293–4300 (2017).

13. Lin, P., Yan, F., Yu, J., Chan, H. L. W. & Yang, M. The Application of Organic Electrochemical Transistors in Cell-Based Biosensors. *Adv. Mater.* **22**, 3655–3660 (2010).

14. Andersson, P. *et al.* Active Matrix Displays Based on All-Organic Electrochemical Smart Pixels Printed on Paper. *Adv. Mater.* **14**, 1460–1464 (2002).

15. Patel, S. N., Javier, A. E., Stone, G. M., Mullin, S. A. & Balsara, N. P. Simultaneous Conduction of Electronic Charge and Lithium Ions in Block Copolymers. *ACS Nano* **6**, 1589–1600 (2012).

16. Javier, A. E., Patel, S. N., Hallinan, D. T., Srinivasan, V. & Balsara, N. P. Simultaneous Electronic and Ionic Conduction in a Block Copolymer: Application in Lithium Battery Electrodes. *Angew. Chem. Int. Ed.* **50**, 9848–9851 (2011).

17. Deslouis, C., El Moustafid, T., Musiani, M. M. & Tribollet, B. Mixed ionic-electronic conduction of a conducting polymer film. Ac impedance study of polypyrrole. *Electrochimica Acta* **41**, 1343–1349 (1996).

18. Malik, S. & Nandi, A. K. Crystallization mechanism of regioregular poly(3-alkyl thiophene)s. *J. Polym. Sci. Part B Polym. Phys.* **40**, 2073–2085 (2002).
19. Ajayaghosh, A. Donor–acceptor type low band gap polymers : polysquaraines and related systems. *Chem. Soc. Rev.* **32**, 181–191 (2003).
20. Holliday, S., Donaghey, J. E. & McCulloch, I. Advances in Charge Carrier Mobilities of Semiconducting Polymers Used in Organic Transistors. *Chem. Mater.* **26**, 647–663 (2014).
21. Cho, S. *et al.* Thermal annealing-induced enhancement of the field-effect mobility of regioregular poly(3-hexylthiophene) films. *J. Appl. Phys.* **100**, 114503 (2006).
22. Chang, J.-F., Sirringhaus, H., Giles, M., Heeney, M. & McCulloch, I. Relative importance of polaron activation and disorder on charge transport in high-mobility conjugated polymer field-effect transistors. *Phys. Rev. B* **76**, 205204 (2007).
23. Chew, A. R. *et al.* Unraveling the Effect of Conformational and Electronic Disorder in the Charge Transport Processes of Semiconducting Polymers. *Adv. Funct. Mater.* **28**, 1804142 (2018).
24. Kaichen Gu *et al.* Assessing the Huang-Brown Description of Tie Chains for Charge Transport in Conjugated Polymers. *ACS Macro Lett.* doi:10.1021/acsmacrolett.8b00626.
25. Kaneto, K., Y. Lim, W., Takashima, W., Endo, T. & Rikukawa, M. Alkyl Chain Length Dependence of Field-Effect Mobilities in Regioregular Poly(3-Alkylthiophene) Films. *Jpn. J. Appl. Phys.* **39**, L872 (2000).
26. Savagatrup, S. *et al.* Viability of stretchable poly(3-heptylthiophene) (P3HpT) for organic solar cells and field-effect transistors. *Synth. Met.* **203**, 208–214 (2015).
27. Ho, V., Boudouris, B. W. & Segalman, R. A. Tuning Polythiophene Crystallization through Systematic Side Chain Functionalization. *Macromolecules* **43**, 7895–7899 (2010).

28. McCulloch, I. *et al.* Liquid-crystalline semiconducting polymers with high charge-carrier mobility. *Nat. Mater.* **5**, 328–333 (2006).

29. Lim, D.-H. *et al.* A systematic study on molecular planarity and D–A conformation in thiazolothiazole- and thienylenevinylene-based copolymers for organic field-effect transistors. *J. Mater. Chem. C* **5**, 10126–10132 (2017).

30. Li, Y., Tatum, W. K., Onorato, J. W., Zhang, Y. & Luscombe, C. K. Low Elastic Modulus and High Charge Mobility of Low-Crystallinity Indacenodithiophene-Based Semiconducting Polymers for Potential Applications in Stretchable Electronics. *Macromolecules* **51**, 6352–6358 (2018).

31. Li, Y. *et al.* An indacenodithiophene-based semiconducting polymer with high ductility for stretchable organic electronics. *Polym. Chem.* **8**, 5185–5193 (2017).

32. Salleo, A., Chabinyc, M. L., Yang, M. S. & Street, R. A. Polymer thin-film transistors with chemically modified dielectric interfaces. *Appl. Phys. Lett.* **81**, 4383–4385 (2002).

33. Kline, R. J., McGehee, M. D. & Toney, M. F. Highly oriented crystals at the buried interface in polythiophene thin-film transistors. *Nat. Mater.* **5**, 222–228 (2006).

34. Kim, J.-S. *et al.* Tuning Mechanical and Optoelectrical Properties of Poly(3-hexylthiophene) through Systematic Regioregularity Control. *Macromolecules* **48**, 4339–4346 (2015).

35. Mauer, R., Kastler, M. & Laquai, F. The Impact of Polymer Regioregularity on Charge Transport and Efficiency of P3HT:PCBM Photovoltaic Devices. *Adv. Funct. Mater.* **20**, 2085–2092 (2010).

36. Noriega, R. *et al.* A general relationship between disorder, aggregation and charge transport in conjugated polymers. *Nat. Mater.* **12**, 1038–1044 (2013).

37. Burmakin, E. I. & Shekhtman, G. Sh. Mechanism of ionic transport in cesium-conducting solid electrolytes based on cesium orthophosphate. *Russ. J. Electrochem.* **52**, 796–800 (2016).

38. Xue, Z., He, D. & Xie, X. Poly(ethylene oxide)-based electrolytes for lithium-ion batteries. *J. Mater. Chem. A* **3**, 19218–19253 (2015).

39. Golodnitsky, D., Strauss, E., Peled, E. & Greenbaum, S. Review—On Order and Disorder in Polymer Electrolytes. *J. Electrochem. Soc.* **162**, A2551–A2566 (2015).

40. Aziz, S. B., Woo, T. J., Kadir, M. F. Z. & Ahmed, H. M. A conceptual review on polymer electrolytes and ion transport models. *J. Sci. Adv. Mater. Devices* **3**, 1–17 (2018).

41. Cheng, S., Smith, D. M. & Li, C. Y. How Does Nanoscale Crystalline Structure Affect Ion Transport in Solid Polymer Electrolytes? *Macromolecules* **47**, 3978–3986 (2014).

42. Siva Kumar, J., Subrahmanyam, A. R., Jaipal Reddy, M. & Subba Rao, U. V. Preparation and study of properties of polymer electrolyte system (PEO+NaClO3). *Mater. Lett.* **60**, 3346–3349 (2006).

43. Watanabe, M., Nagano, S., Sanui, K. & Ogata, N. Ion conduction mechanism in network polymers from poly(ethylene oxide) and poly(propylene oxide) containing lithium perchlorate. *Solid State Ion.* **18–19**, 338–342 (1986).

44. Albinsson, I., Mellander, B. -E. & Stevens, J. R. Ionic conductivity in poly(propylene glycol) complexed with lithium and sodium triflate. *J. Chem. Phys.* **96**, 681–690 (1992).

45. Walker, C. W. & Salomon, M. Improvement of Ionic Conductivity in Plasticized PEO-Based Solid Polymer Electrolytes. *J. Electrochem. Soc.* **140**, 3409–3412 (1993).

46. Das, S. & Ghosh, A. Effect of plasticizers on ionic conductivity and dielectric relaxation of PEO-LiClO4 polymer electrolyte. *Electrochimica Acta* **171**, 59–65 (2015).

47. Wei, Z. *et al.* Superior lithium ion conduction of polymer electrolyte with comb-like structure via solvent-free copolymerization for bipolar all-solid-state lithium battery. *J. Mater. Chem. A* **6**, 13438–13447 (2018).

48. Qi, L., Lin, Y., Jing, X. & Wang, F. Study of the conductivity and side chain mobility of a comb-like polymer electrolyte using the dynamic mechanical method. *Solid State Ion.* **139**, 293–301 (2001).

49. Gao, Y., Hu, B., Yao, Y. & Chen, Q. Segmental Dynamics of PEO/LiClO4 Complex Crystals and Their Influence on the Li+-Ion Transportation in Crystal Lattices: A 13C Solid-State NMR Approach. *Chem. – Eur. J.* **17**, 8941–8946 (2011).

50. Giridharagopal, R. *et al.* Electrochemical strain microscopy probes morphology-induced variations in ion uptake and performance in organic electrochemical transistors. *Nat. Mater.* **16**, 737–742 (2017).

51. Ghosh, R. *et al.* Spectral Signatures and Spatial Coherence of Bound and Unbound Polarons in P3HT Films: Theory Versus Experiment. *J. Phys. Chem. C* **122**, 18048–18060 (2018).

52. Rivnay, J. *et al.* Structural control of mixed ionic and electronic transport in conducting polymers. *Nat. Commun.* **7**, 11287 (2016).

53. Kim, N. *et al.* Highly Conductive PEDOT:PSS Nanofibrils Induced by Solution-Processed Crystallization. *Adv. Mater.* **26**, 2268–2272 (2014).

54. Takano, T., Masunaga, H., Fujiwara, A., Okuzaki, H. & Sasaki, T. PEDOT Nanocrystal in Highly Conductive PEDOT:PSS Polymer Films. *Macromolecules* **45**, 3859–3865 (2012).

55. Nardes, A. M. *et al.* Microscopic Understanding of the Anisotropic Conductivity of PEDOT:PSS Thin Films. *Adv. Mater.* **19**, 1196–1200 (2007).

56. Xia, Y. & Ouyang, J. PEDOT:PSS films with significantly enhanced conductivities induced by preferential solvation with cosolvents and their application in polymer photovoltaic cells. *J. Mater. Chem.* **21**, 4927–4936 (2011).

57. Kim, J. Y., Jung, J. H., Lee, D. E. & Joo, J. Enhancement of electrical conductivity of poly(3,4-ethylenedioxythiophene)/poly(4-styrenesulfonate) by a change of solvents. *Synth. Met.* **126**, 311–316 (2002).

58. Ashizawa, S., Horikawa, R. & Okuzaki, H. Effects of solvent on carrier transport in poly(3,4-ethylenedioxythiophene)/poly(4-styrenesulfonate). *Synth. Met.* **153**, 5–8 (2005).

59. Kim, Y. H. *et al.* Highly Conductive PEDOT:PSS Electrode with Optimized Solvent and Thermal Post-Treatment for ITO-Free Organic Solar Cells. *Adv. Funct. Mater.* **21**, 1076–1081 (2011).

60. Jönsson, S. K. M. *et al.* The effects of solvents on the morphology and sheet resistance in poly(3,4-ethylenedioxythiophene)–polystyrenesulfonic acid (PEDOT–PSS) films. *Synth. Met.* **139**, 1–10 (2003).

61. Nardes, A. M., Janssen, R. A. J. & Kemerink, M. A Morphological Model for the Solvent-Enhanced Conductivity of PEDOT:PSS Thin Films. *Adv. Funct. Mater.* **18**, 865–871 (2008).

62. Veder, J.-P. *et al.* An Electrochemical Impedance Spectroscopy/Neutron Reflectometry Study of Water Uptake in the Poly(3,4-Ethylenedioxythiophene):Poly(Styrene Sulfonate)/Polymethyl Methacrylate-Polydecyl Methacrylate Copolymer Solid-Contact Ion-Selective Electrode. *Electroanalysis* **24**, 140–145 (2012).

63. Nardes, A. M. *et al.* Conductivity, work function, and environmental stability of PEDOT:PSS thin films treated with sorbitol. *Org. Electron.* **9**, 727–734 (2008).

64. Döbbelin, M. *et al.* Influence of Ionic Liquids on the Electrical Conductivity and Morphology of PEDOT:PSS Films. *Chem. Mater.* **19**, 2147–2149 (2007).
65. Murphy, R. J. *et al.* Scattering Studies on Poly(3,4-ethylenedioxythiophene)–Polystyrenesulfonate in the Presence of Ionic Liquids. *Macromolecules* **48**, 8989–8997 (2015).
66. Stavrinidou, E. *et al.* Direct Measurement of Ion Mobility in a Conducting Polymer. *Adv. Mater.* **25**, 4488–4493 (2013).
67. Håkansson, A. *et al.* Effect of (3-glycidyloxypropyl)trimethoxysilane (GOPS) on the electrical properties of PEDOT:PSS films. *J. Polym. Sci. Part B Polym. Phys.* **55**, 814–820 (2017).
68. Kim, S.-M. *et al.* Influence of PEDOT:PSS crystallinity and composition on electrochemical transistor performance and long-term stability. *Nat. Commun.* **9**, 3858 (2018).
69. Giovannitti, A. *et al.* Controlling the mode of operation of organic transistors through side-chain engineering. *Proc. Natl. Acad. Sci.* **113**, 12017–12022 (2016).
70. Giovannitti, A. *et al.* N-type organic electrochemical transistors with stability in water. *Nat. Commun.* **7**, 13066 (2016).
71. Onorato, J. W. & Luscombe, C. K. Morphological effects on polymeric mixed ionic/electronic conductors. *Mol. Syst. Des. Eng.* **4**, 310–324 (2019).
72. Elschner, A. & Lövenich, W. Solution-deposited PEDOT for transparent conductive applications. *MRS Bull.* **36**, 794–798 (2011).
73. Rivnay, J. *et al.* High-performance transistors for bioelectronics through tuning of channel thickness. *Sci. Adv.* **1**, e1400251 (2015).

74. Tybrandt, K., Forchheimer, R. & Berggren, M. Logic gates based on ion transistors. *Nat. Commun.* **3**, 871 (2012).

75. NG, S. C., CHAN, H. S. O. & YU, W.-L. Synthesis and characterization of electrically conducting copolymers of ethylenedioxythiophene and 1,3-propylenedioxythiophene with ω-functional substituents. *J. Mater. Sci. Lett.* **16**, 809–811 (1997).

76. Wang, C., Schindler, J. L., Kannewurf, C. R. & Kanatzidis, M. G. Poly(3,4-ethylenedithiathiophene). A New Soluble Conductive Polythiophene Derivative. *Chem. Mater.* **7**, 58–68 (1995).

77. Jonas, F., Krafft, W. & Muys, B. Poly(3, 4-ethylenedioxythiophene): Conductive coatings, technical applications and properties. *Macromol. Symp.* **100**, 169–173 (1995).

78. Bernards, D. A. & Malliaras, G. G. Steady-State and Transient Behavior of Organic Electrochemical Transistors. *Adv. Funct. Mater.* **17**, 3538–3544 (2007).

79. Elschner, A., Kirchmeyer, S., Lovenich, W., Merker, U. & Reuter, K. *PEDOT: Principles and Applications of an Intrinsically Conductive Polymer*. (CRC Press, 2010).

80. Lang, U., Müller, E., Naujoks, N. & Dual, J. Microscopical Investigations of PEDOT:PSS Thin Films. *Adv. Funct. Mater.* **19**, 1215–1220 (2009).

81. Zhang, S. *et al.* Solvent-induced changes in PEDOT:PSS films for organic electrochemical transistors. *APL Mater.* **3**, 014911 (2014).

82. Huang, J. *et al.* Investigation of the Effects of Doping and Post-Deposition Treatments on the Conductivity, Morphology, and Work Function of Poly(3,4-ethylenedioxythiophene)/Poly(styrene sulfonate) Films. *Adv. Funct. Mater.* **15**, 290–296 (2005).

83. Mengistie, D. A., Wang, P.-C. & Chu, C.-W. Effect of molecular weight of additives on the conductivity of PEDOT:PSS and efficiency for ITO-free organic solar cells. *J. Mater. Chem. A* **1**, 9907–9915 (2013).

84. Palumbiny, C. M. *et al.* Molecular Reorientation and Structural Changes in Cosolvent-Treated Highly Conductive PEDOT:PSS Electrodes for Flexible Indium Tin Oxide-Free Organic Electronics. *J. Phys. Chem. C* **118**, 13598–13606 (2014).

85. Ouyang, J., Chu, C.-W., Chen, F.-C., Xu, Q. & Yang, Y. High-Conductivity Poly(3,4-ethylenedioxythiophene):Poly(styrene sulfonate) Film and Its Application in Polymer Optoelectronic Devices. *Adv. Funct. Mater.* **15**, 203–208 (2005).

86. Ouyang, J. *et al.* On the mechanism of conductivity enhancement in poly(3,4-ethylenedioxythiophene):poly(styrene sulfonate) film through solvent treatment. *Polymer* **45**, 8443–8450 (2004).

87. Xia, Y., Sun, K. & Ouyang, J. Solution-Processed Metallic Conducting Polymer Films as Transparent Electrode of Optoelectronic Devices. *Adv. Mater.* **24**, 2436–2440 (2012).

88. Meng, W. *et al.* Conductivity Enhancement of PEDOT:PSS Films via Phosphoric Acid Treatment for Flexible All-Plastic Solar Cells. *ACS Appl. Mater. Interfaces* **7**, 14089–14094 (2015).

89. Mengistie, D. A., Ibrahem, M. A., Wang, P.-C. & Chu, C.-W. Highly Conductive PEDOT:PSS Treated with Formic Acid for ITO-Free Polymer Solar Cells. *ACS Appl. Mater. Interfaces* **6**, 2292–2299 (2014).

90. Xia, Y. & Ouyang, J. Significant Conductivity Enhancement of Conductive Poly(3,4-ethylenedioxythiophene): Poly(styrenesulfonate) Films through a Treatment with Organic Carboxylic Acids and Inorganic Acids. *ACS Appl. Mater. Interfaces* **2**, 474–483 (2010).

91. Sarker, A. K. *et al.* Hydroiodic acid treated PEDOT:PSS thin film as transparent electrode: an approach towards ITO free organic photovoltaics. *RSC Adv.* **5**, 52019–52025 (2015).
92. Derue, L. *et al.* Thermal Stabilisation of Polymer–Fullerene Bulk Heterojunction Morphology for Efficient Photovoltaic Solar Cells. *Adv. Mater.* **26**, 5831–5838 (2014).
93. Berezhetska, O., Liberelle, B., Crescenzo, G. D. & Cicoira, F. A simple approach for protein covalent grafting on conducting polymer films. *J. Mater. Chem. B* **3**, 5087–5094 (2015).
94. Khodagholy, D. *et al.* Highly Conformable Conducting Polymer Electrodes for In Vivo Recordings. *Adv. Mater.* **23**, H268–H272 (2011).
95. Wong, A. K. Y. & Krull, U. J. Surface characterization of 3-glycidoxypropyltrimethoxysilane films on silicon-based substrates. *Anal. Bioanal. Chem.* **383**, 187–200 (2005).
96. Kergoat, L. *et al.* Detection of Glutamate and Acetylcholine with Organic Electrochemical Transistors Based on Conducting Polymer/Platinum Nanoparticle Composites. *Adv. Mater.* **26**, 5658–5664 (2014).
97. Colucci, R. *et al.* Cross-linked PEDOT: PSS as an alternative for low-cost solution-processed electronic devices. *Synth. Met.* **241**, 47–53 (2018).
98. ElMahmoudy, M. *et al.* Tailoring the Electrochemical and Mechanical Properties of PEDOT:PSS Films for Bioelectronics. *Macromol. Mater. Eng.* **302**, 1600497 (2017).
99. Mantione, D. *et al.* Low-Temperature Cross-Linking of PEDOT:PSS Films Using Divinylsulfone. *ACS Appl. Mater. Interfaces* **9**, 18254–18262 (2017).
100. Agua, I. del *et al.* DVS-Crosslinked PEDOT:PSS Free-Standing and Textile Electrodes toward Wearable Health Monitoring. *Adv. Mater. Technol.* **3**, 1700322 (2018).
101. Yan, L. *et al.* Ionically cross-linked PEDOT:PSS as a multi-functional conductive binder for high-performance lithium–sulfur batteries. *Sustain. Energy Fuels* **2**, 1574–1581 (2018).

102. Harman, D. G. *et al.* Poly(3,4-ethylenedioxythiophene):dextran sulfate (PEDOT:DS) – A highly processable conductive organic biopolymer. *Acta Biomater.* **14**, 33–42 (2015).

103. Zhang, Y., Chen, L., Hu, X., Zhang, L. & Chen, Y. Low Work-function Poly(3,4-ethylenedioxylenethiophene): Poly(styrene sulfonate) as Electron-transport Layer for High-efficient and Stable Polymer Solar Cells. *Sci. Rep.* **5**, 12839 (2015).

104. Inal, S. *et al.* Organic electrochemical transistors based on PEDOT with different anionic polyelectrolyte dopants. *J. Polym. Sci. Part B Polym. Phys.* **54**, 147–151 (2016).

105. Hofmann, A. I. *et al.* An Alternative Anionic Polyelectrolyte for Aqueous PEDOT Dispersions: Toward Printable Transparent Electrodes. *Angew. Chem. Int. Ed.* **54**, 8506–8510 (2015).

106. McDonald, M. B. & Hammond, P. T. Efficient Transport Networks in a Dual Electron/Lithium-Conducting Polymeric Composite for Electrochemical Applications. *ACS Appl. Mater. Interfaces* **10**, 15681–15690 (2018).

107. Ghosh, S. & Inganäs, O. Networks of Electron-Conducting Polymer in Matrices of Ion-Conducting Polymers Applications to Fast Electrodes. *Electrochem. Solid-State Lett.* **3**, 213–215 (2000).

108. Li, P., Sun, K. & Ouyang, J. Stretchable and Conductive Polymer Films Prepared by Solution Blending. *ACS Appl. Mater. Interfaces* **7**, 18415–18423 (2015).

109. Cao, Y., Yu, G., Heeger, A. J. & Yang, C. Y. Efficient, fast response light-emitting electrochemical cells: Electroluminescent and solid electrolyte polymers with interpenetrating network morphology. *Appl. Phys. Lett.* **68**, 3218–3220 (1996).

110. Chen, F.-C., Xu, Q. & Yang, Y. Enhanced efficiency of plastic photovoltaic devices by blending with ionic solid electrolytes. *Appl. Phys. Lett.* **84**, 3181–3183 (2004).

111. Wenzl, F. P. *et al.* Microstructure tailoring of conjugated polymer-electrolyte blends for light-emitting electrochemical cells. *Solid State Ion.* **176**, 1747–1751 (2005).

112. Cao, Y., Pei, Q., Andersson, M. R., Yu, G. & Heeger, A. J. Light-Emitting Electrochemical Cells with Crown Ether as Solid Electrolyte. *J. Electrochem. Soc.* **144**, L317–L320 (1997).

113. Friedlein, J. T. *et al.* Influence of disorder on transfer characteristics of organic electrochemical transistors. *Appl. Phys. Lett.* **111**, 023301 (2017).

114. Song, I. Y., Kim, J., Im, M. J., Moon, B. J. & Park, T. Synthesis and Self-Assembly of Thiophene-Based All-Conjugated Amphiphilic Diblock Copolymers with a Narrow Molecular Weight Distribution. *Macromolecules* **45**, 5058–5068 (2012).

115. Craley, C. R., Zhang, R., Kowalewski, T., McCullough, R. D. & Stefan, M. C. Regioregular Poly(3-hexylthiophene) in a Novel Conducting Amphiphilic Block Copolymer. *Macromol. Rapid Commun.* **30**, 11–16 (2009).

116. Liu, J., Sheina, E., Kowalewski, T. & McCullough, R. D. Tuning the Electrical Conductivity and Self-Assembly of Regioregular Polythiophene by Block Copolymerization: Nanowire Morphologies in New Di- and Triblock Copolymers. *Angew. Chem. Int. Ed.* **41**, 329–332 (2002).

117. Thelen, J. L. *et al.* Phase Behavior of a Block Copolymer/Salt Mixture through the Order-to-Disorder Transition. *Macromolecules* **47**, 2666–2673 (2014).

118. Nakamura, I., Balsara, N. P. & Wang, Z.-G. First-Order Disordered-to-Lamellar Phase Transition in Lithium Salt-Doped Block Copolymers. *ACS Macro Lett.* **2**, 478–481 (2013).

119. Patel, S. N., Javier, A. E. & Balsara, N. P. Electrochemically Oxidized Electronic and Ionic Conducting Nanostructured Block Copolymers for Lithium Battery Electrodes. *ACS Nano* **7**, 6056–6068 (2013).

120. Bhatt, M. P., Thelen, J. L. & Balsara, N. P. Effect of Copolymer Composition on Electronic Conductivity of Electrochemically Oxidized Poly(3-hexylthiophene)-b-poly(ethylene oxide) Block Copolymers. *Chem. Mater.* **27**, 5141–5148 (2015).

121. Wang, H. *et al.* Syntheses of Amphiphilic Diblock Copolymers Containing a Conjugated Block and Their Self-Assembling Properties. *J. Am. Chem. Soc.* **122**, 6855–6861 (2000).

122. Huang, W. Y. *et al.* Organization and Orientation of a Triblock Copolymer Poly(ethylene glycol)-b-poly(p-phenylene ethynylene)-b-poly(ethylene glycol) and Its Blends in Thin Films. *Macromolecules* **34**, 7809–7816 (2001).

123. Im, M. J., Moon, B. J., Lee, G.-Y., Son, S. Y. & Park, T. Positioning lithium ions by host–guest chemistry combined with self-assembly using a thiophene-based all-conjugated amphiphilic block copolymer. *J. Polym. Sci. Part Polym. Chem.* **52**, 1068–1074 (2014).

124. Thackeray, J. W., White, H. S. & Wrighton, M. S. Poly(3-methylthiophene)-coated electrodes: optical and electrical properties as a function of redox potential and amplification of electrical and chemical signals using poly(3-methylthiophene)-based microelectrochemical transistors. *J. Phys. Chem.* **89**, 5133–5140 (1985).

125. Rani, V. & Santhanam, K. S. V. Polycarbazole-based electrochemical transistor. *J. Solid State Electrochem.* **2**, 99–101 (1998).

126. Ofer, D., Park, L. Y., Schrock, R. R. & Wrighton, M. S. Potential dependence of the conductivity of polyacetylene: finite potential windows of high conductivity. *Chem. Mater.* **3**, 573–575 (1991).

127. Ofer, D., Crooks, R. M. & Wrighton, M. S. Potential dependence of the conductivity of highly oxidized polythiophenes, polypyrroles, and polyaniline: finite windows of high conductivity. *J. Am. Chem. Soc.* **112**, 7869–7879 (1990).

128. Paul, E. W., Ricco, A. J. & Wrighton, M. S. Resistance of polyaniline films as a function of electrochemical potential and the fabrication of polyaniline-based microelectronic devices. *J. Phys. Chem.* **89**, 1441–1447 (1985).
129. White, H. S., Kittlesen, G. P. & Wrighton, M. S. Chemical derivatization of an array of three gold microelectrodes with polypyrrole: fabrication of a molecule-based transistor. *J. Am. Chem. Soc.* **106**, 5375–5377 (1984).
130. Nishizawa, Matsuhiko., Matsue, Tomokazu. & Uchida, Isamu. Penicillin sensor based on a microarray electrode coated with pH-responsive polypyrrole. *Anal. Chem.* **64**, 2642–2644 (1992).
131. Stejskal, J. *et al.* Mixed electron and proton conductivity of polyaniline films in aqueous solutions of acids: beyond the 1000 S cm−1 limit. *Polym. Int.* **58**, 872–879 (2009).
132. Minett, M. G. & Owen, J. R. Polymeric insertion electrodes. *Solid State Ion.* **28–30**, 1192–1196 (1988).
133. Tarver, J., Yoo, J. E., Dennes, T. J., Schwartz, J. & Loo, Y.-L. Polymer Acid Doped Polyaniline Is Electrochemically Stable Beyond pH 9. *Chem. Mater.* **21**, 280–286 (2009).
134. Sugiyama, F. *et al.* Effects of flexibility and branching of side chains on the mechanical properties of low-bandgap conjugated polymers. *Polym. Chem.* **9**, 4354–4363 (2018).
135. Meng, B. *et al.* Replacing Alkyl with Oligo(ethylene glycol) as Side Chains of Conjugated Polymers for Close π–π Stacking. *Macromolecules* **48**, 4357–4363 (2015).
136. Sheina, E. E., Khersonsky, S. M., Jones, E. G. & McCullough, R. D. Highly Conductive, Regioregular Alkoxy-Functionalized Polythiophenes: A New Class of Stable, Low Band Gap Materials. *Chem. Mater.* **17**, 3317–3319 (2005).

137. Nielsen, C. B. *et al.* Molecular Design of Semiconducting Polymers for High-Performance Organic Electrochemical Transistors. *J. Am. Chem. Soc.* **138**, 10252–10259 (2016).

138. Liao, Y. *et al.* Sulfonated Polyaniline Nanostructures Synthesized via Rapid Initiated Copolymerization with Controllable Morphology, Size, and Electrical Properties. *Macromolecules* **45**, 1570–1579 (2012).

139. Cheng, C. H. W., Lin, F. & Lonergan, M. C. Charge Transport in a Mixed Ionically/Electronically Conducting, Cationic, Polyacetylene Ionomer between Ion-Blocking Electrodes. *J. Phys. Chem. B* **109**, 10168–10178 (2005).

140. Laiho, A., Herlogsson, L., Forchheimer, R., Crispin, X. & Berggren, M. Controlling the dimensionality of charge transport in organic thin-film transistors. *Proc. Natl. Acad. Sci.* **108**, 15069–15073 (2011).

141. Dong, B. X. *et al.* Influence of Side-Chain Chemistry on Structure and Ionic Conduction Characteristics of Polythiophene Derivatives: A Computational and Experimental Study. *Chem. Mater.* **31**, 1418–1429 (2019).

142. Sekitani, T., Zschieschang, U., Klauk, H. & Someya, T. Flexible organic transistors and circuits with extreme bending stability. *Nat. Mater.* **9**, 1015–1022 (2010).

143. Hoth, C. N., Schilinsky, P., Choulis, S. a. & Brabec, C. J. Printing highly efficient organic solar cells. *Nano Lett.* **8**, 2806–2813 (2008).

144. Sirringhaus, H. 25Th Anniversary Article: Organic Field-Effect Transistors: the Path Beyond Amorphous Silicon. *Adv. Mater. Deerfield Beach Fla* **26**, 1319–35 (2014).

145. Dong, H., Fu, X., Liu, J., Wang, Z. & Hu, W. 25th Anniversary Article: Key Points for High-Mobility Organic Field-Effect Transistors. *Adv. Mater.* **25**, 6158–6183 (2013).

146. Borsenberger, P. M. & Weiss, D. S. *Organic Photoreceptors for Xerography*. (CRC Press, 1998).
147. Geffroy, B., le Roy, P. & Prat, C. Organic light-emitting diode (OLED) technology: materials, devices and display technologies. *Polym. Int.* **55**, 572–582 (2006).
148. Müllen, K. & Scherf, U. *Organic Light Emitting Devices: Synthesis, Properties and Applications*. (Wiley, 2006).
149. Günes, S., Neugebauer, H. & Sariciftci, N. S. Conjugated polymer-based organic solar cells. *Chem. Rev.* **107**, 1324–38 (2007).
150. Kroon, R., Lenes, M., Hummelen, J. C., Blom, P. W. M. & de Boer, B. Small Bandgap Polymers for Organic Solar Cells (Polymer Material Development in the Last 5 Years). *Polym. Rev.* **48**, 531–582 (2008).
151. Khodagholy, D. *et al.* In vivo recordings of brain activity using organic transistors. *Nat. Commun.* **4**, (2013).
152. Rivnay, J., Owens, R. M. & Malliaras, G. G. The rise of organic bioelectronics. *Chem. Mater.* **26**, 679–685 (2014).
153. Owens, R. M. & Malliaras, G. G. Organic Electronics at the Interface with Biology. *MRS Bull.* **35**, 449–456 (2010).
154. Lee, K., Povlich, L. K. & Kim, J. Recent advances in fluorescent and colorimetric conjugated polymer-based biosensors. *The Analyst* **135**, 2179–89 (2010).
155. Scherson, D. A. & Palencsár, A. Batteries and Electrochemical Capacitors. *Electrochem. Soc. Interface* **43**, (2006).
156. Delacourt, C. *et al.* Toward Understanding of Electrical Limitations (Electronic, Ionic) in LiMPO[sub 4] (M=Fe, Mn) Electrode Materials. *J. Electrochem. Soc.* **152**, A913 (2005).

157. Liu, T. *et al.* Polyaniline and polypyrrole pseudocapacitor electrodes with excellent cycling stability. *Nano Lett.* **14**, 2522–2527 (2014).

158. Mortimer, R. J., Dyer, A. L. & Reynolds, J. R. Electrochromic organic and polymeric materials for display applications. *Displays* **27**, 2–18 (2006).

159. O'Regan, B. & Gratzel, M. A Low-Cost, High-Efficiency Solar-Cell Based on Dye-Sensitized Colloidal TiO_2 Films. *Nature* **353**, 737–740 (1991).

160. Haines, C. S. *et al.* Artificial muscles from fishing line and sewing thread. *Science* **343**, 868–872 (2014).

161. Inal, S., Rivnay, J., Suiu, A. O., Malliaras, G. G. & McCulloch, I. Conjugated Polymers in Bioelectronics. *Acc. Chem. Res.* **51**, 1368–1376 (2018).

162. Dong, B. X., Huang, B., Tan, A. & Green, P. F. Nanoscale Orientation Effects on Carrier Transport in a Low-Band-Gap Polymer. *J. Phys. Chem. C* **118**, 17490–17498 (2014).

163. Mollinger, S. a., Krajina, B. a., Noriega, R., Salleo, A. & Spakowitz, A. J. Percolation, Tie-Molecules, and the Microstructural Determinants of Charge Transport in Semicrystalline Conjugated Polymers. *ACS Macro Lett.* **4**, 708–712 (2015).

164. Duong, D. T. *et al.* Mechanism of crystallization and implications for charge transport in poly(3-ethylhexylthiophene) thin films. *Adv. Funct. Mater.* **24**, 4515–4521 (2014).

165. Kline, R. J. *et al.* Dependence of Regioregular Poly (3-hexylthiophene) Film Morphology and Field-Effect Mobility on Molecular Weight. *Macromolecules* 3312–3319 (2005).

166. Zhang, X. *et al.* Molecular origin of high field-effect mobility in an indacenodithiophene-benzothiadiazole copolymer. *Nat. Commun.* **4**, 2238 (2013).

167. Inal, S., Malliaras, G. G. & Rivnay, J. Optical study of electrochromic moving fronts for the investigation of ion transport in conducting polymers. *J. Mater. Chem. C* **4**, 3942–3947 (2016).

168. Pipertzis, A., Mühlinghaus, M., Mezger, M., Scherf, U. & Floudas, G. Polymerized Ionic Liquids with Polythiophene Backbones: Self-Assembly, Thermal Properties, and Ion Conduction. *Macromolecules* **51**, 6400–6450 (2018).

169. Jiang, Z. GIXSGUI : a MATLAB toolbox for grazing-incidence X-ray scattering data visualization and reduction, and indexing of buried three-dimensional periodic nanostructured films. *J. Appl. Crystallogr.* **48**, 917–926 (2015).

170. Dong, B. X. *et al.* Crystallization Mechanism and Charge Carrier Transport in MAPLE-Deposited Conjugated Polymer Thin Films. *ACS Appl. Mater. Interfaces* **9**, 44799–44810 (2017).

171. Carlo, A. M., Study, S. & Bassler, H. Charge Transport in Disordered Organic Photoconductors. **15**, (1993).

172. Jimison, L. H. *et al.* Vertical confinement and interface effects on the microstructure and charge transport of P3HT thin films. *J. Polym. Sci. Part B Polym. Phys.* **51**, 611–620 (2013).

173. Himmelberger, S. *et al.* Effects of confinement on microstructure and charge transport in high performance semicrystalline polymer semiconductors. *Adv. Funct. Mater.* **23**, 2091–2098 (2013).

174. Dacuña, J. & Salleo, a. Modeling Space-Charge Limited Currents in Organic Semiconductors : Extracting Trap Density and Mobility I . Introduction. *Phys. Rev. B* **84**, 195209 (2011).

175. Baker, J. L. *et al.* Quantification of thin film crystallographic orientation using X-ray diffraction with an area detector. *Langmuir* **26**, 9146–9151 (2010).

176. DeLongchamp, D. M., Kline, R. J., Fischer, D. a, Richter, L. J. & Toney, M. F. Molecular characterization of organic electronic films. *Adv. Mater. Deerfield Beach Fla* **23**, 319–37 (2011).

177. Kroon, R. *et al.* Polar Side Chains Enhance Processability, Electrical Conductivity, and Thermal Stability of a Molecularly p-Doped Polythiophene. *Adv. Mater.* **29**, 35–37 (2017).

178. Kayunkid, N., Uttiya, S. & Brinkmann, M. Structural model of regioregular poly(3-hexylthiophene) obtained by electron diffraction analysis. *Macromolecules* **43**, 4961–4967 (2010).

179. Nosé, S. A unified formulation of the constant temperature molecular dynamics methods. *J. Chem. Phys.* **81**, 511–519 (1984).

180. To, T. T. & Adams, S. Modelling of P3HT:PCBM interface using coarse-grained forcefield derived from accurate atomistic forcefield. *Phys. Chem. Chem. Phys.* **16**, 4653–4663 (2014).

181. Berthier, C. *et al.* Microscopic investigation of ionic conductivity in alkali metal salts-poly(ethylene oxide) adducts. *Solid Sate Ion.* **11**, 91–95 (1983).

182. Wintersgill, M. C. *et al.* Electrical conductivity, differential scanning calorimetry and nuclear magnetic resonance studies of amorphous poly(ethylene oxide) complexed with sodium salts. *Polymer* **30**, 1123–1126 (1989).

183. Borodin, O. & Smith, G. D. Mechanism of ion transport in amorphous poly(ethylene oxide)/ LiTFSI from molecular dynamics simulations. *Macromolecules* **39**, 1620–1629 (2006).

184. Chang, J.-F. *et al.* Enhanced Mobility of Poly(3-hexylthiophene) Transistors by Spin-Coating from High-Boiling-Point Solvents. *Chem. Mater.* **16**, 4772–4776 (2004).

185. Dong, B. X., Li, A., Strzalka, J., Stein, G. E. & Green, P. F. Molecular organization in MAPLE-deposited conjugated polymer thin films and the implications for carrier transport characteristics. *J. Polym. Sci. Part B Polym. Phys.* **55**, 39–48 (2017).

186. Hammond, M. R. *et al.* Molecular order in high-efficiency polymer/fullerene bulk heterojunction solar cells. *ACS Nano* **5**, 8248–57 (2011).

187. Guardado, J. O. & Salleo, A. Structural Effects of Gating Poly(3-hexylthiophene) through an Ionic Liquid. *Adv. Funct. Mater.* **27**, 1–12 (2017).

188. Thelen, J. L. *et al.* Relationship between Mobility and Lattice Strain in Electrochemically Doped Poly(3-hexylthiophene). *ACS Macro Lett.* **4**, 1386–1391 (2015).

189. Thomas, E. M. *et al.* X-Ray Scattering Reveals Ion-Induced Microstructural Changes During Electrochemical Gating of Poly(3-Hexylthiophene). *Adv. Funct. Mater.* **1803687**, 1803687 (2018).

190. Paul, D. K., Mccreery, R. & Karan, K. Proton Transport Property in Supported Nafion Nanothin Films by Electrochemical Impedance Spectroscopy. *J. Electrochem. Soc.* **161**, 1395–1402 (2014).

191. Arges, C. G., Kambe, Y., Suh, H. S., Ocola, L. E. & Nealey, P. F. Perpendicularly Aligned, Anion Conducting Nanochannels in Block Copolymer Electrolyte Films. *Chem. Mater.* **28**, 1377–1389 (2016).

192. Sharon, D. *et al.* Interrogation of Electrochemical Properties of Polymer Electrolyte Thin Films with Interdigitated Electrodes. *J. Electrochem. Soc.* **165**, H1028–H1039 (2018).

193. Liu, Z. *et al.* Self-Assembly Behavior of An Oligothiophene-Based Conjugated Liquid Crystal and Its Implication for Ionic Conductivity Characteristics. *Adv. Funct. Mater.* **1805220**, 1–12 (2018).

194. Lascaud, S. *et al.* Phase Diagrams and Conductivity Behavior of Poly(ethylene oxide)-Molten Salt Rubbery Electrolytes. *Macromolecules* **27**, 7469–7477 (1994).

195. Lee, E. *et al.* Hierarchical Helical Assembly of Conjugated Poly(3-hexylthiophene)-block-poly(3-triethylene glycol thiophene) Diblock Copolymers. *J. Am. Chem. Soc.* **133**, 10390–10393 (2011).

196. Huang, D. M., Faller, R., Do, K. & Moulé, A. J. Coarse-Grained Computer Simulations of Polymer/Fullerene Bulk Heterojunctions for Organic Photovoltaic Applications. *J. Chem. Theory Comput.* **6**, 526–537 (2010).

197. Jorgensen, W. L., Maxwell, D. S. & Tirado-Rives, J. Development and Testing of the OPLS All-Atom Force Field on Conformational Energetics and Properties of Organic Liquids. *J. Am. Chem. Soc.* **118**, 11225–11236 (1996).

198. Poelking, C. & Andrienko, D. Effect of Polymorphism, Regioregularity and Paracrystallinity on Charge Transport in Poly(3-hexylthiophene) [P3HT] Nanofibers. *Macromolecules* **46**, 8941–8956 (2013).

199. Wheeler, D. R. & Newman, J. Molecular Dynamics Simulations of Multicomponent Diffusion. 1. Equilibrium Method. *J. Phys. Chem. B* **108**, 18353–18361 (2004).

200. Wustoni, S. *et al.* In Situ Electrochemical Synthesis of a Conducting Polymer Composite for Multimetabolite Sensing. *Adv. Mater. Technol.* **5**, 1900943 (2020).

201. Savva, A., Wustoni, S. & Inal, S. Ionic-to-electronic coupling efficiency in PEDOT:PSS films operated in aqueous electrolytes. *J. Mater. Chem. C* **6**, 12023–12030 (2018).

202. Pappa, A. M. *et al.* Direct metabolite detection with an n-type accumulation mode organic electrochemical transistor. *Sci. Adv.* **4**, eaat0911 (2018).

203. Zhao, H., Zhu, B., Sekine, J., Luo, S.-C. & Yu, H. Oligoethylene-Glycol-Functionalized Polyoxythiophenes for Cell Engineering: Syntheses, Characterizations, and Cell Compatibilities. *ACS Appl. Mater. Interfaces* **4**, 680–686 (2012).

204. Kim, B., Un Hwang, J. & Kim, E. Chloride transport in conductive polymer films for an n-type thermoelectric platform. *Energy Environ. Sci.* **13**, 859–867 (2020).

205. Han, P., Chung, S.-H. & Manthiram, A. Designing a high-loading sulfur cathode with a mixed ionic-electronic conducting polymer for electrochemically stable lithium-sulfur batteries. *Energy Storage Mater.* **17**, 317–324 (2019).

206. Keene, S. T. *et al.* A biohybrid synapse with neurotransmitter-mediated plasticity. *Nat. Mater.* 1–5 (2020) doi:10.1038/s41563-020-0703-y.

207. Rivnay, J. *et al.* Organic electrochemical transistors. *Nat. Rev. Mater.* **3**, 1–14 (2018).

208. Savva, A. *et al.* Influence of Water on the Performance of Organic Electrochemical Transistors. *Chem. Mater.* **31**, 927–937 (2019).

209. Thiburce, Q., Giovannitti, A., McCulloch, I. & Campbell, A. J. Nanoscale Ion-Doped Polymer Transistors. *Nano Lett.* **19**, 1712–1718 (2019).

210. Giovannitti, A. *et al.* The Role of the Side Chain on the Performance of N-type Conjugated Polymers in Aqueous Electrolytes. *Chem. Mater.* **30**, 2945–2953 (2018).

211. Schmode, P. *et al.* The Key Role of Side Chain Linkage in Structure Formation and Mixed Conduction of Ethylene Glycol Substituted Polythiophenes. *ACS Appl. Mater. Interfaces* **12**, 13029–13039 (2020).

212. Nečas, D. & Klapetek, P. Gwyddion: an open-source software for SPM data analysis. *Cent. Eur. J. Phys.* **10**, 181–188 (2012).

213. Farouil, L., Alary, F., Bedel-Pereira, E. & Heully, J.-L. Revisiting the Vibrational and Optical Properties of P3HT: A Combined Experimental and Theoretical Study. *J. Phys. Chem. A* **122**, 6532–6545 (2018).

214. Hestand, N. J. & Spano, F. C. Expanded Theory of H- and J-Molecular Aggregates: The Effects of Vibronic Coupling and Intermolecular Charge Transfer. *Chem. Rev.* **118**, 7069–7163 (2018).

215. Rahimi, K. *et al.* Light absorption of poly(3-hexylthiophene) single crystals. *RSC Adv.* **4**, 11121–11123 (2014).

216. Fuoss, R. M. & Kraus, C. A. Properties of Electrolytic Solutions. III. The Dissociation Constant. *J. Am. Chem. Soc.* **55**, 1019–1028 (1933).

217. Panday, A. *et al.* Effect of Molecular Weight and Salt Concentration on Conductivity of Block Copolymer Electrolytes. *Macromolecules* **42**, 4632–4637 (2009).

218. Nishimoto, A., Watanabe, M., Ikeda, Y. & Kohjiya, S. High ionic conductivity of new polymer electrolytes based on high molecular weight polyether comb polymers. *Electrochimica Acta* **43**, 1177–1184 (1998).

219. Flagg, L. Q. *et al.* Polymer Crystallinity Controls Water Uptake in Glycol Side-Chain Polymer Organic Electrochemical Transistors. *J. Am. Chem. Soc.* **141**, 4345–4354 (2019).

220. Olsher, Uriel., Izatt, R. M., Bradshaw, J. S. & Dalley, N. Kent. Coordination chemistry of lithium ion: a crystal and molecular structure review. *Chem. Rev.* **91**, 137–164 (1991).

Appendix B: List of Publications

1. Tatum, W. K., Torrejon, D., O'Neil, P., Onorato, J. W., Resing, A. B., Holliday, S., Flagg, L. Q., Ginger, D. S., Luscombe, C. K. Generalizable Framework for Algorithmic Interpretation of Thin Film Morphologies in Scanning Probe Images. *J. Chem. Inf. Model.* (2020) doi:10.1021/acs.jcim.0c00308.

2. Herbert, K., M., Getty, P. T., Dolinski, N. D., Hertzog, J. E., de Jong, D., Lettow, J. H., Romulus, J., Onorato, J. W., Foster, E. M., Rowan, S. J. Dynamic Reaction-Induced Phase Separation in Tunable, Adaptive Covalent Networks. *Chem. Sci.* **11**, 5028–5036 (2020).
3. Bischak, C. G., Flagg, L. Q., Yan, K., Rehman, T., Davies, D. W., Quezada, R. J., Onorato, J. W., Luscombe, C. K., Diao, Y., Li, C.-Z., Ginger, D. S. A Reversible Structural Phase Transition by Electrochemically-Driven Ion Injection into a Conjugated Polymer. *J. Am. Chem. Soc.* **142**, 7434–7442 (2020).

4. Flagg, L. Q., Bischak, C. G., Quezada, R. J., Onorato, J. W., Luscombe, C. K., Ginger, D. S. P-Type Electrochemical Doping Can Occur by Cation Expulsion in a High-Performing Polymer for Organic Electrochemical Transistors. *ACS Mater. Lett.* **2**, 254–260 (2020).
5. Gu, K., Onorato, J. W., Luscombe, C. K. & Loo, Y.-L. The Role of Tie Chains on the Mechano-Electrical Properties of Semiconducting Polymer Films. *Adv. Electron. Mater.* **6**, 1901070 (2020).
6. Pakhnyuk, V., Onorato, J. W., Steiner, E. J., Cohen, T. A. & Luscombe, C. K. Enhanced Miscibility and Strain Resistance of Blended Elastomer/π-conjugated Polymer

Composites Through Side Chain Functionalization Towards Stretchable Electronics. *Polym. Int.* **69**, 308–316 (2020).

7. Flagg, L. Q., Bischak, C. G., Onorato, J. W., Rashid, R. B., Luscombe, C. K., Ginger, D. S. Polymer Crystallinity Controls Water Uptake in Glycol Side-Chain Polymer Organic Electrochemical Transistors. *J. Am. Chem. Soc.* **141**, 4345–4354 (2019).
8. Dong, B. X., Nowak, C., Onorato, J. W., Strzalka, J., Escobedo, F. A., Luscombe, C. K., Nealey, P. F., Patel, S. N. Influence of Side-Chain Chemistry on Structure and Ionic Conduction Characteristics of Polythiophene Derivatives: A Computational and Experimental Study. *Chem. Mater.* **31**, 1418–1429 (2019).
9. Onorato, J. W. & Luscombe, C. K. Morphological Effects on Polymeric Mixed Ionic/Electronic Conductors. *Mol. Syst. Des. Eng.* **4**, 310–324 (2019).
10. Gu, K., Snyder, C. R., Onorato, J., Luscombe, C. K., Bosse, A. W., Loo, Y.-L. Assessing the Huang–Brown Description of Tie Chains for Charge Transport in Conjugated Polymers. *ACS Macro Lett.* **7**, 1333–1338 (2018).
11. Chew, A. R., Ghosh, R., Pakhnyuk, V., Onorato, J., Davidson, E. C., Segalman, R. A., Luscombe, C. K., Spano, F. C., Salleo, A. Unraveling the Effect of Conformational and Electronic Disorder in the Charge Transport Processes of Semiconducting Polymers. *Adv. Funct. Mater.* **28**, 1804142 (2018).
12. Li, Y., Tatum, W. K., Onorato, J. W., Zhang, Y. & Luscombe, C. K. Low Elastic Modulus and High Charge Mobility of Low-Crystallinity Indacenodithiophene-Based Semiconducting Polymers for Potential Applications in Stretchable Electronics. *Macromolecules* **51**, 6352–6358 (2018).

13. Ghosh, R., Chew, A. R., Onorato, J., Pakhnyuk, V., Luscombe, C. K., Salleo, A., Spano, F. C. Spectral Signatures and Spatial Coherence of Bound and Unbound Polarons in P3HT Films: Theory Versus Experiment. *J. Phys. Chem. C* **122**, 18048–18060 (2018).
14. Gu, K., Onorato, J., Xiao, S. S., Luscombe, C. K. & Loo, Y.-L. Determination of the Molecular Weight of Conjugated Polymers with Diffusion-Ordered NMR Spectroscopy. *Chem. Mater.* **30**, 570–576 (2018).
15. Scholes, D. T., Yee, P. Y., Lindemuth, J. R., Kang, H., Onorato, J., Ghosh, R., Luscombe, C. K., Spano, F. C., Tolbert, S. H., Schwartz, B. J. The Effects of Crystallinity on Charge Transport and the Structure of Sequentially Processed F4TCNQ-Doped Conjugated Polymer Films. *Adv. Funct. Mater.* **27**, 1702654 (2017).
16. Giridharagopal, R., Flagg, L. Q., Harrison, J. S., Ziffer, M. E., Onorato, J., Luscombe, C. K., Ginger, D. S. Electrochemical Strain Microscopy Probes Morphology-Induced Variations in Ion Uptake and Performance in Organic Electrochemical Transistors. *Nat. Mater.* **16**, 737–742 (2017).
17. Li, Y., Tatum, W. K., Onorato, J. W., Barajas, S. D., Yang, Y. Y., Luscombe, C. K. An Indacenodithiophene-Based Semiconducting Polymer with High Ductility for Stretchable Organic Electronics. *Polym. Chem.* **8**, 5185–5193 (2017).
18. Onorato, J., Pakhnyuk, V. & Luscombe, C. K. Structure and Design of Polymers for Durable, Stretchable Organic Electronics. *Polym. J.* **49**, 41–60 (2017).

Appendix C: Vita

Jonathan Onorato was born in south Florida, along the Gulf Coast, but went to high school in northern Pennsylvania. It was there that he was first exposed to the joys of chemistry when he took Mr. Phil Sarver’s AP Chemistry course. Mr. Sarver’s class, but more specifically Mr. Sarver’s enthusiasm was a significant inspiration for Jonathan and resulted in him looking for a chemistry-involved degree in college. At Case Western Reserve University, Jonathan took Introduction to Materials Science from Prof. David Schiraldi and found his career. He eventually received his BSE in Polymer Science and Engineering from Case Western Reserve University in Cleveland, Ohio, where he worked for Prof. Stuart Rowan for his senior thesis research, where he studied dynamic covalent chemistry and the potential for introducing self-healing chemistry into materials. Following his graduation in Spring 2015, he went on to join the lab of Prof. Christine Luscombe at the University of Washington for his PhD research in the Materials Science and Engineering department where he received the Wagstaff, DIRECT, and CEI fellowships. At UW, his research work focused on a wide-range of topics, including structure-property relationship and mechanical properties of conjugated polymers, mixed ionic/electronic conducting polymers, and data science and machine learning methods applied to chemistry.